

Cosmic Star Formation History

PIERO MADAU,
*Department of Astronomy and Astrophysics, University of California,
 1156 High Street, Santa Cruz, CA 95064; pmadau@ucolick.org*

MARK DICKINSON
*National Optical Astronomy Observatory, 950 North Cherry Avenue,
 Tucson, AZ 85719; med@noao.edu*

Key Words

cosmology, galaxies: galaxy formation, evolution, star formation, stellar populations

Abstract

Over the last decade and a half, an avalanche of new data from multiwavelength imaging and spectroscopic surveys has revolutionized our view of galaxy formation and evolution. Making sense of it all and fitting it together into a coherent picture remains one of astronomy’s great challenges. Here we review the range of complementary techniques and theoretical tools that are allowing astronomers to map the cosmic history of star formation, heavy element production, and reionization of the universe from the cosmic “dark ages” to the present epoch. A consistent picture is emerging from modern galaxy surveys, whereby the star formation rate density peaked about 3.5 Gyr after the Big Bang, at $z \approx 1.9$, and declined exponentially at later times, with an e-folding timescale of 3.9 Gyr. Half of the stellar mass observed today was formed before a redshift $z = 1.3$. About 25% formed before the peak of the cosmic star formation rate density, and another 25% formed after $z = 0.7$. Less than $\sim 1\%$ of today’s stars formed during the epoch of reionization, at $z > 6$. Under the simple assumption of a universal initial mass function, the global stellar mass density inferred at any epoch matches reasonably well the time integral of all the preceding star formation activity, although a mild disagreement may still point to unresolved issues with the measurements, or to deviations in the stellar initial mass function from conventional assumptions. The assembly histories of the stellar component of galaxies and their central black holes were quite similar, offering evidence for the co-evolution of black holes and their host galaxies. The rise of the mean metallicity of the universe to about 0.001 solar by redshift six, one Gyr after the Big Bang, appears to have been accompanied by the production of fewer than ten hydrogen Lyman-continuum photons per baryon, a rather tight budget for cosmological reionization.

CONTENTS

INTRODUCTION	2
------------------------	---

THE EQUATIONS OF COSMIC CHEMICAL EVOLUTION 5

MEASURING MASS FROM LIGHT 7
Star Formation Rates 11
“Weighing” Stellar Mass 23

TRACING THE GALAXY EMISSION HISTORY WITH LARGE SURVEYS 25
UV surveys 26
Infrared surveys 30
Emission line surveys 35
Radio surveys 38
Stellar mass density surveys 39
The state of the art, and what’s wrong with it 42

FROM OBSERVATIONS TO GENERAL PRINCIPLES 45
Star Formation Density 46
Core-Collapse Supernova Rate 50
Stellar Mass Density 51
Fossil Cosmology 54
The Global Specific Star Formation Rate 56
Cosmic Metallicity 57
Black Hole Accretion History 60
First Light and Cosmic Reionization 61

CONCLUDING REMARKS 63

DISCLOSURE STATEMENT 66

ACKNOWLEDGMENTS 66

1 INTRODUCTION

The origin and evolution of galaxies is one of the most intriguing and complex chapters in the formation of cosmic structure, and observations in this field have accumulated at an astonishing pace during the last decade and a half. Multiwavelength imaging surveys with the *Hubble* and *Spitzer* Space Telescopes and ground-based facilities, together with spectroscopic follow-up with 8-m class telescopes, have led to the discovery of galaxies with confirmed redshifts as large as $z = 7.5$ (Finkelstein et al. 2013), and compelling photometric candidates as far back as $z \approx 11$ (Coe et al. 2013), when the universe was only 3% of its current age. Following the seminal work of Steidel et al. (1995), color-selection criteria that are sensitive to the presence of intergalactic H I absorption features in the spectral energy distribution (SED) of distant sources have been used to build increasingly large samples of star-forming galaxies at $2.5 \lesssim z \lesssim 9$ (e.g., Madau et al. 1996; Steidel et al. 2003; Giavalisco et al. 2004a; Bouwens et al. 2011b). Infrared/optical color selection criteria have been shown to efficiently isolate both actively star-forming and passively evolving galaxies at $z \approx 2$ (Franx et al. 2003; Daddi et al. 2004). Photometric redshifts have become an unavoidable tool for placing faint galaxies onto a cosmic timeline. *Spitzer*, *Herschel*, and submillimeter telescopes have revealed that dusty galaxies with star formation rates (SFRs) of order $100 M_{\odot} \text{ yr}^{-1}$ or more were abundant when the universe was only 2–3 Gyr old (Barger et al. 1998; Daddi et al. 2005; Gruppioni et al. 2013). Deep near-infrared observations are now commonly used to select galaxies based on their optical rest-frame light, and to chart the evolution of the global stellar mass density at $0 < z < 3$ (Dickinson et al. 2003). The *Galaxy Evolution Explorer (GALEX)* satellite has quantified the ultraviolet galaxy luminosity function of galaxies in the local universe, and its evolution at $z \lesssim 1$.

Ground-based observations, and, subsequently, UV and IR data from *GALEX* and *Spitzer*, have confirmed that star formation activity was significantly higher in the past (Lilly et al. 1996; Schiminovich et al. 2005; Le Floch et al. 2005). In the local universe, various galaxy properties (colors, surface mass densities, and concentrations) have been observed by the *Sloan Digital Sky Survey* (SDSS) to be “bimodal” around a transitional stellar mass of $3 \times 10^{10} M_{\odot}$ (Kauffmann et al. 2003), showing a clear division between faint, blue, active galaxies and bright, red, passive systems. The number and total stellar mass of blue galaxies appear to have remained nearly constant since $z \sim 1$, whereas those of red galaxies (around L^*) have been rising (Faber et al. 2007). At redshifts $0 < z < 2$ at least, and perhaps earlier, most star-forming galaxies are observed to obey a relatively tight “main sequence” correlation between their star formation rates and stellar masses (Brinchmann et al. 2004; Noeske et al. 2007; Elbaz et al. 2007; Daddi et al. 2007). A minority of starburst galaxies have elevated star formation rates, above this main sequence, as well as a growing population of quiescent galaxies that fall below it.

With the avalanche of new data, galaxy taxonomy has been enriched by the addition of new acronyms like LBGs, LAEs, EROs, BzKs, DRGs, DOGs, LIRGs, ULIRGs, SMGs, etc. Making sense of it all and fitting it together into a coherent picture remains one of astronomy’s great challenges, in part because of the observational difficulty of tracking continuously transforming galaxy sub-populations across cosmic time, and in part because theory provides only a partial interpretative framework. The key idea of standard cosmological scenarios, that primordial density fluctuations grow by gravitational instability driven by cold, collisionless dark matter, leads to a “bottom-up” Λ CDM scenario of structure formation (Peebles 1982). Galaxies form hierarchically, with low-mass objects (“halos”) collapsing earlier and merging to form larger and larger systems over time – from ultra-faint dwarfs to clusters of galaxies (Blumenthal et al. 1984). Ordinary matter in the universe follows the dynamics dictated by the dark matter until radiative, hydrodynamic, and star formation processes take over (White & Rees 1978). But while the “dark side” of galaxy formation can be modeled with high accuracy and has been explored in details through N -body numerical simulations of increasing resolution and size (e.g., Davis et al. 1985; Dubinski & Carlberg 1991; Moore et al. 1999; Springel et al. 2005; Diemand et al. 2008; Springel et al. 2008; Stadel et al. 2009; Klypin et al. 2011), the same does not hold for the baryons. The complex processes of baryonic dissipation inside evolving CDM halos, the transformation of cold gas into stars, the formation of disks and spheroids, the chemical enrichment of gaseous material on galactic and intergalactic scales, and above all the role played by “feedback” (the effect of the energy input from stars, supernovae, and massive black holes on their environment) in regulating star formation and generating galactic outflows, are still poorly understood. The purely phenomenological treatment of complex physical processes that is at the core of semi-analytic schemes of galaxy formation (e.g., White & Frenk 1991; Kauffmann et al. 1993; Somerville & Primack 1999; Cole et al. 2000), and – at a much higher level of realism – the “subgrid modeling” of star formation and stellar feedback that must be implemented even in the more accurate cosmological hydrodynamic simulations (e.g., Katz et al. 1996; Yepes et al. 1997; Navarro & Steinmetz 2000; Springel & Hernquist 2003; Keres et al. 2005; Ocvirk et al. 2008; Governato et al. 2010; Guedes et al. 2011; Hopkins et al. 2012; Kuhlen et al. 2012; Zemp et al. 2012; Agertz et al. 2013) are sensitive to poorly determined parameters and suffer from various degeneracies, a weakness that has traditionally prevented robust predictions to be made in advance of specific observations.

Ideally, an in-depth understanding of galaxy evolution would encompass the full sequence of events that led from the formation of the first stars after the end of the cosmic dark ages

to the present-day diversity of forms, sizes, masses, colors, luminosities, metallicities, and clustering properties of galaxies. This is a daunting task, and it is perhaps not surprising that an alternative way to look at and interpret the bewildering variety of galaxy data has become very popular in the last decade and a half. The method focuses on the emission properties of the galaxy population as a whole, traces the evolution with cosmic time of the galaxy luminosity density from the far-UV (FUV) to the far-IR (FIR), and offers the prospect of an empirical determination of the global history of star formation and heavy element production of the universe, independently of the complex evolutionary phases of individual galaxy subpopulations. The modern version of this technique relies on some basic properties of stellar populations and dusty starburst galaxies: 1) the UV-continuum emission in all but the oldest galaxies is dominated by short-lived massive stars, and is therefore a direct measure, for a given stellar initial mass function (IMF) and dust content, of the instantaneous star formation rate density (SFRD); 2) the rest-frame near-infrared (NIR) light is dominated by near-solar mass evolved stars that make up the bulk of a galaxy’s stellar mass, and can then be used as a tracer of the total stellar mass density (SMD); and 3) interstellar dust absorbs preferentially UV light and re-radiates it in the thermal IR, so that the far-IR emission of dusty starburst galaxies can be a sensitive tracer of young stellar populations and the SFRD. By modeling the emission history of all stars in the universe at ultraviolet, optical, and infrared wavelengths from the present epoch to $z \approx 8$ and beyond, one can then shed light on some key questions in galaxy formation and evolution studies: Is there a characteristic cosmic epoch of star and heavy elements formation in galaxies? What fraction of the luminous baryons observed today were already locked into galaxies at early times? Are the data consistent with a universal IMF? Do galaxies reionize the universe at a redshift greater than 6? Can we account for all the metals produced by the global star formation activity from the Big Bang to the present? How does the cosmic history of star formation compare with the history of mass accretion onto massive black holes as traced by luminous quasars?

This review focuses on the range of observations, methods, and theoretical tools that are allowing astronomers to map the rate of transformation of gas into stars in the universe, from the cosmic dark ages to the present epoch. Given the limited space available, it is impossible to provide a thorough survey of such a huge community effort without leaving out significant contributions or whole subfields. We have therefore tried to refer only briefly to earlier findings, and present recent observations in more detail, limiting the number of studies cited and highlighting key research areas. In doing so, we hope to provide a manageable overview of how the field has developed and matured in line with new technological advances and theoretical insights, and of the questions with which astronomers still struggle nowadays.

The remainder of this review is organized as follows. The equations of cosmic chemical evolution that govern the consumption of gas into stars and the formation and dispersal of heavy elements in the universe as a whole are given in §2. We turn to the topic of measuring mass from light, and draw attention to areas of uncertainty in §3. Large surveys, key datasets and the analyses thereof are highlighted in §4. An up-to-date determination of the star formation history of the universe is provided and its main implications are discussed in §5. Finally, we summarize our conclusions in §6. Unless otherwise stated, all results presented here will assume a “cosmic concordance cosmology” with parameters $(\Omega_M, \Omega_\Lambda, \Omega_b, h) = (0.3, 0.7, 0.045, 0.7)$.

2 THE EQUATIONS OF COSMIC CHEMICAL EVOLUTION

To pursue and cast into a quantitative form the idea of a cosmic star formation and metal enrichment history – not of any particular type of galaxies but of the universe as a whole – it is useful to start by generalizing the standard equations of galaxy evolution (Tinsley 1980) over all galaxies and intergalactic gas in the universe. In a representative cosmological comoving volume having density ρ_* in long-lived stars and stellar remnants (white dwarfs, neutron stars, black holes) and gas density ρ_g , and in which new stars are formed at the rate ψ , the equations of cosmic chemical evolution can be written as

$$\begin{aligned}\frac{d\rho_*}{dt} &= (1 - R)\psi \\ \frac{d\rho_g}{dt} &= -\frac{d\rho_*}{dt} \\ \rho_g \frac{dZ}{dt} &= y(1 - R)\psi.\end{aligned}\tag{1}$$

Here, Z is the metallicity in the gas and newly born stars, R is the “return fraction” or the mass fraction of each generation of stars that is put back into the interstellar (ISM) and intergalactic (IGM) medium, and y is the net metal yield or the mass of new heavy elements created and ejected into the ISM/IGM by each generation of stars per unit mass locked into stars. The above equations govern the formation, destruction, and distribution of heavy elements as they cycle through stars and are ultimately dispersed into the ISM/IGM. By treating all galaxies as a single stellar system and all baryons in the ISM/IGM as its gas reservoir, their solution enables the mean trends of galaxy populations to be calculated with the fewest number of free parameters. The equations state that, for every new mass element locked forever into long-lived stars and stellar remnants, $\Delta\rho_*$, the metallicity of the ISM/IGM increases as $\Delta Z = y\Delta\rho_*/\rho_g$ while the mass of heavy elements in the ISM/IGM changes as $\Delta(Z\rho_g) = (y - Z)\Delta\rho_*$. The latter expression is a consequence of metals being both released into the gas from mass loss during post-main sequence stellar evolution as well as being removed from the ISM/IGM when new stars condense out. Note how, compared to the source term, the metal sink term can be neglected at early epochs when $Z \ll y$.

Equations (1) can be integrated to give, at redshift z :

1. the total mass density of long-lived stars and stellar remnants accumulated from earlier episodes of star formation,

$$\rho_*(z) = (1 - R) \int_0^{t(z)} \psi dt = (1 - R) \int_z^\infty \psi \frac{dz'}{H(z')(1 + z')},\tag{2}$$

where $H(z') = H_0[\Omega_M(1 + z')^3 + \Omega_\Lambda]^{1/2}$ is the Hubble parameter in a flat cosmology;

2. the total mass density of gas,

$$\rho_g(z) = \rho_{g,\infty} - \rho_*(z),\tag{3}$$

where $\rho_{g,\infty}$ is the comoving density of gas at some suitable high redshift where there are no stars or heavy elements; and

3. the total mass density of heavy elements in the ISM/IGM,

$$\begin{aligned}Z(z)\rho_g(z) &= y(1 - R) \int_0^{t(z)} \psi dt - (1 - R) \int_0^{t(z)} Z\psi dt \\ &\equiv [y - \langle Z_*(z) \rangle] \rho_*(z)\end{aligned}\tag{4}$$

where the term $\langle Z_* \rangle \rho_*$ is the total metal content of stars and remnants at that redshift. Note that the instantaneous total metal ejection rate, E_Z , is the sum of a recycle term and a creation term (Maeder 1992),

$$E_Z = ZR\psi + y(1 - R)\psi, \quad (5)$$

where the first term is the amount of heavy elements initially lost from the ISM when stars formed that are now being re-released, and the second represents the new metals synthesized by stars and released during mass loss.

For a given universal stellar IMF, the quantities R and y can be derived using the following formulae:

$$R = \int_{m_0}^{m_u} (m - w_m)\phi(m)dm \quad (6)$$

$$y(1 - R) = \int_{m_0}^{m_u} my_m\phi(m)dm, \quad (7)$$

where m is mass of a star, w_m is its remnant mass, $\phi(m)$ is the initial mass function [normalized so that $\int_{m_l}^{m_u} m\phi(m)dm = 1$], and y_m is the stellar yield, i.e., the fraction of mass m that is converted to metals and ejected.¹ The above equations have been written under the simplifying assumptions of “instantaneous recycling” (where the release and mixing of the products of nucleosynthesis by all stars more massive than m_0 occur on a timescale that is much shorter than the Hubble time, while stars with $m < m_0$ live forever), “one zone” (where the heavy elements are well mixed at all times within the volume under consideration), “closed box” (flows of gas in and out the chosen volume are negligible), and “constant IMF and metal yield”.

Recall now that the main sequence timescale is shorter than 0.6 Gyr (the age of the universe at $z = 8.5$) for stars more massive than $2.5 M_\odot$, while stars less massive than $0.9 M_\odot$ never evolve off the main sequence.² So over the redshift range of interest here, the instantaneous recycling approximation may break down in the limited mass range $0.9 < m < 2.5 M_\odot$. For illustrative purposes, we shall adopt in the following the initial-final mass values for white dwarfs tabulated by Weidemann (2000), which can be fit to few percent accuracy over the interval $1 M_\odot < m < 7 M_\odot$ as $w_m = 0.444 + 0.084m$. We shall also assume that all stars with $8 M_\odot < m < m_{\text{BH}} = 40 M_\odot$ return all but a $w_m = 1.4 M_\odot$ remnant, and stars above m_{BH} collapse to black holes without ejecting material into space, i.e., $w_m = m$. Few stars form with masses above $40 M_\odot$, so the impact of the latter simplifying assumption on chemical evolution is minimal. Taking then $m_0 = 1 M_\odot$ as the dividing stellar mass for instantaneous recycling and a Salpeter (1955) IMF with $\phi(m) \propto m^{-2.35}$ in the range $m_l = 0.1 M_\odot < m < m_u = 100 M_\odot$, one derives a return fraction of $R = 0.27$. Under the same assumptions, a Chabrier (2003) IMF,

$$\phi(m) \propto \begin{cases} e^{-(\log m - \log m_c)^2 / 2\sigma^2} / m & (m < 1 M_\odot) \\ m^{-2.3} & (m > 1 M_\odot) \end{cases} \quad (8)$$

¹In this review, the term “yield” will generally indicate the net yield y of a stellar population as defined in eq. (7); we will explicitly speak, instead, of “stellar yields” to indicate the y_m resulting from nucleosynthesis calculations.

²Stellar evolutionary models by Schaller et al. (1992) show that for $m < 7 M_\odot$, solar-metallicity stars have longer lifetimes than their metal-poor counterparts, while the opposite is true for $m > 9 M_\odot$.

(with $m_c = 0.08 M_\odot$ and $\sigma = 0.69$) is more weighted towards short-lived massive stars and yields a larger return fraction, $R = 0.41$. In the instantaneous recycling approximation, the fraction of “dark” stellar remnants formed in each generation is

$$D = \int_{m_0}^{m_u} w_m \phi(m) dm. \quad (9)$$

The two IMFs produce a dark remnant mass fraction of $D = 0.12$ and $D = 0.19$, respectively. The stellar nucleosynthetic yields depend on metallicity, rotation, and the mass limit for black hole formation m_{BH} . By integrating over the IMF the subsolar metallicity stellar yields (where the effect of mass loss is negligible) tabulated by Maeder (1992) from $10 M_\odot$ to $m_{\text{BH}} = 40, M_\odot$, we obtain $y = 0.016$ for Salpeter and $y = 0.032$ for a Chabrier IMF. The same tabulation, when integrated to $m_{\text{BH}} = 60 M_\odot$ instead, implies $y = 0.023$ (with $R = 0.29$) and $y = 0.048$ (with $R = 0.44$) for a Salpeter and Chabrier IMF, respectively. Notice that some of the uncertainties associated with the IMF and the mass cutoff m_{BH} become smaller when computing the term $y(1 - R)$ in the equations (1). For massive stars at solar metallicities, stellar winds eject large amount of helium and carbon into the ISM before these are processed into heavier elements, but the effect on the integrated metal yields ($10 - 40 M_\odot$) is weak (Maeder 1992). Total stellar yields (including the wind and pre-supernova contributions) obtained from rotating stellar models at solar metallicity have been presented by Hirschi et al. (2005). Over the same range $10 - 40 M_\odot$, we derive in this case $y = 0.019$ for Salpeter and $y = 0.038$ for Chabrier. For comparison, the zero-metallicity stellar yields of Chieffi & Limongi (2004) imply $y = 0.015$ for Salpeter and $y = 0.030$ for Chabrier.

Although disfavored by many observations, a Salpeter IMF in the mass range $0.1 - 100 M_\odot$ will be used as a reference throughout the rest of this review. Similarly, for consistency with prior work, we will assume the canonical metallicity scale where solar metallicity is $Z_\odot = 0.02$, rather than the revised value $Z_\odot = 0.014$ of Asplund et al. (2009).

3 MEASURING MASS FROM LIGHT

At its heart, deriving the history of galaxies’ star formation involves inferring mass from light. We observe the emission from galaxies at various wavelengths, and from those measurements we try to infer the rates at which the galaxies are forming stars, or their integrated stellar masses. Figure 1 illustrates the sensitivity of today’s premier multiwavelength surveys to the star formation rates and stellar masses of galaxies at high redshift. Rest-frame ultraviolet, infrared, submillimeter and radio emission, as well as nebular lines such as $\text{H}\alpha$, are all used to measure star formation rates and will be discussed in this section. In the absence of extinction, UV measurements are more sensitive than current IR or radio data by orders of magnitude, but in practice dust attenuation is often severe. Long-wavelength data are essential to gain a comprehensive picture of cosmic star formation, but are limited by current instrumental sensitivities, although ALMA enables dramatic improvements at submillimeter wavelengths that are particularly valuable at higher redshifts. Near- to mid-infrared measurements are critical for deriving stellar masses. Their sensitivity to stellar mass depends critically on the mass-to-light ratio of the stellar population in a distant galaxy, hence on its age, star formation history, and extinction. Figure 1 (*bottom*) illustrates two limiting cases: a maximum- M/L model defined as a passively evolving stellar population as old as the universe, and a minimum- M/L model defined as a very young, unreddened, actively star-forming galaxy. In principle, surveys should be mass-complete to

the maximum- M/L limits. Much less massive galaxies with young, low- M/L stellar populations can easily be detected, but observations would miss dusty or evolved galaxies with lower masses. The *HST* WFC3 camera has significantly improved near-infrared sensitivity compared to most ground-based imaging, but only samples optical rest frame light at $z < 3$. *Spitzer's* IRAC remains the premier resource for deriving stellar masses at higher redshifts, and *JWST* will provide a major advance.

The conversions from light to mass are derived or calibrated using stellar population synthesis models, which encode our knowledge of stellar evolution and of the spectral energy distributions of stars, and compute the emergent spectrum for a galaxy with given properties. This knowledge is imperfect, although astronomers have made great progress developing population synthesis models and improving the libraries of empirical and theoretical stellar spectra that they use (for a recent review see Conroy 2013).

A galaxy (or of the universe as a whole, for that matter) consists of stars that span a wide range of masses, ages, and metal abundances. The light from those stars may be attenuated by dust before it emerges from the galaxy; the dust dims and generally reddens the galaxy spectrum, and the heated dust re-emits energy in the infrared. A galaxy spectrum arises from a composite stellar population whose true distribution of properties is generally unknown. For nearby galaxies, resolved color-magnitude diagrams can reveal the actual distributions of stellar properties, but for most galaxies we can observe only their integrated light, and properties of the emergent spectrum (particularly broad band colors) are often degenerate to different intrinsic properties. An often-noted example is the degeneracy between age, metallicity, and dust attenuation, all of which can redden the spectrum of a galaxy. Observations at higher spectral resolution, for example of individual spectral lines, can help to resolve some degeneracies (e.g., to constrain stellar metallicities or population ages from absorption line strengths, or reddening from emission line ratios), but never all: the inherently composite nature of stellar populations requires that we make simplifying assumptions when interpreting the light, assumptions that generally cannot be uniquely tested for individual galaxies. Examples of such assumptions include the form of the IMF, the stellar metallicity distribution, the wavelength dependence of dust attenuation, or the precise star formation history (SFH) of the galaxy. The hope is that these assumptions can be made as reasonably as possible, that their impact on derived masses or star formation rates can be estimated, and that ultimately they may be tested or constrained by observations in various ways.

Initial Mass Function The IMF underlies the relation between mass, light, and stellar population age. It controls the ratio of hot, bright stars that dominate the light, to the cool, faint stars that usually dominate the mass. It regulates the luminosity and color evolution of the integrated stellar population, as stars with different masses evolve at different rates. It also affects the time evolution of the integrated stellar mass, which changes as more massive stars lose gas to the ISM via winds, or detonate as supernovae.

It is essentially impossible to constrain the IMF from photometric measurements of the integrated light from galaxies: the color of a galaxy does not uniquely reveal its underlying IMF, as there are too many degeneracies to permit useful constraints. Even detailed spectroscopy does not usually offer strong constraints on the IMF overall, although certain spectral features can be useful diagnostics of the number of stars in a given mass range (e.g., Leitherer et al. 1999). The most direct constraints on the IMF come from counting stars as a function of mass in resolved, nearby stellar populations, but they must be very nearby indeed (within our Galaxy and its satellites) in order to detect sub-solar dwarf stars which

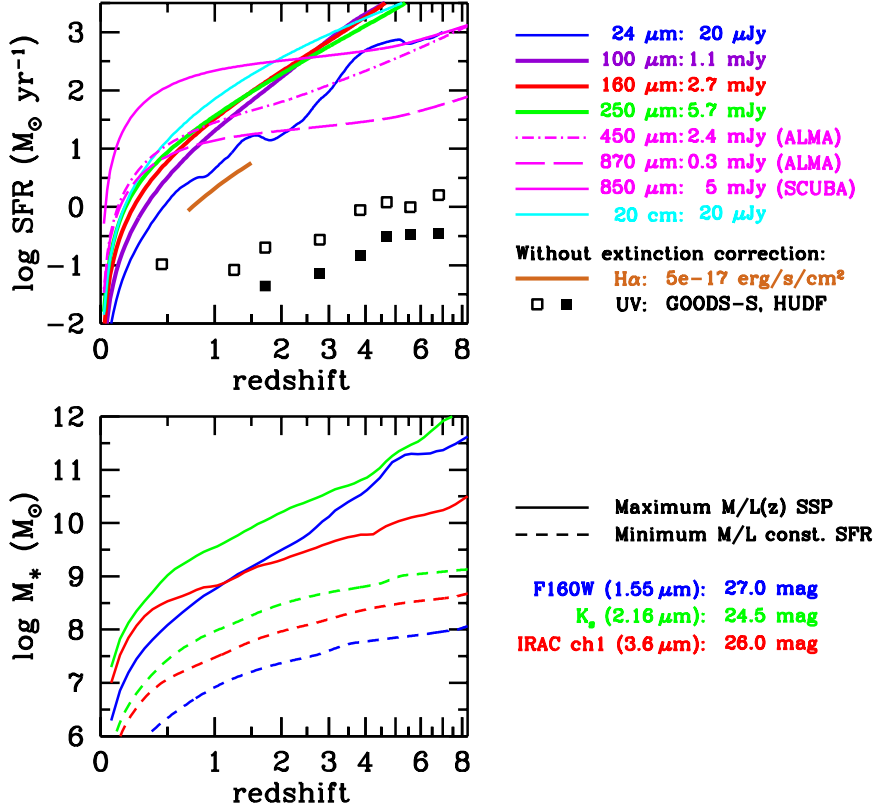


Figure 1: *Top panel:* Sensitivity to star formation versus redshift for deep survey data at various wavelengths. The key at right indicates the wavelengths and the corresponding flux limits. Most of these limits were computed based on data available in the GOODS fields, or are simply chosen to be representative values for very deep surveys. For ALMA we use projected sensitivities of the completed interferometer for modest 10 minute integration times, noting that the small ALMA primary beam at 870 μm and 450 μm requires about 50 and 170 pointings (respectively) to map 1 square arcminute with uniform sensitivity. All conversions to SFR assume a Salpeter IMF from 0.1 to 100 M_{\odot} . The limits for mid-IR (*Spitzer*), far-IR (*Herschel*), submillimeter and radio data use bolometric corrections from the observed wavelength based on spectral energy distribution templates from Elbaz et al. (2011). Open square points show rest-frame 1500 \AA sensitivities assuming *no extinction*; in practice, dust attenuation can significantly increase these limits. The open squares are based on GOODS data from *GALEX*, ground-based *U*-band (Nonino et al. 2009), and *HST* ACS and WFC3 (CANDELS), while the filled points show *HST* ACS and WFC3 limits for the HUDF (Bouwens et al. 2011b). The $\text{H}\alpha$ curve shown here represents the typical limiting sensitivity of the 3D-HST infrared grism spectroscopic survey (Brammer et al. 2012), again assuming *no extinction*, with conversion to SFR from Kennicutt (1998). *Bottom panel:* Sensitivity to stellar mass versus redshift, for flux limits at several wavelengths, as indicated at right. The solid curves assume a passively evolving simple stellar population with the age of the universe, solar metallicity, a Salpeter IMF, and no extinction, computed using the models of Conroy et al. (2009). This approximates the maximum mass-to-light ratio one might see at any redshift, and hence an upper bound to the mass completeness limit for a given survey. Less massive galaxies can easily be detected, however, if they have young stellar populations. The dashed curves show sensitivities for an unreddened galaxy with a constant SFR and age of 10^7 years, when M/L at these wavelengths reaches a minimum value. The infrared sensitivity limits (given in AB magnitudes) are chosen to be representative of deep surveys like GOODS and CANDELS (e.g., K_s data from Retzlaff et al. 2010 or Wang et al. 2010), but are not specific to a particular data set.

dominate the mass of a stellar system. The next best constraints come from integrated measurements of the mass-to-light ratio for star clusters or galaxies, using kinematics (velocity dispersions or rotation curves) to derive a mass for comparison to the luminosity. However, these measurements are difficult to make for faint galaxies at high redshift, and require careful modeling to account for the role of dark matter and many other effects.

For lack of better information, astronomers often assume that the IMF is universal, with the same shape at all times and in all galaxies. While the IMF of various stellar populations within the Milky Way appears indeed to be invariant (for a review, see Bastian et al. 2010), recent studies suggest that the low-mass IMF slope may be a function of the global galactic potential, becoming increasingly shallow (bottom-light) with decreasing galaxy velocity dispersion (Conroy & van Dokkum 2012; Geha et al. 2013). It is still unknown, however, how galaxy to galaxy variations may affect the “cosmic” volume-averaged IMF as a function of redshift. In § 5 below we will see how a universal IMF can provide a reasonably consistent picture of the global star formation history. The exact shape of the IMF at low stellar masses is fairly unimportant for deriving *relative* stellar masses or star formation rates for galaxies. Low-mass stars contribute most of the mass but almost none of the light, and do not evolve over a Hubble time. Therefore changing the low-mass IMF mainly rescales the mass-to-light ratio M/L , and hence affects both stellar masses and SFRs derived from photometry to a similar degree. Changes to the intermediate- and high-mass region of the IMF, however, can have significant effects on the luminosity and color evolution, and hence on the galaxy properties derived from photometry. It is quite common to adopt the simple power-law IMF of Salpeter (1955), truncated over a finite mass range (generally, 0.1 to 100 M_{\odot} , as adopted in this review). However, most observations show that the actual IMF turns over from the Salpeter slope at masses $< 1 M_{\odot}$, resulting in smaller M/L ratios than those predicted by the Salpeter IMF. Some common versions of such an IMF are the broken power law representation used by Kroupa (2001), and the log-normal turnover suggested by Chabrier (2003).

Dust Extinction The shape of the extinction law depends on the properties of the dust grains causing the extinction. For observations of a single star, photons may be absorbed by dust or scattered out of the observed sightline. However, galaxies are 3-dimensional structures with mixed and varying distributions of stars and dust. Photons may be scattered both in and out of the sightline, and the optical depth of dust along the line of sight to the observer will be different for every star in the galaxy. These effects are generally lumped together into the simplifying assumption of a net dust attenuation curve, and such relations have been derived for local galaxy samples both empirically (e.g., Calzetti et al. 2000) and based on theoretical modeling (Charlot & Fall 2000). However, all galaxies are not equal, and no net attenuation law can really be used for all galaxies. There can always be stars that are completely obscured behind optically thick dust such that little or none of their light emerges directly from the galaxy, except re-radiated as dust emission. While for many galaxies this may not be a significant factor, there are certainly some starburst galaxies in which huge and bolometrically dominant star formation activity takes place in regions screened by hundreds of magnitudes of dust extinction. UV/optical measurements will never detect this light, but fortunately the star formation can be detected and measured at other wavelengths, e.g., with far-infrared or radio data.

Star Formation History The star formation histories of individual galaxies are unlikely to be smooth and simple; they may vary on both long and short time scales. The fact that

young stars are more luminous than older stars leads to the problem of “outshining” (e.g., Papovich et al. 2001; Maraston et al. 2010) – the light from older stars can be lost in the glare of more recent star formation, and contribute relatively little to the observed photometry from a galaxy, even if those stars contribute significantly to its mass. SED model fits to galaxies with recent star formation tend to be driven largely by the younger, brighter starlight, and may not constrain the mass (or other properties) of older stars that may be present.

We note that for the universe as a whole there is one “cosmic” IMF that represents the global average at a given time or redshift, whether or not the IMF varies from one galaxy to another. Similarly, there is a “cosmic” distribution of metallicities, a “cosmic” net attenuation of starlight by dust at a given wavelength, and the universe as a whole obeys one “cosmic” star formation history, which, moreover, was probably relatively smooth over time – i.e., any stochasticity or “burstiness” averages out when considered for the universe as a whole. In principle, these facts can simplify the determination of the cosmic star formation history, particularly when it is derived from measurements of integrated light averaging over all galaxies. In practice, however, astronomers often derive star formation rates and stellar masses for individual galaxies in their deep surveys, and then sum them to derive comoving volume averages. In that case, some of the advantages of the “cosmic averaging” are reduced.

3.1 Star Formation Rates

There are many ways in which to infer star formation rates from observations of the integrated light from galaxies. Kennicutt (1998) and Kennicutt & Evans (2012) have presented extensive review of this topic, and here we will only recap points that are particularly relevant for measurements of the global star formation history, particularly at high redshift. Virtually all observational tracers of star formation fundamentally measure the rate of *massive* star formation, since the massive stars emit most of the energy from a young stellar population. However, different observational tracers are sensitive to different ranges of stellar masses, and hence respond differently as a function of stellar population age. For example, H α emission arises primarily from HII regions photoionized by O stars with lifetimes shorter than 20 Myr, while UV continuum is produced by stars with spanning a broader mass range and with longer lifetimes. The time-dependence of different indicators can complicate efforts to derive accurate SFRs for individual galaxies, especially if their SFRs might be rapidly changing (e.g., during a starburst event), but they should average out when summing over a whole population of galaxies.

3.1.1 ULTRAVIOLET LIGHT Newly-formed stellar populations emit radiation over a broad spectrum. For a normal IMF, low-mass stars dominate the mass integrated over the whole stellar population, but at young ages the luminosity is dominated by ultraviolet emission from massive stars. These stars have short lifetimes, so the UV emission fades quickly. For a Salpeter IMF, the 1500 Å luminosity from an evolving simple stellar population (SSP, i.e., an ensemble of stars formed instantaneously and evolving together) with solar metallicity fades by a factor of 100 after 10^8 years, and by factors of 10^3 to 10^6 after 10^9 years, depending on metallicity (Figure 2). Bolometrically, at least half of the luminous energy that an SSP would produce over a 10 Gyr cosmic lifetime emerges in the first 100 Myr, mostly in the UV, making this a natural wavelength from which to infer star formation rates.

For a galaxy forming stars at a constant rate, the 1500 Å luminosity stabilizes once O-stars start to evolve off the main sequence. For solar metallicity, by an age of $10^{7.5}$ years, it has reached 75% of its asymptotic value, although convergence is somewhat slower at lower metallicity (Figure 2). For these reasons, the UV luminosity at wavelengths³ around 1500 Å is regarded as a good tracer of the formation rate of massive stars, provided that the time scale for significant fluctuations in the SFR is longer than a few $\times 10^7$ years. For shorter bursts or dips in the SFR, changes in the UV continuum flux may lag those in the SFR and smooth over such variations.

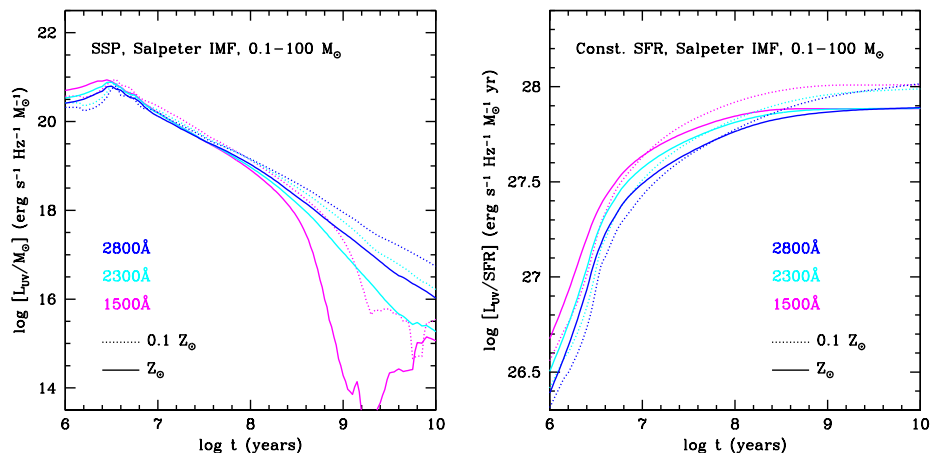


Figure 2: *Left panel:* Time dependence of the UV luminosity of a simple stellar population (SSP) with initial mass $1 M_{\odot}$, formed with a Salpeter IMF in the range $0.1 - 100 M_{\odot}$, measured at three wavelengths, 1500 Å, 2300 Å, and 2800 Å, and computed with the stellar population synthesis models of Conroy et al. (2009). *Solid lines:* Solar metallicity ($Z = 0.02$). *Dashed lines:* 1/10th solar metallicity ($Z = 0.002$). *Right panel:* Time dependence of the UV luminosity per unit star formation rate for a model with a constant star formation rate, shown for the same UV wavelengths and metallicities as in the figure at left.

Although the 1500 Å rest frame is readily accessible with ground-based optical observations of galaxies at redshifts $z \gtrsim 1.4$, measurements at lower redshifts require space-based UV data (e.g., from *GALEX* or *HST*), or are limited to longer UV wavelengths. 2300 Å (the approximate central wavelength of the *GALEX* NUV passband) and 2800 Å (used, e.g., by Lilly et al. 1996) are mid-UV reference wavelengths that have sometimes been used in the literature. The mid-UV emission from a galaxy can have a larger contribution from longer-lived, lower-mass stars, particularly at later ages, and the time evolution of the luminosity is more gradual. This is particularly true after ~ 250 Myr, when the 1500 Å luminosity of an SSP drops off sharply, while the 2800 Å luminosity continues to fade at an approximately exponential rate (Figure 2). For a constant star formation rate, the UV spectral slope reddens moderately with time, as the 1500 Å luminosity reaches a steady-state level earlier, while longer-lived (B and A) stars continue to build up and contribute to the 2800 Å luminosity. This complicates both the conversion from luminosity to SFR, as well as any correction for dust extinction based on the UV spectral slope. Still, for young ages, both shorter and longer UV wavelengths usefully trace the star formation rate, and have been

³Wavelengths from 1400–1700 Å have been used in the literature for both local and high redshift studies.

used extensively in the literature. Moreover, longer UV wavelengths are subject to somewhat lesser dust attenuation. Wavelengths shorter than that of Ly α (1216 Å) are rarely used to estimate star formation rates, particularly at high redshift where absorption from neutral hydrogen in the intergalactic medium is strong.

The UV luminosity output by a stellar population also depends on its metallicity, which affects stellar temperatures and line blanketing. Generally speaking, less metal rich stars produce more UV light. The amplitude of this effect is not insignificant, and depends on the details of the star formation history. From a Salpeter IMF and constant star formation rate, the range of FUV luminosity per unit SFR for stars spanning a factor of 100 in metallicity (from $Z = 0.0003$ to 0.03) is less than 0.24 dex, or 70%. These variations are larger at higher metallicities and older ages, and we might therefore expect significant evolution in the L_{FUV} to SFR conversion factor as the global metallicity of galaxies evolves.

We express the conversion factor between the intrinsic FUV specific luminosity $L_{\nu}(\text{FUV})$ (before extinction, or corrected for extinction) and the ongoing SFR as:

$$\text{SFR} = \mathcal{K}_{\text{FUV}} \times L_{\nu}(\text{FUV}), \quad (10)$$

where $L_{\nu}(\text{FUV})$ is expressed in units of $\text{erg s}^{-1} \text{Hz}^{-1}$ and SFR in units of $M_{\odot} \text{yr}^{-1}$. The precise value of the conversion factor \mathcal{K}_{FUV} is sensitive to the recent star formation and metal enrichment history, as well as the choice of the IMF. It is relatively insensitive to the exact FUV wavelength, as the UV spectrum of a galaxy with a constant star formation rate is quite flat in f_{ν} units, at least for ages much longer than 10^7 years. Generally, we will use FUV to refer to 1500 Å emission in this review, or be explicit when we refer to other UV wavelengths. For a Salpeter IMF in the mass range $0.1 - 100 M_{\odot}$ and constant SFR, the *Flexible Stellar Population Synthesis* (FSPS) models of Conroy et al. (2009) yield $\mathcal{K}_{\text{FUV}} = (1.55, 1.3, 1.1, 1.0) \times 10^{-28}$ for $\log Z_*/Z_{\odot} = (+0.2, 0, -0.5, -1.0)$ at age $\gtrsim 300$ Myr. The GALAXEV models of Bruzual & Charlot (2003) yield values of \mathcal{K}_{FUV} that are about 5% smaller.

Figure 3 illustrates the combined effects of the evolution of the global star formation rate and metal density on the global mean UV-to-SFR conversion factor as a function of redshift, based on the FSPS models. The dotted lines show $\mathcal{K}_{\text{UV}}(z)$ assuming a constant SFRD and metallicity, and that star formation commenced at $z = 12$. Concentrating on the FUV behavior at 1500 Å (*left*), for constant $\psi(z)$, the conversion factor is nearly constant, slightly elevated at the highest redshifts as the cosmic age gets young, particularly for lower metallicity models. The solid lines assume the functional form for the cosmic star formation history that we will derive later (Section 5.1 and eq. 15). Here, ψ increases with time from $z = 12$ to 1.7, so that the UV-emitting population is on average younger over that redshift range, leading to a more gradually declining trend in $\mathcal{K}_{\text{FUV}}(z)$ with time. The dashed line incorporates one scenario for a global change in the metallicity of the star-forming population, evolving as $Z_* = Z_{\odot} 10^{-0.15z}$ (Kewley & Kobulnicky 2007). This particular evolution is only moderately well constrained at lower redshifts, and should be taken as illustrative only, but we may certainly expect metallicities to be lower on average at higher redshift. The effects of metallicity dominate over those of age in this scenario, but the two counterbalance one another to a certain degree, so that $\mathcal{K}_{\text{FUV}}(z)$ changes by less than 20%. At 2800 Å (*right*), the redshift dependence of $\mathcal{K}_{\text{NUV}}(z)$ is stronger, particularly at $z < 2$ as the global SFRD declines with time, although this may be partially canceled by the effects of metallicity evolution. This is an example of why shorter FUV wavelengths should be preferred for deriving galaxy star formation rates.

In this review, we adopt a constant FUV conversion factor $\mathcal{K}_{\text{FUV}} = 1.15 \times 10^{-28} M_{\odot} \text{yr}^{-1}$

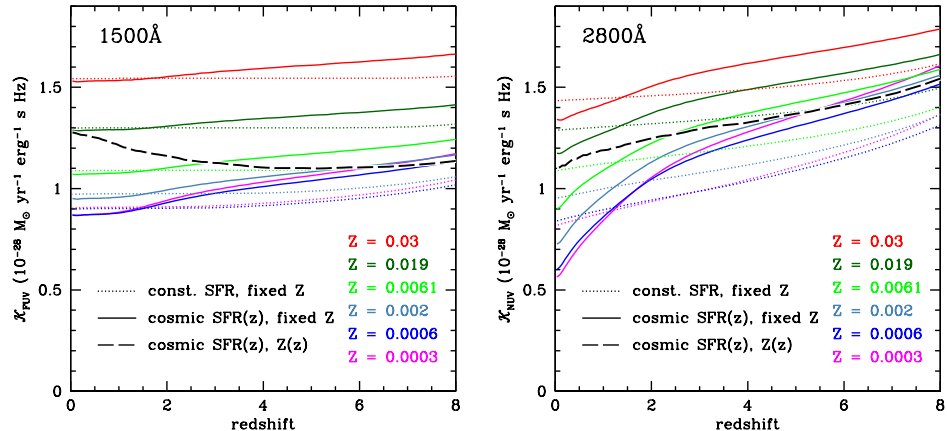


Figure 3: Age and metallicity dependence of the SFR to UV luminosity ratio ($= \mathcal{K}$, eq. 10) for a stellar population with a Salpeter IMF in the range $0.1 - 100 M_{\odot}$, using the spectral population synthesis models of Conroy et al. (2009). *Dotted lines*: constant SFR (starting at $z = 12$), fixed stellar metallicity. *Solid lines*: cosmic SFR density (eq. 15, again starting at $z = 12$), fixed stellar metallicity. *Dashed lines*: cosmic SFR density, stellar metallicity evolving as $Z_* = Z_{\odot} 10^{-0.15z}$ (Kewley & Kobulnicky 2007). The left- and right-hand panels show this relation at 1500 \AA and 2800 \AA , respectively.

$\text{erg}^{-1} \text{ s Hz}$ (we will typically leave out the units) as a compromise value based on the evolutionary scenario from Figure 3. The widely used value from Kennicutt (1998) (and based on the calibration by Madau et al. 1998b), $\mathcal{K}_{\text{FUV}} = 1.4 \times 10^{-28}$, is 20% larger than our calibration. Other recent analyses based on the GALAXEV libraries have also found lower mean conversion factors, both for low- and high-redshift galaxy populations (e.g., Salim et al. 2007; Haardt & Madau 2012). The FUV conversion tabulated in Kennicutt & Evans (2012) (from Murphy et al. 2011), if rescaled from the Kroupa IMF to Salpeter, is very close to the $z = 0$, solar metallicity value of $\mathcal{K}_{\text{FUV}}(z)$ in Figure 3, but our somewhat smaller value should be more representative for the peak era of cosmic star formation at high redshift. Some authors express FUV luminosity as $L_{\text{FUV}} = \nu L_{\nu}$ in solar units. In this case $\mathcal{K}_{\text{FUV}} = 2.2 \times 10^{-10} M_{\odot} \text{ yr}^{-1} L_{\odot}^{-1}$ at 1500 \AA , and the conversion factor will depend on wavelength.

Figure 4 (*left*) shows the ratio of \mathcal{K}_{FUV} for the Chabrier or Kroupa IMFs to that for Salpeter, as a function of age for a constant star formation rate, calculated with FSPS. This ratio is nearly constant, varying by only 5% with age and 3% over a factor of 100 in metallicity. Where necessary to convert SFRs from the literature from Chabrier or Kroupa IMFs to Salpeter, we divide by constant factors of 0.63 (Chabrier) or 0.67 (Kroupa). Similarly, Figure 4 (*right*) examines mass-to-light ratios for an SSP as a function of age, in various bandpasses, comparing values for the Chabrier or Kroupa IMFs to Salpeter. Again, these ratios are fairly constant with age⁴ and have very little dependence on the bandpass.

⁴ The similar time dependence of M/L for the “bottom-light” Chabrier or Kroupa IMFs to that for the Salpeter IMF is something of a coincidence (or a conspiracy). The rate of luminosity evolution for an SSP depends on the logarithmic IMF slope at masses greater than $1 M_{\odot}$, and is faster for the flatter $x = 1.3$ (Kroupa or Chabrier) than for the Salpeter value $x = 1.35$. However, the evolution of the recycled mass fraction is also faster for the Kroupa and Chabrier IMFs because their low-mass turnovers give them smaller mass fractions of long-lived stars. These two effects roughly cancel for $x = 1.3$, resulting in a time dependence for M/L that is nearly the same as that for the Salpeter IMF. For an SSP with a “bottom-

In other words, the color evolution for an SSP with Chabrier or Kroupa IMFs is very similar to that for Salpeter, with a roughly constant offset in M/L . The dependence on metallicity (not shown) is very weak. To rescale stellar masses from Chabrier or Kroupa to Salpeter, we divide by constant factors 0.61 and 0.66, respectively.

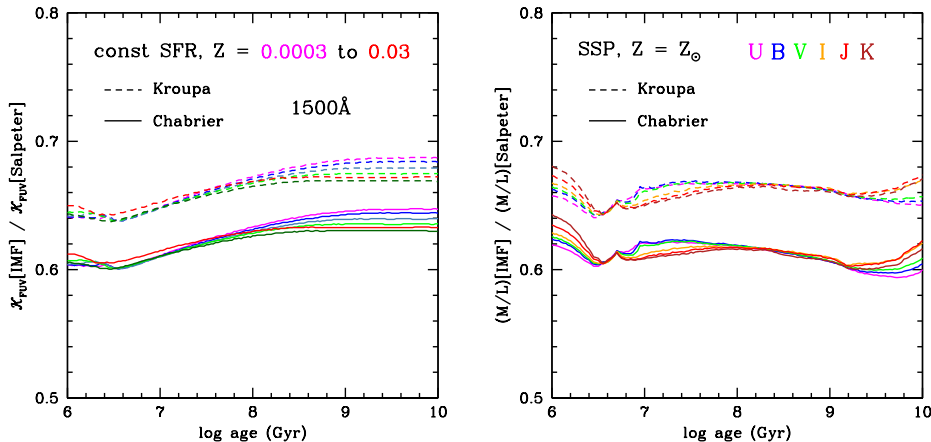


Figure 4: *Left panel:* The ratio of SFR/ L_{FUV} conversion factors \mathcal{K}_{FUV} (eq. 10) for Chabrier or Kroupa IMFs to that for a Salpeter IMF (0.1 to $100 M_{\odot}$), for a constant star formation rate, and for various metallicities, computed with the FSPS models of Conroy et al. (2009). The difference in this conversion factor varies only slightly with age or metallicity over the ranges shown here. *Right panel:* Ratio of mass-to-light ratios for a simple stellar population as a function of age, for various bandpasses from the near-UV through near-IR, comparing values for Chabrier and Kroupa IMFs to Salpeter. This factor also has only a small dependence on age, bandpass, or metallicity (the latter not shown here).

The greatest drawback for UV measurements of star formation is the obscuring effect of dust. Extinction is strong in the UV, so even modest amounts of dust can dramatically suppress the emerging UV flux. Dust re-emits the absorbed energy in the infrared, which we will discuss in the next section. A reliable measurement of star formation rates from UV light must either correct for the effects of dust absorption, or measure the absorbed energy directly through infrared emission. We will return to the relation between UV dust attenuation and IR emission in § 3.1.3 below.

3.1.2 INFRARED EMISSION The energy that dust absorbs from the UV is re-radiated at mid- and far-infrared wavelengths, making infrared observations another important tool for measuring star formation rates. The effect of dust extinction at far-infrared wavelengths is generally regarded as being negligible, although in the mid-infrared extinction can still be relevant for the most deeply buried star formation and AGN. The total infrared luminosity (L_{IR} , usually defined as being integrated over the wavelength range 8 to $1000 \mu\text{m}$) is effectively a measurement of the energy that was absorbed by dust, mainly at UV wavelengths. Since most UV emission comes from star formation, the IR luminosity is often interpreted as being directly proportional to the absorbed fraction of the energy from star formation. However, active nuclei can also produce strong UV emission, again often in

light” IMF with a Salpeter slope $x = 1.35$, the ratio of M/L compared to that for a Salpeter IMF would decrease by about 16% over about 5 Gyr, and a constant IMF rescaling factor for derived stellar masses would be inappropriate.

dusty environments, and may contribute to IR emission by heating dust in the torus and clouds surrounding the AGN. Older stellar populations can also heat dust that is present in the interstellar medium of a galaxy, contributing to the far-IR emission. This is important particularly for “mature” galaxies with low current star formation rates in the nearby universe: for a galaxy like our Milky Way, perhaps half of the far-infrared emission comes from dust heated by older stars, not from young star-forming regions (Lonsdale Persson & Helou 1987). However, for very actively star-forming galaxies without AGN it is generally assumed that most of the IR emission arises from new star formation. Ideally, a galaxy’s total infrared luminosity would be measured by fitting a dust emission model to observations at several wavelengths, hopefully spanning the peak of dust emission. In practice, however, such multi-wavelength data are often unavailable, and astronomers frequently use an SED template, often derived from observations of local galaxies, to extrapolate from a single observed flux density at some mid- or far-IR wavelength, not necessarily close to the dust emission peak, to a total L_{IR} . Variations in the dust emission properties from galaxy to galaxy can then lead to significant uncertainties in this bolometric correction, and hence in the estimation of star formation rates.

The spectrum of dust emission is fairly complex, arising from various components heated to different temperatures. Most of the dust mass in a galaxy is usually in the form of relatively cold dust (15-60 K) that contributes strongly to the emission at far-infrared and submillimeter wavelengths (30-1000 μm). Dust at several different temperatures may be present, including both colder grains in the ambient ISM and warmer grains in star-forming regions. Emission from still hotter, small-grain dust in star-forming regions, usually transiently heated by single photons and not in thermal equilibrium, can dominate the mid-infrared continuum ($\lambda < 30 \mu\text{m}$) and may serve as a useful star formation rate indicator (e.g., Calzetti et al. 2007). The mid-infrared spectral region (3–20 μm) is both spectrally and physically complex, with strong emission bands from polycyclic aromatic hydrocarbons (PAH), and absorption bands, primarily from silicates. The strength of PAH emission can depend strongly on ISM metallicity and radiation field intensity (e.g., Engelbracht et al. 2005, 2008; Smith et al. 2007). Strong silicate absorption features are seen when the column density of dust and gas is particularly large toward obscured AGN and perhaps even nuclear starburst regions. AGN themselves may contribute strong continuum emission from warm dust, and can dominate over star formation at mid-infrared wavelengths, whereas in the far-infrared their role is less prominent.

The Infrared Space Observatory (*ISO*) and the *Spitzer Space Telescope* were the first telescopes with mid-infrared sensitivities sufficient to detect galaxies at cosmological redshifts. In particular, *Spitzer* observations at 24 μm with the MIPS instrument were very sensitive, capable of detecting “normal” star-forming galaxies out to $z \approx 2$ in modest integration times. *Spitzer* was also very efficient for mapping large sky areas, and had a 24 μm beam size small enough (5.7 arcsec) to reliably identify faint galaxy counterparts to the infrared emission. However, only a fraction of the total infrared luminosity emerges in the mid-infrared, and as we have already noted it is a complicated spectral region, leading to large and potentially quite uncertain bolometric corrections from the observed mid-infrared flux to the total infrared luminosity. At $z \approx 2$, where 24 μm observations sample rest-frame wavelengths around 8 μm , where the strongest PAH bands are found, spectral templates based on local galaxies span more than an order of magnitude in the ratio $L_{\text{IR}}/L_{8\mu\text{m}}$ (e.g., Chary & Elbaz 2001; Dale & Helou 2002; Dale et al. 2005). One must have more information about the type of galaxy being observed to be confident choosing an appropriate template to convert the observed mid-IR luminosity to L_{IR} or a star formation rate.

The far-infrared thermal emission is a simpler and more direct measurement of star formation energy. *ISO* and *Spitzer* offered only relatively limited far-infrared sensitivity for deep observations, in part due to their large beam sizes that resulted in significant confusion and blending of sources and in difficulty localizing galaxy counterparts. The *Herschel* space observatory dramatically improved such observations: its 3.5m mirror diameter provided a PSF FWHM small enough to minimize confusion and to identify source counterparts in observations from 70 to 250 μm , although at the longest wavelengths of the *Herschel* SPIRE instrument, 350 and 500 μm , confusion becomes severe. *Herschel* observations can directly detect galaxies near the peak of their far-infrared dust emission: dust SEDs typically peak at 60-100 μm in the rest frame, within the range of *Herschel* observations out to $z < 4$. Temperature variations in galaxies do lead to variations in the bolometric corrections for observations at a single wavelength, but these differences are much smaller than for mid-IR data, generally less than factors of 2.

Despite *Herschel's* far-IR sensitivity, in general deep *Spitzer* 24 μm observations still detect more high- z sources down to lower limiting infrared luminosities or star formation rates. At $z \approx 2$, the deepest *Herschel* observations only barely reach to roughly L_{IR}^* (the characteristic luminosity of the “knee” of the infrared luminosity function), leaving a large fraction of the total cosmic SFRD undetected, at least for individual sources, although stacking can be used to probe to fainter levels. Deep *Spitzer* 24 μm observations detect galaxies with star formation rates several times lower, and many fields were surveyed to faint limiting fluxes at 24 μm during *Spitzer's* cryogenic lifetime. Therefore there is still value in trying to understand and calibrate ways to measure star formation from deep mid-infrared data, despite the large and potentially uncertain bolometric corrections.

In practice, observations of IR-luminous galaxies detected at high redshift with both *Spitzer* and *Herschel* have demonstrated that the IR spectral energy distributions for many galaxies are well-behaved, and that variations can be understood at least in part. Several pre-*Herschel* studies (Papovich et al. 2007; Daddi et al. 2007; Magnelli et al. 2009, 2011) compared 24 μm observations of distant galaxies to other SFR tracers, including *Spitzer* far-IR measurements (either individual detections or stacked averages) and radio emission. On average, the mid- to far-IR flux ratios for galaxies at $z \lesssim 1.3$ match those predicted by local IR SED templates like those of Chary & Elbaz (2001), implying that 24 μm -derived SFRs should be reliable. However, at higher redshift, $1.3 < z < 2.5$, the 24 μm fluxes were brighter than expected relative to the far-IR or radio data; i.e., SFRs derived from 24 μm data using local SED templates would be systematically overestimated at $z \approx 2$. This result was upheld by early *Herschel* studies (Nordon et al. 2010; Elbaz et al. 2010). In a joint analysis of the IR SED properties of both nearby and high redshift IR-luminous galaxies, Elbaz et al. (2011) provided an explanatory framework for these observations in terms of the distinction between a majority population of galaxies obeying a “main sequence” correlation between their star formation rates and stellar masses, and a minority “starburst” population with substantially higher star formation rates per unit mass (or specific star formation rate, sSFR). Locally, starburst galaxies have more compact, high surface density star forming regions, while normal disk galaxies on the star-forming main sequence have star formation distributed on larger scales with lower surface density. Starbursts also have warmer average dust temperatures and a significantly larger ratio between their far-IR and 8 μm rest-frame luminosities than those of the main sequence disk galaxies. Locally, most luminous and ultraluminous infrared galaxies (LIRGs and ULIRGs, with $L_{\text{IR}} > 10^{11} L_{\odot}$ and $> 10^{12} L_{\odot}$, respectively) are merger-driven starbursts, but at $z \approx 2$ where *globally* the star formation rates and sSFRs of galaxies are much larger, the majority of LIRGs and ULIRGs are

“normal” main sequence galaxies. Their infrared SEDs are more nearly similar to those of ordinary, local star-forming spiral galaxies, with smaller bolometric corrections from observed $24\ \mu\text{m}$ data (rest frame $\lambda \approx 8\ \mu\text{m}$) than those predicted by SED templates designed to match local LIRGs and ULIRGs. Elbaz et al. (2011) construct a “universal” main sequence SED from the ensemble of high- z *Spitzer* and *Herschel* photometry for galaxies in the GOODS fields at $0.3 < z < 2.5$. This leads to consistent total IR luminosities for the large majority of galaxies over that redshift range. Although no single template can be used to accurately derive L_{IR} or SFR from mid-IR observations for all galaxies, we now have a better understanding of how this can be done on average, which may be sufficient for deriving the global redshift evolution of the infrared luminosity density or its corresponding SFRD. Rodighiero et al. (2011) (see also Sargent et al. 2012) have shown that starbursts (whose IR SEDs deviate significantly from those of the main sequence population) account for only 10% of the global SFRD at $z \approx 2$. With the data now in hand from *Herschel* and *Spitzer*, a broad understanding of the evolving IR luminosity function and luminosity density, at least at $0 < z < 2.5$, seems within reach.

Mid- and far-infrared observations require space-based telescopes, but at submillimeter and millimeter wavelengths observations can once again be made from the ground within certain atmospheric transmission windows. The advent of submillimeter bolometer array cameras like SCUBA on the JCMT revolutionized the field, and led to the first detections of a large population of ULIRGs at high redshift (e.g., Smail et al. 1997; Hughes et al. 1998; Barger et al. 1998). Until recently, only the most luminous high- z objects could be readily detected, but the new ALMA interferometer will improve detection sensitivities by more than an order of magnitude, albeit over small fields of view. As was noted earlier, submillimeter observations measure emission beyond the peak of dust emission, where flux is declining steeply with wavelength in the Rayleigh-Jeans part of the spectral energy distribution. This leads to a negative K correction, so strong that it cancels out the effects of distance: a galaxy with a given IR luminosity will have roughly constant submillimeter flux if it is observed at any redshift $1 < z < 10$. On the other hand, the bolometric corrections from the observed submillimeter wavelengths to the total infrared luminosities are large, and depend strongly on dust temperature. This can lead to significant uncertainties interpreting submillimeter fluxes from high-redshift sources, and a bias toward detecting galaxies with the coldest dust emission.

By analogy with equation (10), we express the conversion from IR luminosity (L_{IR}) to ongoing star formation rate as:

$$\text{SFR}_{\text{IR}} = \mathcal{K}_{\text{IR}} \times L_{\text{IR}}, \quad (11)$$

where L_{IR} is the infrared luminosity integrated over the wavelength range from 8 to $1000\ \mu\text{m}$. Here, it is assumed that the IR emission is entirely due to recent star formation, but in practice, as we have already noted, AGN and older stars can contribute to dust heating. Note also that if the net dust opacity to young star-forming regions in a galaxy is not large, and if a significant amount of UV radiation emerges, then the star formation rate derived from the IR luminosity will only represent a fraction of the total. Hence, we write SFR_{IR} in equation (11) to indicate that this is only the dust-obscured component of the star formation rate. For this reason, some authors advocate summing the SFRs derived from the observed IR and UV luminosity densities, the latter *uncorrected* for extinction. Once again, we calibrate the conversion factor \mathcal{K}_{IR} using the FSPS models of Conroy et al. (2009), which also incorporate dust attenuation and re-emission. We assume simple foreground-screen dust attenuation from Calzetti et al. (2000), although the details of the dust absorption model

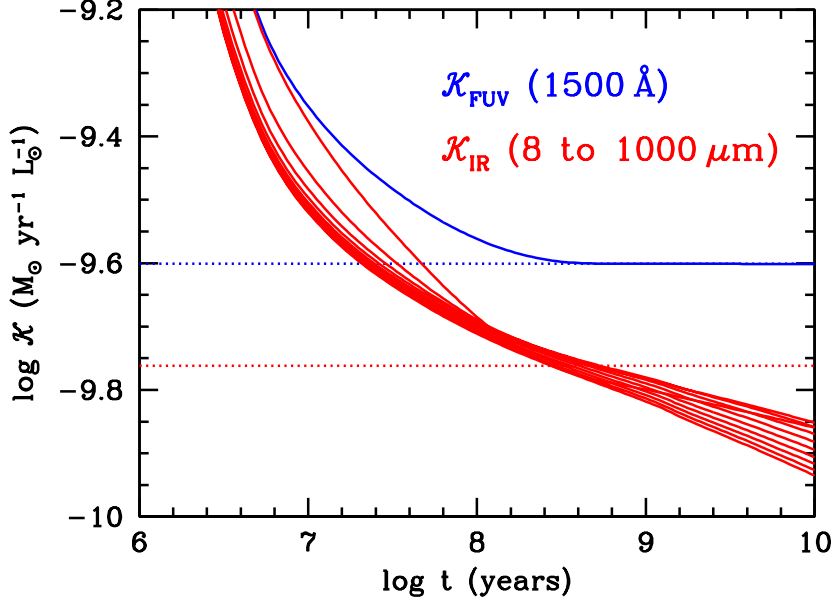


Figure 5: The SFR to luminosity ratio \mathcal{K} for dusty galaxies, in solar luminosity units, calibrated with the FSPS models of Conroy et al. (2009), assuming a constant SFR, a Salpeter IMF, and solar metallicity. The blue curve shows the FUV conversion factor \mathcal{K}_{FUV} (see §3.1.1), and the blue dotted line indicates its asymptotic value. The red curves show the FIR conversion factor \mathcal{K}_{IR} computed as per eq. 12, for 1500 Å extinction ranging from 0.055 to 5.5 magnitudes. The dotted red line indicates the value of \mathcal{K}_{IR} from Kennicutt (1998), which we also adopt here.

matter relatively little. The luminosity integrated from 8 to 1000 μm depends only mildly on the detailed dust emission parameters (essentially, the dust temperature distribution) for a broad range of reasonable values. Because the dust luminosity is primarily reprocessed UV emission from young star formation, the conversion factor \mathcal{K}_{IR} will also depend on the details of the star formation history and on metallicity. In practice, we may expect that galaxies with substantial extinction and bolometrically dominant dust emission are unlikely to have low metallicities; here we assume solar metallicity for our calibration. We modify equation (11) to account for both the FUV and FIR components of star formation:

$$\text{SFR}_{\text{tot}} = \mathcal{K}_{\text{FUV}} L_{\text{FUV}} + \mathcal{K}_{\text{IR}} L_{\text{IR}}, \quad (12)$$

where here L_{FUV} is the observed FUV luminosity at 1500 Å, with no correction for extinction. We use FSPS models with a Salpeter IMF, solar metallicity, and constant SFR to compute L_{FUV} and L_{IR} as a function of age for various levels of dust attenuation, and solve for \mathcal{K}_{IR} . Figure 5 shows the result of this calculation, where SFR is expressed in units of $M_{\odot} \text{yr}^{-1}$ and both the FUV and IR luminosities are expressed in solar units (with $L_{\text{FUV}} = \nu L_{\nu}$), in order to display both on the same scale. As we have seen (§3.1.1), the FUV emission reaches a steady state after about 300 Myr, and for this calculation we use this asymptotic value $\mathcal{K}_{\text{FUV}} = 2.5 \times 10^{-10} M_{\odot} \text{yr}^{-1} L_{\odot}^{-1}$ (equivalently, $\mathcal{K}_{\text{FUV}} =$

$1.3 \times 10^{-28} M_{\odot} \text{ yr}^{-1} \text{ erg}^{-1} \text{ s Hz}$). Instead, L_{IR} increases slowly (hence, K_{IR} decreases) as the optical rest-frame luminosity of longer-lived stars continues to build, some fraction of which is then absorbed by dust and re-emitted. This effect is modest, about 0.1 dex in $\log K_{\text{IR}}$ per dex in $\log t$ for this constant SFR model, and in practice older stars will likely have lower dust extinction than younger stars, further reducing this trend. At ages of a few $\times 10^8$ years K_{IR} depends very little on the total extinction. Kennicutt (1998) proposed a calibration factor $K_{\text{IR}} = 1.73 \times 10^{-10} M_{\odot} \text{ yr}^{-1} L_{\odot}^{-1}$, which is fully consistent with the models shown in Figure 5 for an age of 300 Myr. We adopt that value for this review. For luminosities measured in cgs units, we can write $K_{\text{IR}} = 4.5 \times 10^{-44} M_{\odot} \text{ yr}^{-1} \text{ erg}^{-1} \text{ s}$.

3.1.3 UV EXTINCTION AND IR EMISSION As noted earlier, dust can substantially attenuate UV emission, compromising its utility for measuring star formation rates, but also producing infrared emission which itself is a valuable tracer of star formation activity. Considerable effort has been invested in understanding the physics and phenomenology of extinction in galaxies (see Calzetti 2001 for a review). In principle, the best way to account for the effect of dust attenuation is to directly measure the energy emitted at both UV and IR wavelengths, i.e., both the luminosity that escapes the galaxy directly and that which is absorbed and re-radiated by dust. This provides a “bolometric” approach to measuring star formation rates. In practice, however, data sensitive enough to measure far-infrared luminosities of high redshift galaxies are often unavailable. *Herschel* greatly advanced these sorts of observations, but its sensitivity, while impressive, was still only sufficient to detect galaxies with high star formation rates, $> 100 M_{\odot} \text{ yr}^{-1}$, at $z > 2$.

For star-forming galaxies with moderate extinction at $z > 1$, optical photometry measuring rest-frame UV light is obtained much more easily than suitably deep far-infrared, submillimeter or radio data, and is typically much more sensitive to star formation (Fig. 1). So, it is tempting to try to infer SFRs from rest-frame UV observations alone, but this requires reliable estimates of dust extinction corrections. For example, Lyman break galaxies (LBGs) are a UV-selected population of star-forming high redshift galaxies. Their selection would favor relatively low extinction, but even LBGs are quite dusty: Reddy et al. 2012 use *Herschel* observations to determine that, on average, 80% of the FUV emission from typical ($\sim L_{\text{FUV}}^*$) LBGs at $z \approx 2$ is absorbed by dust and re-radiated in the far-infrared. Many more massive galaxies with high star formation rates have still greater extinction. So-called Dust-Obscured Galaxies (DOGs, Dey et al. 2008) have mid-IR to UV flux density ratios > 1000 (typically corresponding to $L_{\text{IR}}/L_{\text{FUV}} > 100$, Penner et al. 2012), and are quite common, contributing 5%–10% of the SFRD at $z \approx 2$ (Pope et al. 2008); many of these are nearly or entirely invisible in deep optical images.

Nevertheless, the widespread availability of rest-frame UV data for high redshift galaxies encourages their use for measuring the cosmic star formation history. Presently, at $z \gg 2$, there is little alternative: even the deepest *Spitzer*, *Herschel*, radio or submm surveys can only detect the rarest and most ultraluminous galaxies at such redshifts, whereas deep optical and near-infrared surveys have now identified samples of thousands of UV-selected star-forming galaxies out to $z \approx 7$ and beyond.

Attempts to measure and correct for dust extinction in high- z galaxies have generally used the ultraviolet spectral slope (designated β) as a measure of UV reddening, and have adopted empirical correlations between UV reddening and UV extinction. Calzetti et al. (1994, 2000) used IUE and optical spectroscopy to derive an empirical, average dust attenuation curve for a sample of local UV-bright star-forming galaxies. Meurer et al. (1999) (later updated by Overzier et al. 2011) used UV and far-IR data for a similar local sample to empirically

calibrate the relation between UV reddening (β) and UV extinction ($\text{IRX} \equiv L_{\text{IR}}/L_{\text{FUV}}$, which can be directly related to A_{FUV}). The reasonably tight $\text{IRX}-\beta$ relation obeyed by the local UV-bright galaxies is broadly consistent with the Calzetti attenuation law, hence reinforcing its popularity. However, other local studies showed clearly that some galaxies deviate from these relations. Goldader et al. (2002) found that nearby ULIRGs deviate strongly from the Meurer $\text{IRX}-\beta$ relation, with very large values of IRX but often with relatively blue UV spectral index β . This was interpreted to mean that the observed UV light from local ULIRGs is relatively unreddened star formation in the host galaxy that is unrelated to the bolometrically dominant star formation, which is entirely obscured from view at UV/optical wavelengths, and detected only in the far-IR. Instead, observations of ordinary spiral galaxies (Calzetti 1997; Kong et al. 2004; Buat et al. 2005) measured redder values of β for a given IRX . This is generally taken as evidence that light from older and less massive stars contributes significantly to the near-UV emission, leading to redder UV colors for reasons unrelated to extinction. In general, different relative distributions of stars and dust can lead to different net attenuation properties. Extinction can easily be patchy, as winds from star-forming regions can blow away dust on certain time scales, while other regions that are younger or more deeply embedded in the galaxy’s ISM remain more heavily obscured. Dust heating also depends on geometry, leading to different distributions of dust temperatures and hence different emission spectra at infrared and submillimeter wavelengths.

At high redshift there are only relatively limited tests of the relation between UV reddening and extinction. Reddy et al. (2004, 2006, 2010, 2012) have compared various SFR tracers (including radio, *Spitzer* $24\mu\text{m}$, and *Herschel* $100\text{-}160\mu\text{m}$ emission) to show that Calzetti/Meurer UV extinction laws are broadly appropriate for the majority of L^* LBGs at $z \approx 2$, although they also found evidence for systematic deviations for galaxies with the largest SFRs ($> 100 M_{\odot} \text{ yr}^{-1}$), which, like local ULIRGs, show “greyer” effective attenuation (i.e., less UV reddening for their net UV extinction), and for the youngest galaxies, which show stronger reddening for their net FUV extinction, perhaps because of metallicity or geometric effects that steepen the wavelength dependence of the UV reddening function compared to the Calzetti law. Daddi et al. (2007) and Magdis et al. (2010) also found broad consistency between UV-based and IR- or radio-based star formation rate measurements for samples at $z \approx 2\text{-}3$, assuming Calzetti attenuation (although, see Carilli et al. 2008). However, studies that have selected galaxies primarily based on their IR emission have tended to find significant deviations from Meurer/Calzetti attenuation, generally in the sense that UV-based SFRs using Meurer/Calzetti UV slope corrections would significantly underestimate total SFRs (e.g., Chapman et al. 2005; Papovich et al. 2007). More generally, such studies have found that differently-selected populations may obey systematically different net dust attenuation relations depending on the properties of the galaxies (Buat et al. 2012; Penner et al. 2012).

Therefore, we must remain cautious about star formation rates derived from UV data alone, even when estimates of UV reddening are available. The current evidence suggests that these may work well *on average* for UV-bright LBGs with relatively low reddening, but may fail for other galaxies, including the most IR-luminous objects that dominate the most rapidly star-forming galaxy population. Star formation that is obscured by too much dust, e.g., in compact starburst regions, will be unrecorded by UV observations, and can only be measured directly with deep infrared, submillimeter or radio measurements.

3.1.4 OTHER INDICATORS: NEBULAR EMISSION LINES, RADIO AND X-RAY EMISSION

Star formation also produces nebular line emission from excited and ionized gas in HII regions. Recombination lines of hydrogen such as $H\alpha$ and $Ly\alpha$ are often used to measure star formation rates, since they have a close relation to photoionization rates that are mainly due to intense UV radiation from OB stars. Hence, they trace massive star formation quite directly, although the presence of AGN can also contribute to these lines. Other lines from heavier elements, such as [OII] 3727 Å or [OIII] 5007 Å, have been used, but tend to have more complex dependence on ISM conditions such as metallicity or excitation. Emission lines are also subject to absorption by dust in the star-forming regions. This is particularly true for $Ly\alpha$, which is a resonance line, scattered by encounters with neutral hydrogen atoms, which can greatly increase the path length of its travel, and hence increase the likelihood that it may encounter a dust grain and be absorbed. Overall, $H\alpha$ is regarded as the most reliable among the easily accessible nebular SFR tracers (e.g., Moustakas et al. 2006). Weaker but less extinguished hydrogen lines in the near-infrared, like Paschen α , can in principle be very useful for measuring star formation rates in dusty galaxies, but are generally accessible only at very low redshift, although the *James Webb Space Telescope* (*JWST*) will open the possibility for measuring these for significant numbers of galaxies at cosmological distances.

Radio emission is also correlated with star formation, as supernova-accelerated electrons emit non-thermal radiation at centimeter wavelengths; thermal (free-free) emission from electrons in HII regions can also contribute, particularly at higher frequencies (>5 GHz). The physics is somewhat complicated and not entirely understood, but a remarkably tight correlation is observed between radio emission and far-infrared emission in local galaxies spanning many orders of magnitude in luminosity (e.g., Condon 1992; Yun et al. 2001). Radio emission is free from dust extinction, and thus offers a relatively unbiased tracer of star formation. However, it is difficult to obtain radio observations deep enough to detect ordinary star-forming galaxies at high redshift, although recent upgrades to the Karl G. Jansky VLA have significantly improved its sensitivity. AGN can also contribute to radio emission, occasionally dominating for radio-loud AGN (which are, however, a minority population). Radio emission should also be suppressed at earlier cosmic epochs, as electrons should lose energy by inverse Compton scattering off microwave background photons whose energy density increases at high redshift. Recent studies have found little evidence for redshift evolution in the far-infrared to radio correlation (Appleton et al. 2004; Ivison et al. 2010a,b; Sargent et al. 2010a,b; Mao et al. 2011).

Even X-rays have been used to trace star formation rates. X-rays are typically regarded as a quintessential signature of AGN activity in galaxies, but they are also produced by young stellar populations, notably by X-ray binaries. In the absence of an AGN, X-ray emission may be measured from individual star-forming galaxies out to $z \approx 1$ in the deepest *Chandra* fields, and stacking measurements have been used to reach fainter fluxes in studies of UV-selected galaxies, with detections at $1 < z < 4$ and upper limits at higher redshifts (Reddy & Steidel 2004; Lehmer et al. 2005; Laird et al. 2005, 2006; Basu-Zych et al. 2013). However, the proportionality between X-ray luminosity and star formation rate may vary with stellar population age and other parameters that could affect the mix of low- and high-mass X-ray binaries present in a galaxy, and various calibrations that differ significantly have been published (e.g., Ranalli et al. 2003; Persic et al. 2004). Overall, since most of the cosmic X-ray background arises from AGN (see Brandt & Hasinger 2005 for a review), it seems that the value of X-rays for measuring the cosmic star formation history is limited, and we will not discuss this method further in this review.

3.2 “Weighing” Stellar Mass

While hot young stars emit most of their energy at UV wavelengths, the cooler, low-mass stars that dominate the stellar mass of a galaxy emit most of their light at red optical and near-infrared wavelengths. If we examine the spectral energy distribution of an evolving simple stellar population, from ages older than 10^9 years, the bulk of the luminosity (in λf_λ energy units) is emitted in a broad plateau between 0.4 and $2.5 \mu\text{m}$, peaking at $\sim 1 \mu\text{m}$ for ages > 2 Gyr.⁵ The effects of dust extinction are also greatly reduced at near-infrared wavelengths: for the Calzetti attenuation, the extinction (in magnitudes) A in the K -band is $10\times$ smaller than that in the V -band, and $25\times$ smaller than that at 1600 \AA .

The luminosity, and hence the mass-to-light ratio, of a stellar population evolves very steeply with time at UV and blue wavelengths, as young stars quickly evolve off the main sequence, but more slowly at red and near-infrared wavelengths. Therefore, observations in the near-infrared rest frame more nearly trace the integrated stellar mass of a galaxy, but we cannot neglect the effects of evolution: the flux at $1 \mu\text{m}$ still changes by more than an order of magnitude as a stellar population ages from 0.1 to 10 Gyr (see, e.g., Fig. 9 from Bruzual & Charlot 2003). Therefore, we need to do more than simply measure the near-infrared luminosity to infer a stellar mass.

In effect, astronomers use the colors or spectral energy distribution of a galaxy to infer the expected mass-to-light ratio at some wavelength (preferably in the red or near-infrared), and then multiply the observed luminosity by M/L to estimate the stellar mass (M_*). The most common method is to fit spectral templates generated by stellar population synthesis models to broad-band photometry in whatever bands are available that span rest-frame UV to near-IR wavelengths, where stellar photospheric emission dominates the galaxy light. Generally speaking, a large suite of models is generated that span a wide range of stellar population parameters, including the past SFH, age, metallicity, and dust attenuation. The IMF is typically fixed, since there is almost no photometric signature that can usefully constrain it. The suite of models is redshifted to match a galaxy of interest, convolved by the filter bandpasses to generate synthetic broad band fluxes, and these are then fit to the photometry, allowing the luminosity normalization to vary, and minimizing χ^2 or some other likelihood parameter. The unnormalized models have a specified unit mass, and therefore the normalization of the best-fitting model provides the best estimate of the galaxy’s stellar mass, given the range of input parameters that were allowed.

In principle, this method can be used to constrain other stellar population parameters such as the galaxy’s age, star formation rate, or the degree of extinction that is present. In practice, the fitting results for various parameters are often quite degenerate. For example, age, extinction, and metallicity all affect the integrated colors of a galaxy, and therefore the derived values of these parameters tend to be highly co-variant: a galaxy may be red because it is old, dusty, or very metal rich. With very good photometry, particularly spanning a large range of wavelength and with many bandpasses that can more accurately sample the detailed spectral shape (e.g., measuring relatively sharp age-sensitive features like the Balmer or 4000 \AA breaks), these constraints can be improved, but it is hard to avoid significant degeneracies. Careful practitioners may consider joint probability distributions for models that fit with acceptable likelihood. The stellar mass tends to be the best-constrained parameter, largely because the degeneracies in other parameters all tend to affect the net M/L of the model in similar ways. Redder colors from age, dust, or metallicity all tend to affect M/L to a similar

⁵In f_ν flux density or AB magnitude units, the SED peak is at approximately $1.6 \mu\text{m}$, where there is a minimum in the H^- opacity of cool stellar atmospheres.

(but not identical) degree. So, while parameters like age or reddening may be individually uncertain, the net M/L of acceptable models does not vary so much, and thus the total mass is well constrained.

Other than the choice of the IMF, the largest uncertainty that affects the derived stellar mass is usually the necessarily imperfect knowledge of the galaxy’s past star formation history. Fundamentally, more recently formed stars can easily outshine older stars and dominate the observed light, even at red wavelengths. The observed photometry may be dominated by the younger starlight, while the actual galaxy mass may be dominated by older stars that are lost in the glare of the younger stars (“outshining”) and thus have little impact on the choice of the best-fitting models. The model fitting therefore often underestimates the age of the galaxy or the potential contribution of older stars to the mass, and hence may also underestimate the mass. If the actual star formation history were very well known this might not be a problem, but in practice this is almost never the case. For example, the models used to fit the photometry are often assumed to have smoothly-varying star formation rates, but the actual star formation histories of real galaxies can be complex and non-monotonic, fluctuating with time and perhaps punctuated by short-duration bursts. Even if very large suites of models with complex star formation histories are considered, outshining will tend to ensure that recently formed stars tend to drive the model fitting, while the mass in older stars is poorly constrained. There is very little way to realistically constrain the distribution of allowable past star formation histories for real galaxies, especially at high redshift, and this remains a basic limitation when deriving stellar masses.

In practice, these SFH degeneracies are largest for galaxies with recent star formation. For galaxies which have not formed stars in a long while (say > 1 Gyr), or for which the current SFR is small compared to the stellar mass (often quantified by the sSFR, the outshining is small, and thus so is the resulting systematic uncertainty on M/L). Therefore, stellar masses for present-day elliptical galaxies, which are old with little or no on-going star formation, or even ordinary spiral galaxies like the Milky Way, tend to be reasonably well-constrained, while those for very actively star-forming galaxies are less certain. As an example, Papovich et al. (2001) fit models to *HST* WFPC2 and NICMOS photometry for faint Lyman break galaxies at $z \approx 2.5$ in the HDF-North. When using models with smoothly varying star formation histories, they found stellar mass uncertainties to be $\sigma(\log M_*) < 0.5$ dex, with typical uncertainties of 0.25 dex, i.e., less than a factor of 2. However, if they considered “maximal M/L ” models, which allowed for as much older stellar mass as possible within the χ^2 fitting constraints, formed at $z = \infty$, the masses could in principle be as much as 3 to $8\times$ larger. In practice, such extreme models seem unlikely. Moreover, that early work used photometry only out to the K -band, or rest-frame wavelengths $\sim 6000 \text{ \AA}$ at $z = 2.5$. Today, deep *Spitzer* IRAC photometry routinely measures fluxes for high- z galaxies at redder rest-frame wavelengths and can significantly improve stellar mass constraints, although even with the best data from *Spitzer* (or the *JWST* in the future) the effects of outshining fundamentally limit our certainty about stellar mass estimates for individual objects. This can only be reduced if reasonable prior assumptions can more tightly constrain the range of allowable star formation histories.

Interestingly, at very high redshifts some of these SFH uncertainties are reduced, simply because the universe is much younger. At $z > 6$ the universe is less than 1 Gyr old, and the oldest stars in galaxies must be younger than that; this sets a cap on M/L for a hypothetical unseen old population, and thus on its possible contribution to the total stellar mass. Curtis-Lake et al. (2013) provide a recent and detailed discussion of stellar

population modeling uncertainties for galaxies at $z \sim 6$.

Additionally, there is not yet complete consensus among the practitioners who create stellar population models; certain questions regarding evolutionary tracks, the contributions of certain stellar sub-populations, and the behavior of stellar populations at low and high metallicities remain a topic of debate, or are poorly calibrated by observations. One widely-recognized example of such uncertainties was highlighted by Maraston (2005), whose models featured significantly greater contributions of emission from thermally pulsating asymptotic giant branch (TP-AGB) stars to the red and near-infrared rest-frame light at SSP ages between a few hundred Myr and about 2 Gyr. The enhanced red luminosity led to lower M/L at these wavelengths and redder colors, with potentially quite significant effects (factors of 2 or more) in derived stellar masses for galaxies dominated by stars in this age range. While such populations may not dominate in most present-day galaxies, at $z \approx 2-4$ when the universe itself was only a few Gyr old it is clear that their role must be accurately modeled in order to ensure proper estimates of stellar masses. Maraston et al. (2006) found that this could reduce derived stellar masses by $\sim 60\%$ on average for K -band-selected star-forming galaxies at $z \approx 2$ compared to results computed using the popular Bruzual & Charlot (2003) models. Those authors released new models in 2007 which featured enhanced TP-AGB emission, although in recent conference presentations they have argued again for weaker TP-AGB emission, more similar to that in the older models (Bruzual et al. 2013). In this case, a lot hangs on the sparseness of data available to empirically calibrate the emission and evolution of TP-AGB stars, since there is no completely satisfactory way to compute this contribution on theoretical principles.

4 TRACING THE GALAXY EMISSION HISTORY WITH LARGE SURVEYS

Over the past 18 years, there has been a sea of published measurements of the cosmic SFRD or SMD at many different redshifts, using different datasets and methods. Much of the observational work has been carried out in deep survey fields that have accumulated outstanding multiwavelength data for this purpose, covering different angular scales to different depths (Fig. 6). We will not attempt a comprehensive review of this literature, but will highlight key datasets and analyses from roughly the first decade of cosmic star formation rate measurements (1996-2006), and then focus on the most important or extensive recent measurements that we will use in our analysis in § 5. Hopkins (2004) and Hopkins & Beacom (2006) provide an extensive compilation of SFRD measurements up to 2006, while Wilkins et al. (2008a) summarize SMD derivations through 2007. Other authors have also compiled these data more recently (e.g., Behroozi et al. 2013).

We note in passing that the number of papers that present measurements of the cosmic SFR history vastly exceeds the number of different datasets that have been used for this purpose. This is largely because certain well-trodden surveys like the Hubble Deep Field North, the Hubble Ultradeep Field, GOODS, and COSMOS have been used over and over again by many groups, or by the same groups who continue to refine their analyses or add new observational information. One should thus be cautious compiling results from many different studies: sometimes the analyses are independent, but the data used and the actual galaxies measured are not. For example, the star formation history of GOODS-S and COSMOS are particularly well studied by now, but true cosmic variance due to clustering in those fields will not cancel out from one analysis to another.

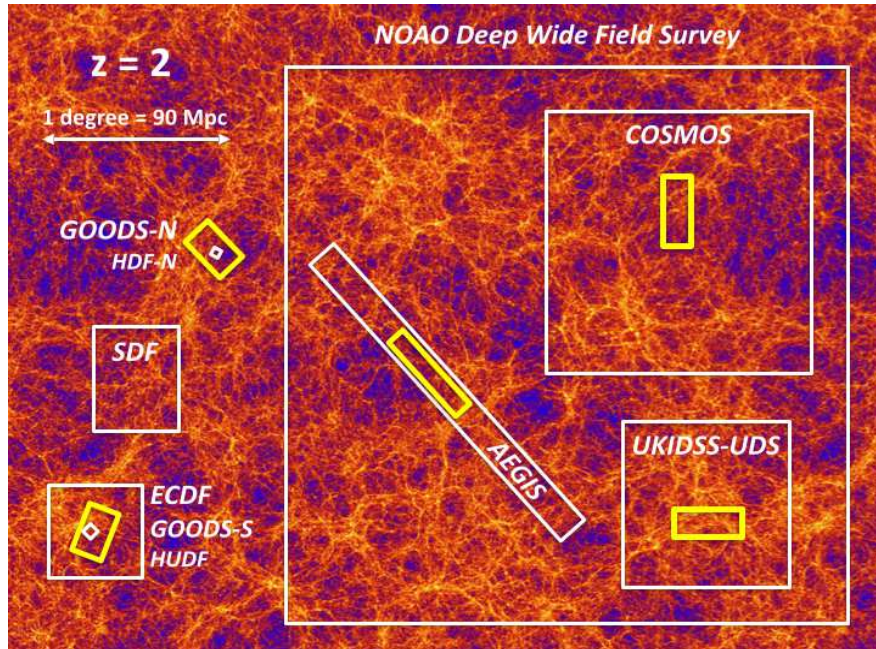


Figure 6: Relative sizes of the regions on the sky observed in several important surveys of the distant universe. The two GOODS fields, the Subaru Deep Field (SDF), and the Extended Chandra Deep Field South (ECDFS) are shown on the left. Very deep surveys like the Hubble Deep Field North (HDF-N) and the Hubble Ultradeep Field (HUDF, ACS area shown), which are embedded within the GOODS fields, can detect fainter galaxies, but cover only very tiny regions on the sky. Other surveys like the Cosmic Evolution Survey (COSMOS), the UK Infrared Deep Sky Survey (UKIDSS) Ultra-Deep Survey (UDS), the All-wavelength Extended Groth Strip International Survey (AEGIS) and the NOAO Deep Wide Field Survey cover wider regions of the sky, usually to shallower depths, i.e., with less sensitivity to very faint galaxies. However, they encompass larger and perhaps more statistically representative volumes of the universe. The yellow boxes indicate the five fields from the Cosmic Assembly Near-infrared Deep Extragalactic Legacy Survey (CANDELS), each of which is embedded within another famous survey area. The image in the background shows a cosmological N -body simulation performed within the MultiDark project (see <http://www.multidark.org/MultiDark/>), viewed at $z = 2$, more than 10 billion years ago. The colors represent the matter density distribution in a slice 43 Mpc thick, or $\Delta(z) = 0.03$ at that redshift, and all lengths are given in comoving units for $h = 0.7$. Small surveys may sample under- or over-dense regions, while larger surveys can average over density variations, but may not be sensitive to the ordinary, relatively faint galaxies that are most numerous in the universe. Averaging over larger redshift intervals than that shown in the background figure will smooth over density variations, but for any redshift binsize cosmic variance will be smaller for wider surveys, or when a survey is divided into fields sampling multiple, independent sightlines.

4.1 UV surveys

The largest number of analyses of the cosmic SFRD have used rest-frame ultraviolet continuum measurements, largely because the method is quite sensitive (see Fig. 1), and can be applied over a very broad range of redshifts. Rest-frame FUV (1500\AA) SFRs at $1.4 < z < 6$ can be measured using optical photometry that is (relatively) easily obtained with ground-based or *Hubble* imaging. The heavy use of photometric redshifts in recent years has led to much work being done from imaging data alone, with little or no spectroscopy, although in popular deep survey fields like GOODS or COSMOS the photo- z 's are typically well calibrated thanks to the widespread availability of thousands of spectroscopic measurements.

At $z < 1$, rest-frame UV measurements ideally require space-based telescopes like *GALEX* or *HST* in order to reach rest-frame wavelengths near 1500Å, but several studies have used blue or *U*-band imaging to sample mid-UV wavelengths (e.g., 2800 Å) at $z < 1$ instead.

The modern era of SFRD measurements arguably began with the analysis of Lilly et al. (1996), who were the first to combine a large and deep (for its time) spectroscopic redshift survey with multiwavelength photometry and to derive luminosity functions and luminosity densities at several different rest-frame wavelengths, including the rest-frame UV. The Canada-France Redshift Survey (CFRS) was carried out using the 4m CFHT, and mainly surveyed the universe out to $z < 1$. The available *BVIK*-band photometry permitted direct measurement of 2800 Å rest-frame luminosities at $z > 0.5$, and down to $z \approx 0.3$ with modest spectral extrapolation. Lilly et al. found that the 2800 Å luminosity density declined by about one order of magnitude from $z = 1$ to the present, which they interpreted as a steep decline in the SFRD.

Madau et al. (1996) used the then-new Hubble Deep Field (HDF) observations to extend this analysis to much higher redshift, using color-selected Lyman break galaxy samples at $\langle z \rangle = 2.75$ and 4. The deep *HST* WFPC2 photometry allowed luminosities to be measured at 1500Å in the rest frame, reaching fainter than contemporaneous ground-based LBG data at $z \approx 3$ from Steidel et al. (1996), and thus integrating further down the luminosity function. Madau et al. quoted only lower limits for the SFRD, without extrapolation to fainter luminosities (relatively small, given the depth of the HDF imaging) and without correction for dust absorption (significant, but at the time little known). Later analyses (e.g., Madau et al. 1998b; Steidel et al. 1999) fit Schechter luminosity functions to the photometric samples in order to extrapolate to total UV luminosity densities. Connolly et al. (1997) combined the optical *HST* imaging of the HDF with ground-based near-infrared imaging to carry out one of the first photometric redshift analyses that provided robust results in the redshift “gap” between the Lilly et al. and Madau et al. regimes. Taken together, the HDF measurements at $z > 1$, together with the CFRS measurements at $z < 1$, suggested a general “rise and fall” picture of the UV luminosity density, and by inference, the cosmic star formation history, peaking somewhere between $z \approx 1$ to 2.

Subsequently, various surveys extended this using other datasets or different analyses. Several groups reanalyzed the Hubble Deep Field (and later the HDF-South) data in various ways, or made use of deeper spectroscopic surveys with the *Keck* telescope. Cowie et al. (1999) and Wilson et al. (2002) combined *Keck* spectroscopy in several fields with deep *U*-band imaging to measure shorter rest-frame UV wavelengths (2000-2500Å) at $z < 1$ than were probed in the CFRS analysis of Lilly et al. (1996), and derived a shallower rate of decline in the SFRD. Wolf et al. (2005) used 17-filter intermediate and broad band imaging to obtain high quality photometric redshifts at $z < 1.25$ in the Extended Chandra Deep Field South, and analyzed the 2800 Å luminosity density evolution.

Ideally, UV rest frame observations at $z < 1$ should be done from space telescopes in order to sample shorter UV wavelengths than those used in the ground-based studies by Lilly, Wilson, Wolf and others. In early work, Treyer et al. (1998) and Sullivan et al. (2000) used the FOCA balloon-born UV telescope to measure 2000Å luminosity densities at $z \approx 0.15$. *GALEX* has since provided vastly more far-UV data, including both wide-area and deeper surveys. Wyder et al. (2005) combined *GALEX* all-sky imaging survey data with distances from the 2dF Galaxy Redshift Survey (2dFGRS) over 56 deg² to measure local ($z \approx 0.055$) luminosity functions at 1500Å and 2300 Å. Budavári et al. (2005) analyzed a similar total sky area using somewhat deeper *GALEX* data and SDSS-derived photometric redshifts to compute luminosity functions and densities at $z < 0.25$. Salim et al. (2007) and Robotham

& Driver (2011) have since analyzed much larger *GALEX* + SDSS data covering as much as 830 deg². Robotham & Driver present a straightforward derivation of the UV luminosity function and luminosity density, while Salim et al. use *GALEX* photometry as one ingredient in deriving star formation rates and the total SFRD.

Arnouts et al. (2005) combined much deeper *GALEX* observations with spectroscopy from the VIMOS VLT Deep Survey (VVDS), and derived 1500Å rest-frame luminosity functions at $0.2 < z < 1.2$. Schiminovich et al. (2005) integrated these luminosity functions to determine the 1500Å luminosity density, measuring evolution consistent with $\rho_{\text{FUV}} \propto (1+z)^{2.5}$. This remains the most direct and frequently cited *GALEX* study of far-UV luminosity densities at $z < 1$. This is somewhat surprising, as there are many more deep *GALEX* observations in fields with extensive spectroscopy (COSMOS, AEGIS, GOODS, etc.), but to our knowledge there have been no other published luminosity functions. The Arnouts/Schiminovich analysis is admirable, but in fact used only about 1000 galaxies with spectroscopic redshifts over the whole range $\Delta z = 1$, in a single field covering 0.5 deg², and hence potentially subject to cosmic variance issues. This is one area quite ripe for further exploitation of existing archival data.

HST is the only other modern space telescope with UV capabilities, particularly with the UVIS channel of the WFC3 camera. Until recently, only one 50 arcmin² field in GOODS-South has been surveyed to interesting depths for studying distant galaxies (Hathi et al. 2010; Oesch et al. 2010). At $z < 1.4$, where these data measure FUV rest-frame emission, the survey volume and counting statistics are poor. These data have also been used for Lyman break color selection at $z \approx 1.5$ to 2. The analyses generally support relatively steep UV luminosity functions, with $\alpha < -1.5$, with large uncertainties. Expanded WFC3 UVIS observations in the HUDF and GOODS-North field, recently completed, should improve these measurements somewhat. A recent WFC3-UVIS survey of gravitationally lensed galaxies behind the massive cluster Abell 1689 (Alavi et al. 2013) has been used for Lyman break color selection to unprecedentedly faint FUV luminosities at $z \approx 2$, to $M_{AB} \approx -13$, or $\sim 1000\times$ fainter than L^* at that redshift. Those authors find no turnover to the luminosity function down to those limits, and measure a faint-end slope $\alpha = -1.56 \pm 0.13$.

Cucciati et al. (2012) analyzed a larger, deeper and more complete spectroscopic sample in the same VVDS survey field studied by Arnouts et al. and Schiminovich et al. . They fit SED models to multi-band photometry from the *U* through *K*-bands to extrapolate flux density measurements to far-UV rest-frame wavelengths at $z < 1.4$. They demonstrate consistency with the *GALEX* luminosity densities from Schiminovich, but do not make direct use of the *GALEX* data. This is the largest and deepest spectroscopic sample that has been used to derive UV luminosity functions at $0 < z < 2$, but is again based on only one sightline, and requires SED extrapolation to rest frame 1500Å at lower redshifts. Tresse et al. (2007) presented a similar, earlier analysis using shallower spectroscopy in two VVDS fields.

Over many years, Steidel and collaborators have carried out an extensive campaign of *Keck* spectroscopy for Lyman break selected galaxies, especially at $z \approx 2$ and 3 (Steidel et al. 2003, 2004). Their survey covers many widely-spread sightlines, providing excellent control over cosmic variance. Among several luminosity function analyses from these data, the most recent and definitive are those of Reddy et al. (2008) and Reddy & Steidel (2009). These still rely on deep photometric color-selected samples to probe the faint end of the luminosity function, but with a degree of spectroscopic confirmation and calibration for brighter galaxies that is unmatched by any other survey. The use of UV rest-frame selection means that any LBG-based study will miss heavily dust-obscured star formation at these

redshifts, but as a measure of the evolving UV luminosity density the LBG surveys have provided the most robust method to date.

At higher redshifts, $4 < z < 7$, deep *HST* observations (discussed below) have dominated surveys for Lyman break galaxies in recent years, but several ground-based imaging programs have made significant contributions, particularly surveying wider areas at (relatively) shallower depths to constrain the bright end of the luminosity function. The *Subaru* telescope and its SuPrime Cam imager have been particularly important in this respect, although deep infrared imaging from *UKIRT* and the *VLT* have also been used. Notable examples (not an exhaustive list) include Ouchi et al. (2004), Yoshida et al. (2006), Iwata et al. (2007) and McLure et al. (2009) at $z = 4$ to 6, and Ouchi et al. (2009), Castellano et al. (2010a,b), Bowler et al. (2012), and Tilvi et al. (2013) at $z \approx 7$.

The installation of the Advanced Camera for Surveys (ACS) enabled substantially more efficient optical *HST* imaging covering fields much wider than the original HDF. ACS also offered significant gains in sensitivity at the reddest wavelengths, making Lyman break selection practical out to $z \approx 6$. Two major ACS surveys led to new derivations of the cosmic SFRD. The Great Observatories Origins Deep Survey (GOODS; Giavalisco et al. 2004b) observed two independent fields with combined area $> 60\times$ larger than the HDF through four filters. In particular this provided a sample of several thousand Lyman break candidates at $z \approx 4$ and of order a thousand at $z \approx 5$, reaching significantly fainter than L^* , permitting robust characterization of the luminosity density. LBG selection at $z \approx 6$ was less secure from GOODS ACS data alone, as it was based on a single color ($i - z$) and could only sample relatively bright galaxies. The Hubble Ultradeep Field (HUDF; Beckwith et al. 2006) observed a single ACS pointing (approx. 11 arcmin^2), located within the GOODS-S region, with very long exposure times, reaching fainter than the original HDF and with better sensitivity at higher redshifts. Both GOODS and the HUDF have been repeatedly revisited with new observations from *HST* over the years, adding deeper optical imaging as well as near-infrared data, first from NICMOS (Thompson et al. 2006; Conselice et al. 2011) and later with WFC3 in the HUDF09 and HUDF12 programs (Bouwens et al. 2011b; Ellis et al. 2013), and the Cosmic Assembly Near-infrared Deep Extragalactic Legacy Survey (CANDELS) of several premier deep survey fields, including GOODS (Grogin et al. 2011; Koekemoer et al. 2011). These infrared observations make Lyman break selection at $z \approx 6$ far more robust, and extend the method out to $z \approx 8$, with a handful of unconfirmed candidates identified out to $z \approx 12$.

Early analyses of the GOODS data (Giavalisco et al. 2004a) found evidence for relatively mild evolution of the UV luminosity density from $2 < z < 5$, but clear evidence that there were fewer high-luminosity galaxies at $z \approx 6$ (Stanway et al. 2003; Dickinson et al. 2004). Subsequent studies have repeatedly mined the combined GOODS+HUDF observations, using deeper data and more rigorous analyses. At least 20 papers about high redshift luminosity functions using WFC3 data in the HUDF and GOODS/CANDELS have been published since 2010, augmenting at least a dozen others pre-WFC3, and we cannot attempt to review them all here. They have convincingly demonstrated that the UVLF evolves significantly at $z > 4$. The current consensus is that this is primarily luminosity evolution, at least at $4 < z < 7$, with L^* brightening over time (e.g., Bouwens et al. 2007; Grazian et al. 2011; Bouwens et al. 2012b). As a result, the number density of bright LBGs increases rapidly with time, more quickly than does the integrated luminosity density. Analyses using the CANDELS and HUDF09+12 near-infrared imaging point to continued evolution out to $z = 8$ and perhaps beyond (Oesch et al. 2012; Yan et al. 2012; Lorenzoni et al. 2013; Schenker et al. 2013), although it would be prudent to recall that only a handful of galaxies

at $z \approx 7$ have reasonably secure spectroscopic confirmation, and none at $z > 7.5$. There is broad agreement that UV spectral slopes for LBGs are bluer at $z > 4$ than at lower redshifts (Bouwens et al. 2012a; Finkelstein et al. 2012a; Dunlop et al. 2013), which in turn has implications for their dust extinction and total star formation rate density. Most of these studies have examined the faint end slope of the luminosity function, measuring very steep values, in some cases approaching or exceeding the divergent value $\alpha = -2$ (Bouwens et al. 2012b; McLure et al. 2013). Several studies have even extended SFRD analyses to $9 < z < 12$, using data from the HUDF (Bouwens et al. 2011a; Ellis et al. 2013) or from lensing cluster studies (Coe et al. 2013). These measurements, while still in flux as better data accumulate, have considerable significance for the earliest phases of galaxy evolution and for the reionization of the IGM (e.g., Robertson et al. 2013), but relatively little impact on the global star formation budget of the universe. According to current estimates, only $\sim 1\%$ of the cosmic stellar mass density present today was formed at $z > 6$.

4.2 Infrared surveys

IRAS enabled the first measurements of the local far-infrared luminosity function (IRLF; Lawrence et al. 1986; Soifer et al. 1987; Saunders et al. 1990; Sanders et al. 2003). These were typically measured either at $60 \mu\text{m}$ observed wavelength, or using far-infrared luminosities integrated over a broader wavelength range, generally extrapolated from the measured *IRAS* fluxes using fitting formulae. While various different representations of far-infrared luminosity have been adopted, here we will consider L_{IR} as the luminosity integrated over the range 8 to $1000 \mu\text{m}$, a range which encompasses most of the bolometric luminosity of dust emission from nearly all sources of interest. The longest wavelength *IRAS* band was at $100 \mu\text{m}$, but *AKARI* extended all-sky far-infrared measurements out to $160 \mu\text{m}$, providing more reliable measurements of the bolometric luminosity and reduced bias against galaxies with cold dust temperatures. Goto et al. (2011a) and (2011b) reanalyzed the local IRLF incorporating *AKARI* data, and while there are differences in detail, the results are largely consistent with previous *IRAS* measurements in the luminosity range of overlap. Luminosity functions have also been measured for *IRAS* samples selected at 12 and 25 microns (Rush et al. 1993; Shupe et al. 1998). Luminosity functions at longer infrared wavelengths were measured for (rather small) local samples with *ISO* ($90 \mu\text{m}$, Serjeant et al. 2004; $170 \mu\text{m}$; Takeuchi et al. 2006), *Herschel* ($250\text{--}500 \mu\text{m}$, Vaccari et al. 2010; Dye et al. 2010), and with ground-based (sub)-mm observations, generally for *IRAS*-selected samples (1.2mm , Franceschini et al. 1998; $850 \mu\text{m}$, Dunne et al. 2000). New, large-area measurements using the largest *Herschel* surveys (e.g., H-ATLAS, covering 550deg^2 , with observations from 100 to $500 \mu\text{m}$) have not yet appeared in the literature.

Nearly all studies find that the bright end of the IRLF cuts off less sharply than the exponential used in the Schechter function. This has typically been modeled either as a double power law (e.g., Lawrence et al. 1986; Sanders et al. 2003) or as a combined log-normal and power law (e.g., Saunders et al. 1990). Locally, the bright end of the IRLF is dominated by galaxies with warmer dust temperatures, which tend to be starburst galaxies and dusty AGN (Saunders et al. 1990). Several studies have measured quite a steep faint-end slope α ($dN/dL \propto L^\alpha$), e.g., $\alpha = -1.6$ (Sanders et al. 2003), or even steeper ($\alpha = -1.8$, Goto et al. 2011a; $\alpha = -1.99$, Goto et al. 2011b), although a few have found flatter distributions, $\alpha = -1.2$ to -1.0 (e.g., Saunders et al. 1990; Takeuchi et al. 2003; Vaccari et al. 2010). In practice, the faint end has not been well-sampled locally except in a few of the *IRAS* surveys. Future analysis of the widest *Herschel* surveys may help resolve this.

It is worth noting that in local, relatively quiescent spiral galaxies like the Milky Way, more than half of the far-infrared luminosity is believed to arise not from dust in active star-forming regions, but from dust in the general interstellar medium, heated by ambient starlight from intermediate- and older-age stellar populations (Lonsdale Persson & Helou 1987; Sodroski et al. 1997). The luminosity of the Milky Way is quite typical ($L_{\text{IR}} \approx 10^{10} L_{\odot}$ (Sodroski et al. 1997), compared to the knee of the local IRLF at $L_{\text{IR}}^* = 10^{10.5} L_{\odot}$ (Sanders et al. 2003). This implies that a significant fraction of the local IR luminosity density is not directly the result of young star formation, and hence not necessarily a good measure of the global star formation rate today. At higher redshift, when the specific star formation rate of typical galaxies was much larger, and the net dust extinction to star-forming regions was on average larger (see § 5.1), we may expect the IRLF and its integral to more reliably trace the total SFRD. However, Salim et al. (2009) have suggested that even at higher redshift ($z \approx 0.7$), intermediate-age stars may significantly contribute to mid-infrared dust emission observed by *Spitzer* at $24 \mu\text{m}$.

The deepest surveys with *ISO* at $15 \mu\text{m}$ detected a few hundred galaxies, mainly at $z \leq 1$, in the Hubble Deep Field and a few other deep survey regions where spectroscopic and photometric redshifts were available (Rowan-Robinson et al. 1997; Flores et al. 1999; Aussel et al. 1999). Analyses of these generally agreed that the emission from dusty star formation increased steeply with redshift, although statistics were generally too poor to construct redshift-dependent luminosity functions. Chary & Elbaz (2001) used measurements from *ISO* and SCUBA, as well as constraints from the far-infrared background as measured by the *COBE* satellite, to constrain a model for the evolution of the cosmic star formation history. Their model exhibited a sharp decline in the SFRD by a factor of 10 or more from $z \approx 0.8$ to the present, with a plateau of nearly constant star formation from $0.8 < z < 2$. At higher redshifts the SFRD was more poorly constrained. Submillimeter sources placed a rough lower bound, while the cosmic infrared background (CIRB) set an upper limit. Acceptable solutions ranged from flat evolution to an increase by a factor of ~ 10 from $z = 4.5$ to 2.

The *Spitzer Space Telescope* greatly enhanced the sensitivity and mapping efficiency for deep infrared observations, particularly at $24 \mu\text{m}$, where the beam size (FWHM $\approx 5''.7$) was small enough to enable relatively straightforward association with optical counterparts. Also, *Spitzer* observed in an era when very large spectroscopic redshift surveys were available or underway, and when photometric redshift techniques were well established. Le Floc'h et al. (2005) produced an early, seminal analysis of $24 \mu\text{m}$ sources at $0.3 < z < 1.2$ in the Extended Chandra Deep Field South. Integrating over derived infrared luminosity functions, they inferred an evolution of the infrared luminosity density proportional to $(1+z)^{3.9 \pm 0.4}$, significantly steeper than the evolving UV luminosity density, $\rho_{\text{FUV}} \propto (1+z)^{2.5}$, Schiminovich et al. (2005). With strong luminosity evolution, the fraction of the IR luminosity density produced by Luminous and Ultraluminous Infrared Galaxies evolved even more steeply: Le Floc'h et al. found that galaxies with $L_{\text{IR}} > 10^{11} L_{\odot}$ produced $70\% \pm 15\%$ of the IR luminosity density at $z \approx 1$, compared to approximately 5 to 15% today, depending on the adopted local luminosity function. Several analyses of luminosity functions, mainly at $z < 1$, using shallower *Spitzer* data covering significantly wider areas have also been published, including Babbedge et al. (2006) and Rujopakarn et al. (2010) at $24 \mu\text{m}$, and Patel et al. (2013) at $70 \mu\text{m}$ and $160 \mu\text{m}$. The work by Rujopakarn et al. (2010) is particularly notable for its combination of (relatively) wide area (9 deg^2), extensive spectroscopic redshifts (4047 galaxies with $z \leq 0.65$), and $24 \mu\text{m}$ sensitivity (0.27 mJy , sufficient to reach $\sim L^*$ out to $z = 0.65$), making it arguably the best bridge study to date

between local (*IRAS* and *AKARI*) measurements and deep field studies at $z \geq 1$.

Several studies extended *Spitzer* 24 μm -based luminosity function measurements to higher redshifts, $z \approx 2$ to 2.5 (Pérez-González et al. 2005; Caputi et al. 2007; Rodighiero et al. 2010), primarily using deeper 24 μm data and fainter spectroscopic and photometric redshifts available in the two GOODS fields.⁶ Broadly speaking, these studies all found flatter IR luminosity density evolution at higher redshifts, with modestly lower or higher $\rho(L_{\text{IR}})$ at $z = 2$ than at $z = 1$, depending on the analysis. All three studies found that the characteristic IR luminosity L_{IR}^* brightened further at $z > 1$, such that ULIRGs emitted close to 50% of the total energy density at $z \approx 2$ (Caputi et al. 2007; Rodighiero et al. 2010), or even the majority (Pérez-González et al. 2005).

In detail, infrared luminosity functions estimated at high redshift have differed at both the faint and bright ends, depending on the data, methodology, and assumptions that are used. At the faint end, the available data rarely constrain the slope of the luminosity function at high redshift – indeed, as already noted, there are significant differences in the faint end slopes that have been measured at $z \approx 0$. Data with a limiting 24 μm flux density of 80 μJy , as for most of the earlier *Spitzer* studies described above, only reach a factor of a few fainter than typical estimates of L_{IR}^* at $z \approx 1$, and barely reach L_{IR}^* at $z \approx 2$. Thus, most analyses are forced to assume a faint-end slope based on measurements at lower redshifts, and are thus subject to large (typically $> 100\%$) and uncertain extrapolations to total IR luminosity densities.

Moreover, there are significant differences in the (large) extrapolations from observed mid-infrared rest-frame measurements (e.g., 8 μm rest-frame at $z = 2$) to the bolometric IR luminosity and SFR, depending on the SED templates that are adopted, and indeed we expect such variations among real galaxies. Pérez-González et al. (2005) found many more galaxies with $L_{\text{IR}} > 10^{12} L_{\odot}$ at $z \approx 2$ than did several other studies, in part due to different assumptions about these bolometric corrections. Also, different procedures for accounting for AGN emission (which can be particularly strong in the mid-infrared), as well as heavy reliance on photometric redshifts, may all contribute to systematic issues in the IRLF, particularly at the bright end.

As we noted earlier (§3.1.2), several studies (Papovich et al. 2007; Daddi et al. 2007) stacked data at longer far-infrared wavelengths (e.g., 70 μm) or in radio and submm data and found that standard SED templates like those of Chary & Elbaz (2001) tend to overestimate typical bolometric corrections from observed 24 μm data for galaxies at $z \approx 2$. This suggested that true far-infrared measurements were needed to reliably determine luminosities and SFRs at high redshift. Huynh et al. (2007) made early measurements of the IRLF at $z < 1$ using the deepest available *Spitzer* 70 μm data in GOODS-N. The sample of detected sources was very small, but was found to be generally consistent with the earlier 24 μm work by Le Floch et al. (2005).

Magnelli et al. (2009, 2011) extended this using comparably deep 70 μm data over a much wider area from the Far-Infrared Deep Extragalactic Legacy (FIDEL) survey. In addition to counting detected sources (mostly at $z < 1.3$, given the depth of the 70 μm data), Magnelli et al. stacked 70 μm data in bins of 24 μm flux and redshift, in order to empirically measure the average conversion between observed mid-IR and far-IR luminosities. Magnelli et al. also used significantly deeper 24 μm catalogs than previous studies, extending down to 30 μJy in the GOODS fields. At $z < 1.3$, Magnelli et al. (2009) found that the average

⁶Pérez-González et al. (2005) used shallower 24 μm data, while Caputi et al. (2007) and Rodighiero et al. (2010) employed deeper data from the GOODS team. Rodighiero et al. also incorporated relatively shallow *Spitzer* 24 μm data covering 0.85 deg² in one of the VVDS redshift survey fields.

far-IR over mid-IR flux ratios closely matched predictions from the Chary & Elbaz (2001) template library, and correspondingly they measured luminosity functions that were similar to previous measurements, but extending to fainter luminosities, significantly below the bend in the IRLF at $z \approx 1$, and with better statistics. At $z > 1.3$, however, Magnelli et al. (2011) confirmed previous suggestions that the average $70 \mu\text{m}$ to $24 \mu\text{m}$ flux ratios deviated systematically from the predictions of standard local SED templates. They extrapolated from the averaged $70 \mu\text{m}$ fluxes to the bolometric IRLF, finding only a mild increase in L^* and the luminosity contribution of ULIRGs from $z \approx 1$ to 2. At lower redshifts, the faint end slope was found to be consistent with $\alpha = -1.6$ as measured for local *IRAS* galaxies by Sanders et al. (2003). By $z = 2$, the data reach only slightly fainter than the IRLF knee, and the slope is not constrained. However, extrapolating with a fixed slope $\alpha = -1.6$, Magnelli et al. found that the faint IRLF at $z = 2$ would be quite similar to that predicted by Reddy et al. (2008) based on UV-selected galaxies and the dust absorption predicted from their UV spectral slopes.

The *Herschel Space Observatory* significantly improved sensitivity and reduced the beam size for far-infrared ($70\text{--}500 \mu\text{m}$) observations, and several large programs were dedicated to surveys of the most important multiwavelength deep fields. Even the deepest *Herschel* surveys do not detect as many sources per square arcminute as are found in the deepest *Spitzer* $24 \mu\text{m}$ observations, but direct access to far-infrared wavelengths is invaluable for reliably estimating bolometric luminosities and star formation rates at high redshift. Several analyses presented preliminary luminosity functions out to $z = 2$ to 3 using data sets obtained early in the *Herschel* mission (Eales et al. 2010; Gruppioni et al. 2010; Lapi et al. 2011).

More extensive analyses of larger *Herschel* data sets have recently appeared in the literature. Gruppioni et al. (2013) use sources selected in *Herschel* PACS observations at 70 , 100 and $160 \mu\text{m}$ in the two GOODS fields, as well as shallower but wider observations of the Extended Chandra Deep Field South and COSMOS. They employ photometry from both the PACS and SPIRE ($250\text{--}500 \mu\text{m}$) instruments to derive infrared luminosities based on spectroscopic and photometric redshifts, using customized infrared spectral energy distribution templates. They derive luminosity functions out to $z < 4.2$, although at the highest redshifts ($3 < z < 4.2$) the data are only sensitive to the rarest hyperluminous sources. Magnelli et al. (2013) restrict their analysis to the deepest 70 to $160 \mu\text{m}$ data available in the GOODS fields, and extract far-infrared fluxes to still fainter limits at positions of $24 \mu\text{m}$ -detected sources, limiting their analysis to $z < 2.3$. Note that, as is so often the case, the fields analyzed and the data used in these studies overlap considerably; even if the methods of analysis are different, they cannot be considered to be fully independent. That said, in their range of overlap, the two analyses are generally consistent, and find somewhat stronger luminosity evolution at $z > 1$ than in the *Spitzer* analysis of Magnelli et al. (2011), and hence a larger contribution of ULIRGs to the total IR luminosity density at $z \approx 2$ (but not as large as in some earlier *Spitzer* studies, e.g., by Pérez-González et al. 2005). Magnelli et al. conclude that this difference (compared to their own very similar *Spitzer* analysis) is mainly due to better determination of the total IR luminosities of galaxies using the improved *Herschel* far-infrared measurements. Gruppioni et al. (2013) find that the characteristic luminosity L_{IR}^* continued to brighten at $z > 2$, albeit at a slower rate. Neither survey reliably measures the faint end slope of the IRLF at high redshift, and both fix it to values derived locally, adopting quite different values (Magnelli's $\alpha = -1.6$ versus Gruppioni's -1.2). In fact, given these different slopes, it is striking and perhaps surprising that these two analyses derive quite similar values for the total IR luminosity

density at redshifts $0 < z < 2$. Broadly speaking, both studies find evolution by a factor of approximately 6 between $z = 1.1$ and the present, and comparatively flat evolution at higher redshift, to $\langle z \rangle = 2.05$ in Magnelli et al. , and $\langle z \rangle = 2.75$ in Gruppioni et al. , albeit with an increasing range of values allowed within the measurement uncertainties.

Figure 7 shows recent determinations of the infrared and ultraviolet luminosity functions at $0 < z < 4$. The UVLFs in the figure show the observed luminosities uncorrected for extinction, and are presented in units of solar luminosities for more direct comparison to the IRLFs. This figure illustrates several points. (1) The IRLFs cut off less steeply at high luminosities than do the UV LFs. (2) The IRLFs extend to much higher luminosities than the UVLFs at the same redshifts, as the most actively star-forming galaxies tend to be strongly obscured by dust. (3) There is strong luminosity evolution, particularly for the IRLFs, but also in the UV, with more modest density evolution. (4) The UVLFs shown here, from Cucciati et al. (2012), exhibit a trend toward steeper faint-end slopes at higher redshifts, especially for $z > 2$. This last point is not universally agreed upon, but most studies do measure quite steep UV luminosity functions at $z > 2$, and a trend toward bluer UV colors at faint luminosities. Together, these point to low extinction for galaxies with lower SFRs, and a significant contribution from low-luminosity galaxies to the global SFR density at high redshift.

Before *Spitzer* and *Herschel*, ground-based submillimeter bolometer arrays, especially SCUBA at JCMT, provided an essential glimpse at dusty star formation at very high redshifts. As is frequently noted, the negative K correction at submillimeter wavelengths approximately cancels luminosity distance dimming at $z > 1$. The flux limits of most submm surveys limit individual source detections to ultra- and hyper-luminous galaxies, so that only the tip of the infrared luminosity function is sampled. In practice, the greatest limitation for deriving luminosity functions or SFRD is identifying galaxy counterparts to submillimeter sources and measuring their redshifts, due mainly to the large beam-size of single-dish submillimeter observations, but also to the fact that the optical counterparts are often very faint and sometimes invisible. On the other hand, another consequence of the negative K correction is that substantial redshift uncertainties translate to only relatively small uncertainties in the bolometric luminosity. Hence Barger et al. (2000) were able to make plausible estimates of the SFRD from submm sources in broad redshift bins, using radio-identified counterparts and very rough radio-millimetric redshift estimates. Barger et al. (2012) have recently updated this using a complete SMG sample with accurate interferometric positions from the SMA, and with more extensive redshift information, in part thanks to recent advances in millimetric CO spectroscopy. Chapman et al. (2005) measured optical spectroscopic redshifts for a sample of radio-identified SMGs, and derived the first SMG luminosity functions at $\langle z \rangle = 0.9$ and $\langle z \rangle = 2.5$. These estimates were recently updated by Wardlow et al. (2011) using (mainly) photometric redshifts for another well-defined SMG sample. These analyses demonstrated a significant contribution of dusty SMGs to the cosmic SFRD at high redshift, mainly limited to $z \lesssim 4$, although recent discoveries of substantial numbers of SMGs out to $z = 6.3$ (e.g., Riechers et al. 2013) suggest that the dusty ultraluminous population may be important even in the first few Gyr of the cosmic star formation history.

Although direct far-infrared detection of individual sources at $z \gg 2$ is limited to the most extremely luminous objects (Fig. 1), the CIRB provides additional constraints on dusty star formation at the highest redshifts (Pei et al. 1999; Gispert et al. 2000). Far-infrared source counts and the CIRB were reviewed by Lagache et al. (2005), and recent results from *Herschel* reviewed by Lutz (2014) in the present volume, so we only briefly

discuss this here. Sources directly detected by *Herschel* in the deepest observations resolve about 75% of the CIRB at 100 and 160 μm (Berta et al. 2011; Magnelli et al. 2013), albeit with significant uncertainties at 100 μm . Stacking *Herschel* data at the position of sources detected by Spitzer at 24 μm detects a larger fraction still, and with modest extrapolation can account for the entire CIRB at these wavelengths. At 250 to 500 μm , where confusion is more severe in *Herschel* SPIRE data, the directly resolved fractions are smaller (from 15% to 5% at 250 to 500 μm), while stacking detects 73% to 55%; again, an extrapolation is consistent with resolving the entire background (B  thermin et al. 2012). Because the deepest *Herschel* observations were carried out in fields like GOODS and COSMOS with exceptional ancillary data, it is possible to stack in bins of photometric redshift, to constrain the redshift distribution of the CIRB emission. At higher redshifts, the peak of dust emission from galaxies shifts to longer far-IR and submillimeter wavelengths, and the fractional contribution of more distant galaxies increases with the wavelength of the bandpass analyzed. Combining data from Spitzer through *Herschel* to ground-based submillimeter observations, B  thermin et al. (2012) estimate that $4.7 \pm 2.0 \text{ nW m}^{-2} \text{ sr}^{-1}$, or $17_{-9}^{+11}\%$ of the integrated CIRB, is produced by galaxies at $z > 2$. While the fraction is small, this still allows for a significant amount of dusty star formation to take place at $z > 2$, beyond that which is seen in directly detected sources. We note that the 24 μm sources used for these stacking analyses are also subject to strong k -correction dimming at $z > 2$, and hence it is conceivable that a still larger fraction of the high-redshift CIRB is missed in this way.

4.3 Emission line surveys

Among the nebular emission lines that have been most frequently used to quantify star formation rates at high redshift, $\text{H}\alpha$ is arguably the most useful, as discussed earlier in Section 3.1.4. Lines from other elements, most commonly $[\text{OII}] 3727 \text{ \AA}$, have also been used to measure the cosmic star formation rate (e.g., Hogg et al. 1998), but their more complex dependence on metallicity and ISM conditions, as well as larger extinction, makes them problematic. Narrow band $\text{Ly}\alpha$ surveys are popular at high redshift, but $\text{Ly}\alpha$ is so strongly subject to resonant scattering and extinction that it must always be regarded as setting only a lower limit on the true star formation rate.

$\text{H}\alpha$ is accessible with optical observations only at $z < 0.5$, and near-infrared observations are needed to follow it out to higher redshifts ($z \lesssim 2.5$). Recent technological developments in infrared instrumentation have significantly increased the potential for such measurements. A new generation of wide-field imagers using mosaics of infrared arrays is now operating on 4m- and 8m-class telescopes (e.g., *UKIRT* WFCAM, *CFHT* WIRCAM, *NOAO* NEWFIRM, *VISTA* VIRCAM, *VLT* HAWK-I), significantly increasing the comoving volumes accessible for deep narrow-band imaging. Near-infrared multiobject spectrographs are now becoming mature and efficient (e.g., *Subaru* MOIRCS and FMOS, *Keck* MOSFIRE, *VLT* KMOS, *LBT* LUCI). Slitless grism spectroscopy with WFC3 on *HST* can measure faint $\text{H}\alpha$ lines out to $z < 1.5$ for all objects within its field of view. Each method has advantages and disadvantages. Narrow band imaging surveys are tuned to specific, narrow redshift ranges, and are thus strongly subject to density variations due to line-of-sight clustering effects. Flux calibration for objects whose redshifts place emission lines in the wings of the narrow bandpasses can also be problematic. Only statistical corrections can be made for the flux contribution from $[\text{NII}]$, or for stellar absorption. Multi-slit spectroscopy is subject to slit losses that complicate measurements of integrated line fluxes, and atmospheric absorption and emission significantly limit the accessible redshifts and can introduce complicated selec-

tion effects.⁷ *HST* WFC3 slitless spectroscopy avoids concerns about the atmosphere and slit losses, but deep observations covering adequately large solid angles are time-intensive. As of this writing, results on $H\alpha$ luminosity functions from the largest ongoing programs (WISPS, Atek et al. 2010 and 3D-HST, Brammer et al. 2012) have not yet appeared in the literature to supersede earlier *HST* NICMOS results (Yan et al. 1999; Hopkins et al. 2000; Shim et al. 2009). With all methods, reliable extinction corrections depend on measurement of the Balmer decrement (the ratio of $H\alpha$ to $H\beta$ line fluxes). This is sometimes available for spectroscopic samples, although in that case the sample selection is often limited by the weaker $H\beta$ line; it is rarely available for narrow-band surveys. Hence, statistical corrections are often adopted. AGN and LINERs can also contribute significantly to the samples of emission line galaxies, and can only be reliably taken into account using high quality spectroscopic data to measure line excitation diagnostics. Most careful studies of the local galaxy population using spectroscopy from SDSS or GAMA (see below) have done this, but it is rarely possible at higher redshifts, and most studies have resorted to statistical corrections or none at all.

There is a long literature of luminosity function and SFRD measurements from $H\alpha$, [OII] and [OIII], and we will only note selected works here. Gunawardhana et al. (2013) include a thorough and up-to-date compilation of these measurements at low and high redshifts.

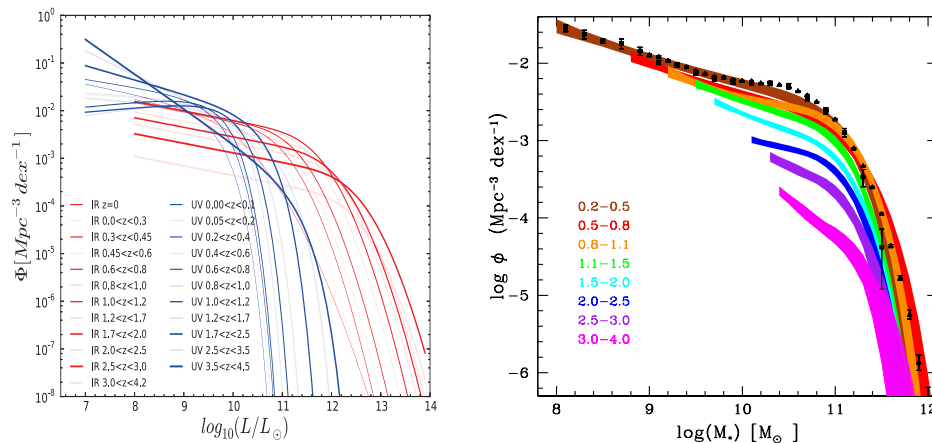


Figure 7: *Left panel:* Redshift evolution of the far-ultraviolet and far-infrared luminosity functions at $0 < z < 4$. The blue curves are Schechter function fits to the FUV luminosity data from Cucciati et al. (2012), with no correction for dust attenuation. The red curves are fits the far-infrared luminosity function data from Gruppioni et al. (2013), use the functional form of Saunders et al. (1990), which better represents the distribution of sources at high infrared luminosities. (From Burgarella et al. 2013.) *Right panel:* Galaxy stellar mass function from low to high redshift for a large, deep ($K_s < 24$) sample of 220,000 galaxies selected using the new UltraVISTA DR1 data release. Each color corresponds to different redshift bins of variable step size. Fits are shown in the mass range covered by the dataset. The filled areas correspond to the 68% confidence level regions, after accounting for Poissonian errors, the cosmic variance and the uncertainties created during the template fitting procedure. The open triangles and squares correspond to the local estimates by Moustakas et al. (2013) and Baldry et al. (2012), respectively. (From Ilbert et al. 2013.)

Gallego et al. (1995) presented an important early study of the local $H\alpha$ luminosity func-

⁷The new *VLT* KMOS spectrograph uses multiple deployable integral field units, eliminating slit loss concerns, and may prove to be a valuable tool for $H\alpha$ surveys.

tion, using objective prism photographic data. Subsequently, the SDSS provided a vast number of spectroscopic redshifts and line flux measurements, although the small aperture size of spectroscopic fibers requires careful and inevitably uncertain corrections to the total emission line flux for each galaxy. SDSS spectroscopy covers both $H\alpha$ and $H\beta$, and hence can provide a measurement of extinction via the Balmer decrement, although care is needed to account for stellar absorption, flux limits and selection effects, etc. Brinchmann et al. (2004) made a widely-cited study of local star formation from SDSS optical spectroscopy and photometry. This used a full analysis of the emission and absorption line spectroscopy, and was thus not strictly based on $H\alpha$ alone, although certainly the Balmer lines carry significant weight in the SFR determinations. As noted earlier, Salim et al. (2007) carried out an independent SDSS analysis based mainly on photometry including *GALEX* UV measurements, but with extensive cross-comparison to the $H\alpha$ data. By using photometry, the Salim analysis bypasses uncertainties inherent in the spectroscopic $H\alpha$ aperture corrections. The local star formation rate densities (normalized to $z = 0.1$) from the Brinchmann and Salim studies agree extremely well. Most recently, Gunawardhana et al. (2013) combine data from the SDSS with significantly deeper (but also much smaller) fiber spectroscopy from the GAMA survey, in order to probe fainter down the luminosity function and extend the analysis to higher redshifts, $z < 0.35$.

Optical spectroscopic surveys have measured $H\alpha$ star formation rate densities typically out to $z < 0.4$ (e.g., Tresse & Maddox 1998; Sullivan et al. 2000; Westra et al. 2010; Gunawardhana et al. 2013). Until recently, near-infrared spectroscopy was measured only for small samples, object by object, typically at $0.5 < z < 1.1$ (Glazebrook et al. 1999; Tresse et al. 2002; Doherty et al. 2006). In general, no direct measurements of extinction are available, and could only be assumed, along with corrections for stellar absorption. Larger-scale and deeper spectroscopic surveys from a new generation of multi-object infrared spectrographs on 8-10m telescopes should be forthcoming.

Several studies have exploited slitless grism spectroscopy of $H\alpha$ at $0.7 < z < 1.9$ from the *HST* NICMOS instrument (Yan et al. 1999; Hopkins et al. 2000; Shim et al. 2009), again for small but relatively unbiased samples, observed with relatively uniform sensitivity over a broad redshift range, and without concerns for flux losses due to a finite spectrograph slit size. Once again, direct measurements of extinction are generally unavailable, and the low-resolution slitless spectroscopy inextricably blends $H\alpha$ with [NII], again requiring purely statistical corrections. New, more sensitive grism surveys with *HST* WFC3, covering larger solid angles, are underway.

The largest number of high redshift measurements has come from narrow band imaging surveys, using wide-field CCD cameras out to $z \approx 0.4$, and with infrared arrays at higher redshifts. These are generally carried out using filters that fit into spectral windows relatively unaffected by atmospheric absorption or emission, corresponding to specific redshifts ($z = 0.24, 0.40, 0.84, 1.47$, and 2.23 are all common). Using a new generation of wide-field imagers, the current state-of-the-art $H\alpha$ surveys are those of Ly et al. (2007, 2011), Hayes et al. (2010), and Sobral et al. (2013). The latter survey (HiZELS) combines data from *Subaru* Suprime-Cam ($z = 0.40$) and *UKIRT* WFCAM ($z = 0.84, 1.47$ and 2.23), covering approximately 2 deg^2 in two survey fields, with deeper but narrower (0.03 deg^2) observations at $z = 2.23$ from the *VLT* and its HAWK-I imager. Between 500 and 1750 $H\alpha$ emitters are detected in each redshift window, providing good statistics. These authors measure a steady increase in the characteristic luminosity $L^*(H\alpha)$ with redshift, with a faint-end slope $\alpha \approx 1.6$ that is constant with redshift, and is also similar to that found in most of the UV continuum surveys.

4.4 Radio surveys

Centimeter wavelength radio continuum emission from star-forming galaxies arises from a combination of flat-spectrum free-free emission, which is prominent at high frequencies, and steep spectrum synchrotron emission, which dominates at lower frequencies. Although the free-free emission should in principle be quite a direct tracer of star-formation rates, so far it has been impractical to observe this at high redshift, although the improved high-frequency sensitivity of the Jansky VLA should open this capability in the future. The lower-frequency emission arises mainly as a consequence of supernovae, and hence is also related to the star formation rate. In practice, its calibration as an SFR measurement is primarily empirical, e.g., based on the tight correlation observed between radio and far-infrared emission for *IRAS*-selected galaxies in the local universe (e.g., Yun et al. 2001). This correlation, together with insensitivity to dust extinction, make radio emission an attractive wavelength for studying star formation.

Problematically, AGN can also produce powerful radio emission. Locally, radio sources with $L_\nu(1.4 \text{ GHz}) > 10^{23} \text{ W Hz}^{-1}$ are predominantly AGN. This radio luminosity would correspond to a star formation rate $> 94 M_\odot \text{ yr}^{-1}$, using the conversion factor from Murphy et al. (2011) scaled to a Salpeter IMF. Such galaxies are extremely rare locally, and hence it is common to simply exclude very powerful radio sources as likely AGN. However, at $z > 1$, galaxies with these star formation rates (corresponding to ULIRGs in terms of their infrared luminosities) are common, even “normal” (see §3.1.2), and thus it is problematic to disregard them simply on the basis of their radio emission. Other considerations are needed to distinguish AGN from star forming radio sources, such as radio spectral index, radio morphology, or radio/infrared flux ratios, but these are all more difficult to measure, especially for very faint sources.

The local radio luminosity function has been used to estimate the present-day star formation rate density in many studies, of which recent examples include Machalski & Godlowski (2000), Condon et al. (2002), Sadler et al. (2002), Serjeant et al. (2002), and Mauch & Sadler (2007). In these studies, care has been taken to separate AGN from star-forming galaxies on various criteria, often by comparison with *IRAS* infrared measurements, excluding objects with a radio excess relative to their infrared luminosities.

At $z > 1$, even the deepest VLA surveys have only been able to detect galaxies with star formation rates $\gtrsim 100 M_\odot \text{ yr}^{-1}$ (Fig. 1), and $\gtrsim 1000 M_\odot \text{ yr}^{-1}$ at $z > 3$, although the Jansky VLA is now pushing to fainter sensitivities. Haarsma et al. (2000) were among the first to combine very deep VLA observations with spectroscopic and photometric redshift information to derive radio luminosity functions and the cosmic star formation rate density at high redshift, primarily at $0.3 < z < 0.8$, although they also considered one very broad bin from $1 < z < 4.4$. This work, based on individually detected radio sources, was updated in later studies that took advantage of more extensive multiwavelength data to distinguish AGN from star-forming galaxies. Seymour et al. (2008) identified AGN based on radio spectral indices, radio morphology, and radio to near- and mid-IR flux ratios. Smolčić et al. (2009) used optical SED criteria to identify star-forming galaxies detected in VLA 1.4 GHz data for COSMOS, at more modest redshifts, $z < 1.3$. Seymour et al. assumed pure luminosity evolution for the luminosity function, consistent with the measurements by Smolčić et al. (and earlier by Haarsma et al.). All of these studies found broad agreement between the radio SFRD evolution and that from optical and infrared surveys, with a steep decline from $z = 1$ to 0; Seymour et al. measured a peak SFRD at $z \approx 1.5$, albeit with large uncertainties.

Other studies have used radio stacking to probe to fainter luminosities, below the detection limits for individual sources – particularly, stacking for near-IR samples that approximate stellar mass selection. Here, the assumption is that, as in the local universe, radio sources at fainter luminosities will primarily trace star formation, with relatively little AGN contribution. Dunne et al. (2009) stacked VLA 1.4 GHz and GMRT 610 MHz data for K -band selected sources, in bins of redshift and K -band luminosity, finding a linear (but redshift-dependent) relation between radio and near-IR luminosity. Using a measurement of the evolving K -band luminosity function from the same data set, they then use this radio/near-IR ratio to extrapolate the observations to the total radio luminosity density and SFRD. Karim et al. (2011) have carried out the most extensive study of this sort to date, using a large 1.4 GHz survey of COSMOS and a *Spitzer* $3.6\ \mu\text{m}$ -selected sample. Stacking in bins of stellar mass and photometric redshift and converting the mean radio fluxes to star formation rates, they extensively analyzed the SFR– M_* correlation, and used this and the evolving stellar mass function (from Ilbert et al. 2010) compute the integrated SFRD. Dunne et al. measured a steady increase in the SFRD from $z \approx 0$ to a peak at $z \approx 1.5$, declining at higher redshift to $z \approx 4$. Instead, Karim et al. found a monotonic decline in the SFRD from $z = 3$ to the present day.

4.5 Stellar mass density surveys

As the technology of near-infrared detectors advanced, so did surveys that used NIR photometry to more nearly sample galaxies by stellar mass at both low and high redshifts (e.g., Gavazzi et al. 1996; Cowie et al. 1996). However, it was not until the turn of the Millennium that authors started routinely to use stellar population synthesis models to convert photometry and redshift information to stellar masses for large samples of galaxies, especially at high redshift.

Before the era of large, modern redshift surveys like the SDSS and the 2dFGRS, several authors made estimates of the local baryonic and stellar mass densities (Persic & Salucci 1992; Fukugita et al. 1998; Salucci & Persic 1999). This effort accelerated, however, as the new spectroscopic surveys mapped the local universe. Cole et al. (2001) used 2dFGRS redshifts and near-infrared photometry from 2MASS to measure the local K -band luminosity function more accurately than had previously been possible. Then, using stellar population modeling, they inferred stellar masses from the galaxy colors and luminosities, and derived the local galaxy stellar mass function (GSMF) and the local comoving stellar mass density. Bell et al. (2003) did the same using SDSS and 2MASS. Many studies have subsequently derived the GSMF from incrementally improving SDSS data releases, using additional ancillary data, and a variety of methods for stellar population modeling, sometimes deriving mass-to-light ratios from photometry, and sometimes from the SDSS spectra themselves (Panter et al. 2007; Baldry et al. 2008; Li & White 2009). Moustakas et al. (2013) incorporated photometry from the ultraviolet (*GALEX*) to the mid-infrared (*WISE*) in their analysis of the SDSS GSMF. Baldry et al. (2012) analyzed a sample from GAMA, a wide-area spectroscopic survey extending significantly fainter than the SDSS, modeling M/L from optical SDSS photometry. As the samples have grown larger, more elaborate functional forms have been fit to the GSMF, including double and even triple Schechter functions, and there is some evidence that the GSMF slope at low masses ($< 10^9 M_\odot$) may be steeper than was previously believed (e.g., $\alpha = -1.47$, Baldry et al. 2012). Other authors have modeled stellar populations for ensembles of galaxies rather than deriving individual galaxy stellar masses, e.g., by fitting the integrated local luminosity densities for the entire

local volume, from UV to near-IR wavelengths (Baldry & Glazebrook 2003), or by modeling coadded SDSS spectra in bins of luminosity, velocity dispersion, and 4000 Å break strength (Gallazzi et al. 2008).

At higher redshifts, Brinchmann & Ellis (2000) derived stellar masses for galaxies at $z < 1$ in fields with both *HST* and NIR imaging. They found relatively little evolution in the integrated mass density at $0.4 < z < 0.9$, more or less as expected, given the declining cosmic SFRD at those redshifts, but a marked evolution in the mass breakdown by morphological type. Cohen (2002) similarly found no significant evolution in the stellar mass density at $0.25 < z < 1.05$. Because the cosmic SFRD declines steeply with time at $z < 1$, relatively little new stellar mass accumulates in the late stages of cosmic history. Moustakas et al. (2013) have recently broken new ground with a low-resolution prism spectroscopic survey measuring $\sim 40,000$ redshifts for galaxies at $0.2 < z < 1$ in five fields with *Spitzer* IRAC photometry covering 5.5 deg^2 . Even with such outstanding data, the evolution in the overall SMF at $0 < z < 1$ is nearly imperceptible, but the migration of galaxies from the star-forming to the quiescent population is confirmed with exquisite detail.

Sawicki & Yee (1998), Papovich et al. (2001), and Shapley et al. (2001) pioneered the use of stellar population models to derive stellar masses for Lyman break galaxies at $z \approx 2\text{--}3$. In turn, Dickinson et al. (2003), Fontana et al. (2003), and Rudnick et al. (2003) used the deepest near-IR imaging then available for the two Hubble Deep Fields, from *HST* NICMOS (HDF-North) and *VLT* ISAAC (HDF-South), together with extensive photometric and spectroscopic redshifts, to derive the comoving stellar mass density in several redshift bins out to $z \approx 3$. Strong evolution was found over that longer redshift baseline, with the stellar mass density at $z \approx 3$ measured to be in the range 5 to 15% of its present-day value, although a somewhat broader range of values would be permitted if systematic assumptions about the galaxy star formation histories or stellar metallicities were pushed well beyond the range of models used for the standard analysis. The stellar mass density reached half its present-day value somewhere between $z = 2$ and 1. Strong cosmic variance in these small fields was also evident: at $z > 2$, red galaxies with high mass-to-light ratios were nearly absent in the HDF-N, but were found in moderate abundance in the HDF-S, and the corresponding stellar mass densities differed substantially. This pointed to the importance of surveying larger fields and more sightlines, but obtaining infrared imaging to satisfactory depth over these larger regions of sky has proven to be very challenging, requiring another decade of effort.

The launch of *Spitzer* and the impressive performance of its IRAC camera for imaging at 3.6 to $8 \mu\text{m}$ made it possible to measure *rest-frame* near-infrared photometry for galaxies at high redshift, and major public survey imaging campaigns like GOODS, S-COSMOS and SWIRE produced widely-accessible and heavily-used imaging data sets spanning a wide range of area–depth parameter space, ideal for deriving stellar mass functions (SMFs) and densities at high redshift. Indeed, near-infrared imaging has struggled to catch up with IRAC in terms of comparable area–depth coverage, and despite the vast swaths of telescope time that have been invested in obtaining near-IR data on popular fields like GOODS and COSMOS, imaging at 1 to $2.5 \mu\text{m}$ still tends to fall short of *Spitzer*’s sensitivity at 3.6 and $4.5 \mu\text{m}$. At $z > 4.5$, the ground-based *K*-band samples rest-frame ultraviolet wavelengths, and IRAC offers the only viable way to measure optical rest-frame light in order to constrain stellar masses.

From 2006 onward, most (although not all) papers on stellar mass functions and densities at high redshift have made use of IRAC data – often in the same survey fields, analyzed over and over. Among many other papers, Fontana et al. (2006), Pérez-González et al.

(2008), Kajisawa et al. (2009), and Marchesini et al. (2009) analyzed stellar masses in the GOODS fields (sometimes in combination with other data sets) for galaxies out to $z \approx 4$, while Arnouts et al. (2007), Pozzetti et al. (2010), Ilbert et al. (2010), and Brammer et al. (2011) analyzed wider-area but shallower surveys (e.g., COSMOS, VVDS-SWIRE, NMBS), generally focusing on redshifts $z \leq 2$. Despite differences in the methodologies, the conclusions of these papers painted a remarkably consistent picture of the evolution of the SMF at $0 < z < 3$, with very little change in its shape, characteristic mass M^* , or its faint-end slope, but steady evolution in the characteristic density ϕ^* . There are indications that the faint end slope of the mass function may steepen at higher redshifts (e.g., Kajisawa et al. 2009; Santini et al. 2012). The integrated stellar mass densities measured in the different analyses generally agreed within factors of 2 at most redshifts, and a consistent picture of mass-buildup emerged.

Some of the most recent additions to this literature have taken advantage of deeper, wider near-infrared imaging from the largest-format cameras on 4m-class telescopes (Bielby et al. 2012; Ilbert et al. 2013; Muzzin et al. 2013) to map relatively wide survey areas like COSMOS or the CFHT Legacy Survey fields to depths previously reserved for small, deep surveys like GOODS. Together with ever growing spectroscopic surveys and increasingly excellent photometric redshifts, these have yielded the most statistically robust measurements of the stellar mass functions at $z < 2.5$, although several of these surveys repeat analysis in COSMOS, even using essentially the same imaging data sets, so these analyses are not always robust against cosmic variance.

Spitzer IRAC has been essential for deriving stellar masses at $z > 4$, and very deep observations are necessary to detect typical galaxies at those redshifts. For this reason, nearly all analyses of stellar mass densities at $z > 4$ have been carried out in GOODS and the HUDF,⁸ and nearly all have studied UV-selected Lyman break galaxies, for which there are abundant samples. Early analyses of small samples of galaxies at $z = 5$ and 6, including estimates of the integrated SMD, were presented by Yan et al. (2006), Eyles et al. (2007), Stark et al. (2007), Verma et al. (2007), and Yabe et al. (2009). These were followed by larger and more systematic analyses of LBG samples at $4 \geq z \geq 7$ (Stark et al. 2009; González et al. 2011; Lee et al. 2012), all of which used similar procedures, and found broadly similar results. In particular, the derived LBG stellar mass functions have somewhat shallower low-mass slopes than do the UV luminosity functions, because M/L_{UV} is found to decrease at fainter UV luminosities, at least at $z = 4$ and 5 where this could be measured with some robustness from galaxies with individual IRAC detections (e.g., Lee et al. 2012). Labbé et al. (2013) have recently extended this analysis to $z \approx 8$ using *HST* WFC3-selected samples in the HUDF and GOODS/CANDELS fields.

Exceptionally, a few studies have used IRAC selection to avoid the potential bias of UV selection against older or dustier galaxies. Caputi et al. (2011) analyzed an IRAC 4.5 *mu*m-selected sample in the UKIDSS UDS, computing stellar mass densities at $3 \leq z \leq 5$. The depth of their IRAC data limited direct detections to a stellar mass completeness limit $\gtrsim 10^{10.4} M_{\odot}$. Their extrapolated mass densities based on Schechter function fits fall somewhat below those from other LBG-based studies (e.g., González et al. 2011; Lee et al. 2012), but this is likely due to uncertainties in the large extrapolation required. Several other authors have analyzed partially or wholly IRAC-selected candidates for massive galaxies at $z \gtrsim 3.5$ (Wiklind et al. 2008; Mancini et al. 2009; Marchesini et al. 2010; Caputi et al. 2012), and

⁸In a departure from the GOODS-dominated norm, McLure et al. (2009) stacked relatively shallow IRAC data for LBGs at $z = 5$ and 6 in the UKIDSS Ultra Deep Survey (UDS) in order to measure average SEDs and mass-to-light ratios, and hence to estimate the stellar mass density.

in some cases have estimated comoving stellar mass densities, although generally without fitting stellar mass functions, and often without rigorous analysis of sample completeness.

Several studies have suggested that LBGs at $z \gtrsim 4$ have much stronger optical rest frame nebular line emission (particularly H α and [OIII]) than do similar UV-selected galaxies at lower redshifts (Chary et al. 2005; Raiter et al. 2010; Shim et al. 2011; Stark et al. 2013; Labbé et al. 2013). In most cases this has been inferred on the basis of *Spitzer* IRAC colors that would be unusual for pure stellar populations, but which can be explained if strong line emission boosts the IRAC fluxes. This line emission, if not taken into account, can significantly effect derived stellar population parameters, and generally leading to overestimated stellar masses. For LBG samples at $z = 4$ to 8, Stark et al. (2013) and Labbé et al. (2013) estimate that average stellar masses derived from models without nebular lines should be reduced by factors from 10 to 70%, with the effect increasing at higher redshifts. While the photometric evidence for this strong nebular emission is compelling, it will be vitally important for *JWST* spectroscopy to confirm and quantify its effects.

4.6 The state of the art, and what’s wrong with it

Local Measurements Measurements of the present-day star formation rate or stellar mass density require surveys covering a large fraction of the sky in order to be statistically meaningful. Salim et al. (2007) and Robotham & Driver (2011) have used most or all of the *GALEX* Medium Imaging Survey data, covering ~ 1000 deg² overlapping the SDSS and 2dFGRS spectroscopic surveys, and there is little prospect for improving the UV data in the near future. Only refinements in the analysis can be expected, e.g., incorporating improved photometric data at optical or near-IR wavelengths, or further joint analysis with spectroscopic stellar population measurements. We will see below (§5.1, Fig. 8) that there is significant disagreement in the literature about the net FUV extinction correction at $z \approx 0$. Wide-area spectroscopic emission line surveys (e.g., from SDSS or GAMA, Brinchmann et al. 2004, Gunawardhana et al. 2013) are limited by uncertain aperture corrections to line fluxes, while narrow-band imaging surveys have yet to cover enough galaxies over a wide enough area, and are usually limited by the absence of direct measurements of extinction from the Balmer decrement, the [NII] contribution to H α measurements, or the contribution of AGN emission. There is still room for progress in combined narrow-band plus spectroscopic data for large local samples. The local far-infrared luminosity function has not been drastically revised since the final *IRAS* analyses (Sanders et al. 2003; Takeuchi et al. 2003); additional *AKARI* data did not drastically change earlier results (Goto et al. 2011a,b; Sedgwick et al. 2011). The biggest remaining uncertainties pertain to the faint end slope, where measurements vary significantly from $\alpha = -1.2$ to -1.8 (or, somewhat implausibly, even -2.0 , e.g., Goto et al. 2011b). Analysis of the widest-area far-infrared surveys from *Herschel*, such as H-ATLAS (570 deg², Eales et al. 2010) may help with this. The present uncertainties lead to at least a factor of 2 to 3 difference in the local FIR luminosity density. However, in any case, as previously noted, in today’s relatively “dead” epoch of cosmic star formation, a significant fraction of the FIR emission from ordinary spiral galaxies may arise from dust heated by intermediate-age and older stellar populations, not newly formed OB stars, and hence is not necessarily the best measure of the star formation rate. At higher redshifts, when the cosmic specific star formation rate was much larger, new star formation should dominate dust heating, making the IR emission a more robust global tracer.

Local measurements of the stellar mass density have mainly relied on purely optical data

(e.g., SDSS photometry and spectroscopy), or relatively shallow near-infrared data from 2MASS. There may still be concerns about missing light, surface brightness biases, etc., in the 2MASS data (e.g., Bell et al. 2003), and deeper very-wide-field near-infrared data would be helpful. All-sky mid-infrared data from WISE may be valuable here, and has been used by Moustakas et al. (2013), but without extensive analysis specifically focused on this topic. Deeper near-infrared data covering a significant fraction of the sky, either from new wide-field ground-based NIR telescopes with large apertures, or from space-based surveys with *EUCLID* or *WFIRST*, would make a valuable new contribution. Otherwise, as for UV star formation rates, the most likely improvements will come from refined stellar population analyses, more so than from new data.

$0 < z < 1$ During the decline & fall of cosmic star formation, from $z \approx 1$ to 0, the greatest weakness of current measurements is that they have generally covered small sky areas and hence small comoving volumes, over rather few independent sightlines, and hence may be subject to significant cosmic variance uncertainties. Fields like GOODS, which have been analyzed many times, are too small to offer precision measurements in fine redshift bins at $z < 1$. Even the 2 deg² COSMOS field subtends less than 100 Mpc at $z < 1$ and can be spanned by large-scale structure; as a single sightline, it is subject to density fluctuations. Although very good data for measuring the SFRD or stellar mass density at $z < 1$ exist in many fields, relatively few have been analyzed thoroughly, in part because intensive effort on spectroscopic (or even photometric) redshifts has only been applied to the few, most famous fields. Sometimes even fields such as AEGIS, which has outstanding spectroscopy and deep *GALEX*, *SPITZER* and *Herschel* data, have not been fully exploited for this purpose.

For example, very deep *GALEX* data exist for several of the most famous survey fields, but the only widely-cited analysis of the UV luminosity density at $z < 1$ (Schiminovich et al. 2005) uses only ~ 1000 sources with redshifts in a single 0.5 deg² field. Expanded analysis of comparably deep *GALEX* data in COSMOS, AEGIS, and several other survey fields with existing, extensive spectroscopy is long overdue. There are no opportunities to collect more *GALEX* data, but deep *U*-band imaging measuring somewhat longer rest-frame UV wavelengths may be quite adequate for many purposes. Such data exist or could be obtained with wide-field imagers, but the best analysis to date (Cucciati et al. 2012), using ~ 11000 spectroscopic redshifts, is limited to a single 0.6 deg² sightline (indeed, the same field analyzed by Schiminovich et al. 2005 with *GALEX*). Much more work can be done to improve this situation, with relatively limited new observational effort, and often using data that already exist.

Similarly, most analyses of mid- and far-IR data from *Spitzer* and *Herschel* data have used data from at most three independent sightlines (e.g., Magnelli et al. 2009; Rodighiero et al. 2010; Gruppioni et al. 2013), nearly always combining the two GOODS fields with one shallower but wider data set (e.g., COSMOS or the VVDS-SWIRE field). The widest-area analysis to date is that of Rujopakarn et al. (2010), using 24 μm -selected sources at $z < 0.65$ from the 9 deg² Boötes survey. In practice, more data over more sightlines exist. Large consortium surveys such as the PEP and HerMES Herschel Guaranteed Time programs have mapped many fields, often with an elegant hierarchy of different areas and depths, but these have not yet been exploited and combined into a single, definitive analysis. Typically, this is because the ancillary imaging and spectroscopy needed to identify infrared source counterparts and to determine their redshifts is only available or adequate in a few fields (hence, the repeated analyses of GOODS and COSMOS).

Many of these same comments apply to stellar mass density estimates at $z < 1$. There, the state of the art has recently been improved by Moustakas et al. (2013), who analyzed five independent fields with a combined solid angle of 5.5 deg^2 with (relatively shallow) IRAC photometry and (low resolution) spectroscopic redshifts. This is the best combination of area, depth, number of sightlines, and redshift quality for any study of the stellar mass density at $z < 1$, and also superior to any data used to date for star formation rate density studies at similar redshifts. Deeper ground-based near-IR data were used by Bielby et al. (2012), analyzing four fields covering 2.1 deg^2 , and in several studies of the single 2 deg^2 COSMOS field (e.g., Ilbert et al. 2013). New wide-area surveys like VISTA VIDEO (Jarvis et al. 2012; ground-based near-IR, 3 fields, 12 deg^2) SERVS (Mauduit et al. 2012; *Spitzer* IRAC, 5 fields, 18 deg^2 , overlapping VIDEO) will provide excellent new data to improve mass function estimates, but only if adequate redshift information and supporting optical photometry are available.

$1 < z < 4$ At $z > 1$, deep surveys are needed in order to probe typical (L^* and fainter) luminosities and hence to directly detect the majority of cosmic star formation. In principle many fields have suitable data, but in practice, once again, a few survey fields have been re-analyzed many times, in part because they have the best spectroscopic and photometric redshift measurements, and in part because they have the richest multi-wavelength data, and hence are magnets for studies of all kinds. In the UV, the 1500\AA rest frame is easily probed at $z > 1.5$ using ground-based or *HST* optical imaging. At $z \approx 2$ and 3 , the surveys of Lyman break galaxies by Steidel and collaborators (e.g., Reddy & Steidel 2009) cover many independent sightlines, offering excellent control of cosmic variance, and have outstanding spectroscopic calibration. UV selection is biased against dusty star formation, but for pure measurements of the UV luminosity function that survey is arguably definitive. The best direct measurements of dust emission from *Spitzer* and *Herschel* are limited to fewer fields, and still fewer have the very deep data needed to probe galaxies near L^* . As described above, most analysis has revolved around GOODS and COSMOS, and even in GOODS, the *Herschel* data only barely reach L^* at $z = 2$. The faint end slope of the infrared luminosity function is not directly constrained by individually detected sources at $z > 2$, leading to potentially large uncertainties in any extrapolation to the bolometric IR luminosity density. With no more sensitive far-infrared space missions on the horizon, there is little prospect for wide-area surveys to fainter flux limits. ALMA can reach fainter submillimeter continuum limits and detect dust continuum from ordinary galaxies at very high redshifts, but only for very small solid angles – mosaics of hundreds or even thousands of pointings would be needed to survey a field the size of GOODS. Well-designed observations targeting intelligently selected galaxy samples, rather than panoramic mapping, may be required.

Stellar masses below the characteristic mass M^* can be probed using the best ground-based near-infrared data, and by *Spitzer* IRAC even with modest integration times, and therefore more fields have been analyzed, although GOODS and COSMOS still tend to dominate the literature. With the extended *Spitzer* warm mission, there is a wealth of valuable data already taken that has yet to be fully exploited. In practice, there is uncannily good agreement between most determinations of the stellar mass function and density at $1 < z < 4$, and it is not clear that new surveys are needed, rather than more sophisticated analysis of the existing data. However, the CANDELS *HST* WFC3 survey reaches fainter multi-band near-infrared fluxes in fields which already have the deepest IRAC data, and hence provides an important opportunity for measuring photometric redshifts and stellar

masses for galaxies fainter than the limits of most studies to date. This should provide a better constraint on the slope of the stellar mass function at low masses.

$z > 4$ At $z \geq 4$, the large majority of UV-based star formation rate and stellar mass density measurements have been derived from *HST* data, mainly in the GOODS fields and the HUDF plus its deep parallel fields (also located in and around GOODS-South). Although ground-based imaging can select galaxies at $z \geq 4$, in practice the *HST* surveys have gone deeper, especially at the very red optical wavelengths (*I* and *z*-bands) and the near-infrared wavelengths needed to select galaxies at the highest redshifts; only with these data can luminosity function measurements probe significantly fainter than L^* . GOODS also has the deepest *Spitzer* IRAC data, essential for deriving stellar masses at $z > 4$, where even the *K*-band samples rest-frame UV wavelengths. Although the comoving volumes in the GOODS fields are significant at these large redshifts (nearly 10^6 comoving Mpc^3 at $z = 4$ for the combined GOODS fields), one may still worry about clustering and cosmic variance, given only two sightlines. The CANDELS program (Grogin et al. 2011; Koekemoer et al. 2011) is obtaining multi-band optical and near-IR *HST* imaging over five fields, each similar in size, including the two GOODS fields, and is supplemented by very deep IRAC imaging from SEDS (Ashby et al. 2013) and S-CANDELS (in progress, G. Fazio, PI), and will surely help with cosmic variance control and improved statistics.

At $6 < z < 8$, the HUDF data become essential to get any handle on the faint end slope of the luminosity function, and one must surely worry about the very small field size. At $z > 8$, the HUDF (or lensing clusters) are needed simply to detect convincing candidates at all. Hence, nearly all of the literature on the SFRD or stellar masses at these redshifts consists of serial and parallel analyses of the same HUDF data sets, plus recent work from CLASH (Zheng et al. 2012; Coe et al. 2013). Here, the new Hubble Frontier Fields should be important. This program, to be executed in the 2013-2016 time frame, will obtain multiband optical and near-IR *HST* imaging with near-HUDF depth, along with ultradeep *Spitzer* IRAC data, for six massive galaxy clusters, whose lensing potential will magnify the faintest high-redshift background galaxies. In addition, there will be six new “blank” parallel fields that will improve statistics for unlensed sources and provide cosmic variance control for analyses that now depend on the HUDF (and its satellites) alone.

It should be remembered that at $z > 4$, galaxies detected in ground-based near-IR data (and at $z > 3$ for *HST* observations in the reddest WFC3-IR filters) are observed at rest-frame UV wavelengths. Hence, even with CANDELS, the HUDF and the Frontier Fields, *HST* selection will be biased against quiescent or dusty galaxies. Massive galaxies with huge star formation rates that are detected at submillimeter wavelengths but invisible even out to the *K*-band have been detected, with redshifts $z > 4$ confirmed from CO measurements (e.g., Daddi et al. 2009), but it is unknown how much they might contribute to the star formation rate or stellar mass density. IRAC selection should, in principle, provide a less biased census (e.g., Mancini et al. 2009; Huang et al. 2011; Caputi et al. 2011, 2012), but spectroscopic confirmation or even photometric redshift estimates for this population may prove to be very difficult before the launch of the *JWST*.

5 FROM OBSERVATIONS TO GENERAL PRINCIPLES

Equations (1) were first used by Lanzetta et al. (1995) (and generalized by Pei & Fall 1995 to models with inflows and outflows) to study the chemical evolution of the damped Ly α absorption systems, where one infers the comoving rate of star formation from the observed

cosmological mass density of H I. A different method was developed by Madau et al. (1996), Lilly et al. (1996), and Madau et al. (1998b), where data from galaxy surveys were used to infer the star formation density (SFRD) $\psi(t)$ directly. This new approach relies on coupling the equations of chemical evolution to the spectrophotometric properties of the cosmic volume under consideration. The specific luminosity density at time t of a “cosmic stellar population” characterized by a SFRD $\psi(t)$ and a metal-enrichment law $Z_*(t)$ is given by the convolution integral

$$\rho_\nu(t) = \int_0^t \psi(t - \tau) \mathcal{L}[\tau, Z_*(t - \tau)] d\tau, \quad (13)$$

where $\mathcal{L}_\nu[\tau, Z_*(t - \tau)]$ is the specific luminosity density radiated per unit initial stellar mass by a simple stellar population (SSP) of age τ and metallicity $Z_*(t - \tau)$. The theoretical calculation of \mathcal{L}_ν requires stellar evolutionary tracks, isochrones, and stellar atmosphere libraries. As an illustrative example of this technique, we will provide in this section an up-to-date determination of the star formation history of the universe and discuss a number of possible implications.

5.1 Star Formation Density

Rather than trying to be exhaustive, we base our modeling below on a limited number of modern (mostly post-2006) galaxy surveys (see Table 1). For the present purpose, we consider only surveys that have measured star formation rates from rest-frame far-UV (generally 1500 Å) or mid- and far-IR measurements. Other surveys of nebular line or radio emission are also important, but provide more limited or indirect information as we have discussed in earlier sections (§§4.3 and 4.4). For the infrared measurements, we emphasize surveys that make use of far-infrared data from *Spitzer* or *Herschel*, rather than relying on mid-infrared (e.g., *Spitzer* 24 μm) measurements alone, due to the complexity and lingering uncertainty over the best conversions from mid-IR luminosity to star formation rate, particularly at high redshift or high luminosity. In a few cases, we include older measurements when they are the best available, particularly for local luminosity densities from *IRAS* or *GALEX*, or *GALEX*-based measurements at higher redshifts which have not been updated since 2005.

For rest-frame FUV data, we use local *GALEX* measurements by Wyder et al. (2005) and Robotham & Driver (2011), and also include the 1500 Å *GALEX* measurements at $z < 1$ from Schiminovich et al. (2005). We use the FUV luminosity densities of Cucciati et al. (2012) at $0.1 < z < 4$, noting that for $z < 1$ these are extrapolations from photometry at longer UV rest frame wavelengths. At $1 \lesssim z \lesssim 3$ we also use FUV luminosity densities from Dahlen et al. (2007), and Reddy & Steidel (2009). At redshifts $4 \leq z \leq 8$, there have been a plethora of HST-based studies, with some groups of authors repeatedly re-analyzing samples in GOODS and the HUDF as new and improved data have accumulated. We restrict our choices to a few of the most recent analyses, taking best-fit Schechter parameters (ϕ^* , L^* , α) from Bouwens et al. (2012b) and Schenker et al. (2013). For the present analysis, we stop at $z = 8$, and do not consider estimates at higher redshifts.

For local infrared estimates of the SFRD, we use *IRAS* luminosity functions from Sanders et al. (2003) and Takeuchi et al. (2003). At $0.4 < z < 2.3$, we include data from Magnelli et al. (2009, 2011), who used stacked *Spitzer* 70 μm measurements for 24 μm -selected sources. We also use the *Herschel* far-IR luminosity functions of Gruppioni et al. (2013) and Magnelli et al. (2013). While both analyze data from the GOODS fields, Gruppioni et al. incorporate

wider/shallower data from COSMOS, while Magnelli et al. include the deepest 100 and 160 μm data from GOODS-*Herschel*, extracting sources down to the faintest limits using 24 μm prior positions.

All the surveys used here provide best-fit luminosity function parameters – generally Schechter functions for the UV data, but other functions for the IR measurements, such as double power laws or the Saunders et al. (1990) function. These allow us to integrate the luminosity function down to the same *relative* limiting luminosity, in units of the characteristic luminosity L^* . We adopt an integration limit $L_{\text{min}} = 0.03 L^*$ when computing the luminosity density ρ_{FUV} or ρ_{IR} . For the case of a Schechter function, this integral is:

$$\rho_{\text{FUV}}(z) = \int_{0.03L^*}^{\infty} L\phi(L, z)dL = \Gamma(2 + \alpha, 0.03)\phi^* L^*. \quad (14)$$

Here α denotes the faint-end slope of the Schechter parameterization, and Γ is the incomplete gamma function. The integrated luminosity density has a strong dependence on L_{min} at high redshift, where the faint-end slope is measured to be very steep, i.e., $\alpha = -2.01 \pm 0.21$ at $z \sim 7$ and $\alpha = -1.91 \pm 0.32$ at $z \sim 8$ (Bouwens et al. 2011b). Slopes of $\alpha \lesssim -2$ lead to formally divergent luminosity densities. Our choice of a limiting luminosity that is 3.8 magnitudes fainter than L^* , while sampling a significant portion of the faint-end of the FUV LF, requires only a mild extrapolation (1.3 mag) from the deepest *Hubble Space Telescope* WFC3/IR observations (~ 2.5 mag beyond L^* at $z \sim 5-8$) of the Hubble Ultra Deep Field (Bouwens et al. 2011b). For the infrared data we use analytic or numerical integrations depending on the luminosity function form adopted by each reference, but the same faint-end slope considerations apply. (Note however that some authors use logarithmic slopes for infrared luminosity functions, which differ from the linear form used in the standard Schechter formula by $\Delta\alpha = +1$.)

Multiplying the integrated FUV and IR co-moving luminosity densities by the conversion factors \mathcal{K}_{FUV} (§3.1.1) and \mathcal{K}_{IR} (§3.1.2), we obtain measurements of the “observed” UV and IR star formation rate densities, shown in Figure 8 (*left*). Here, the FUV measurements are *uncorrected* for dust attenuation. This illustrates the now well-known result that most energy from star forming galaxies at $0 < z < 2$ is absorbed and reradiated by dust; only a minority fraction emerges directly from galaxies as UV light. The gap between the UV and IR measurements increases with redshift out to at least $z \approx 1$, and then may narrow somewhat from $z = 1$ to 2. Robust measurements of the FIR luminosity density are not yet available at $z > 2.5$.

Clearly, a robust determination of dust attenuation is essential for transforming FUV luminosity densities into total SFRDs. Figure 8 (*right*) shows measurements of the effective dust extinction, $\langle k_d \rangle$, as a function of redshift. This is the multiplicative factor needed to correct the observed FUV luminosity density to the intrinsic value before extinction, or equivalently, $\langle k_d \rangle = \rho_{\text{IR}}/\rho_{\text{FUV}} + 1$ (e.g., Meurer et al. 1999). For most of the data shown in the figure, the attenuation has been estimated from the UV spectral slopes of star-forming galaxies using the attenuation–reddening relations from Meurer et al. (1999) or Calzetti et al. (2000), or occasionally from stellar population model fitting to the full UV–optical spectral energy distributions of galaxies, integrated over the observed population (e.g., Salim et al. 2007; Cucciati et al. 2012). Robotham & Driver (2011) used the empirical attenuation correction of Driver et al. (2008). We note that the estimates of UV attenuation in the local universe span quite a broad range, suggesting that there is still more work to be done to firmly pin down this quantity (and perhaps implying that we should be cautious about the estimates at higher redshift). Several studies of UV-selected galaxies at $z \geq 2$ (Reddy

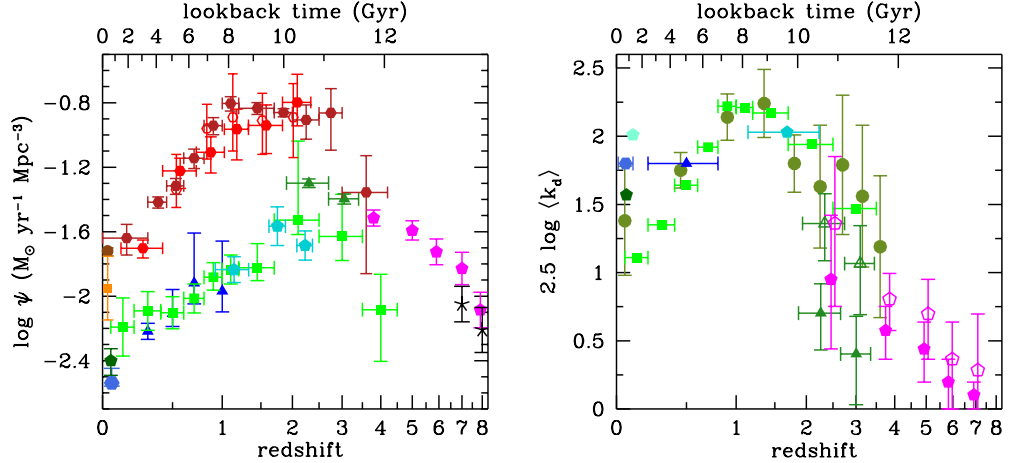


Figure 8: *Left panel*: SFR densities in the FUV (uncorrected for dust attenuation) and in the far-infrared. The data points with symbols are given in Table 1. All UV and IR luminosities have been converted to instantaneous star formation rate densities using the factors $\mathcal{K}_{\text{FUV}} = 1.15 \times 10^{-28}$ and $\mathcal{K}_{\text{IR}} = 4.5 \times 10^{-44}$ (cgs units) valid for a Salpeter IMF. *Right panel*: Mean dust attenuation in magnitudes as a function of redshift. Most of the data points shown are based on ultraviolet spectral slopes or stellar population model fitting. The symbol shapes and colors correspond to the data sets cited in Table 1, with the addition of Salim et al. (2007) (*cyan pentagon*). Two versions of the attenuation factors are shown for UV-selected galaxies at $2 < z < 7$ (Reddy & Steidel 2009; Bouwens et al. 2012a; offset slightly in the redshift axis for clarity): one integrated over the observed population (*filled symbols*), the other extrapolated down down to $L_{\text{FUV}} = 0$ (*open symbols*). Data points from Burgarella et al. (2013) (*olive green dots*) are calculated by comparing the integrated FIR and FUV luminosity densities in redshift bins, rather than from the UV slopes or UV-optical spectral energy distributions.

& Steidel 2009; Bouwens et al. 2012a; Finkelstein et al. 2012b) have noted strong trends for less luminous galaxies to have bluer UV spectral slopes, and hence lower inferred dust attenuation. Because the faint end slope of the FUV luminosity function is so steep at high redshift, a large fraction of the reddened FUV luminosity density is emitted by galaxies much fainter than L^* , this extinction–luminosity trend also implies that the net extinction for the entire population will be a function of the faint integration limit for the sample. As an illustration, in Figure 8 (*right*), the points from Reddy & Steidel (2009) (at $z = 2.3$ and 3.05) and from Bouwens et al. (2012a) (at $2.5 \leq z \leq 7$) are shown for two faint-end integration limits: roughly down to the observed faint limit of the data, $M_{\text{FUV}} < -17.5$ to -17.7 for the different redshift subsamples, and extrapolated to $L_{\text{FUV}} = 0$. The net attenuation for the brighter limit, which more nearly represents the sample of galaxies actually observed in the study, is significantly larger than for the extrapolation – nearly two times larger for the Reddy & Steidel (2009) samples, and by a lesser factor for the more distant objects from Bouwens et al. (2012a). In our analysis of the star formation rate densities, we have adopted the mean extinction factors inferred by each survey to correct the corresponding FUV luminosity densities.

Adopting a different approach, Burgarella et al. (2013) measured total UV attenuation from the ratio of far-infrared to observed (uncorrected) far-ultraviolet luminosity densities (Fig. 8 *left*) as a function of redshift, using FUV luminosity functions from Cucciati et al. (2012) and *Herschel* FIR luminosity functions from Gruppioni et al. (2013). At $z < 2$, these

agree reasonably well with the measurements inferred from the UV slope or from SED fitting. At $z > 2$, the FIR/FUV estimates have large uncertainties due to the similarly large uncertainties required to extrapolate the observed FIR luminosity functions to a total luminosity density. The values are larger than those for the UV-selected surveys, particularly when compared to the UV values extrapolated to very faint luminosities. While it is plausible that galaxies with lower star formation rates may have reduced extinction, it is also likely that purely UV-selected samples at high redshift are biased against dusty star-forming galaxies. As we have noted earlier, there is not yet a robust census for star-forming galaxies at $z \gg 2$ selected on the basis of dust emission alone, due to the sensitivity limits of past and present far-infrared and submillimeter observatories, and the total amount of star formation that is missed from UV surveys at such high redshifts remains uncertain.

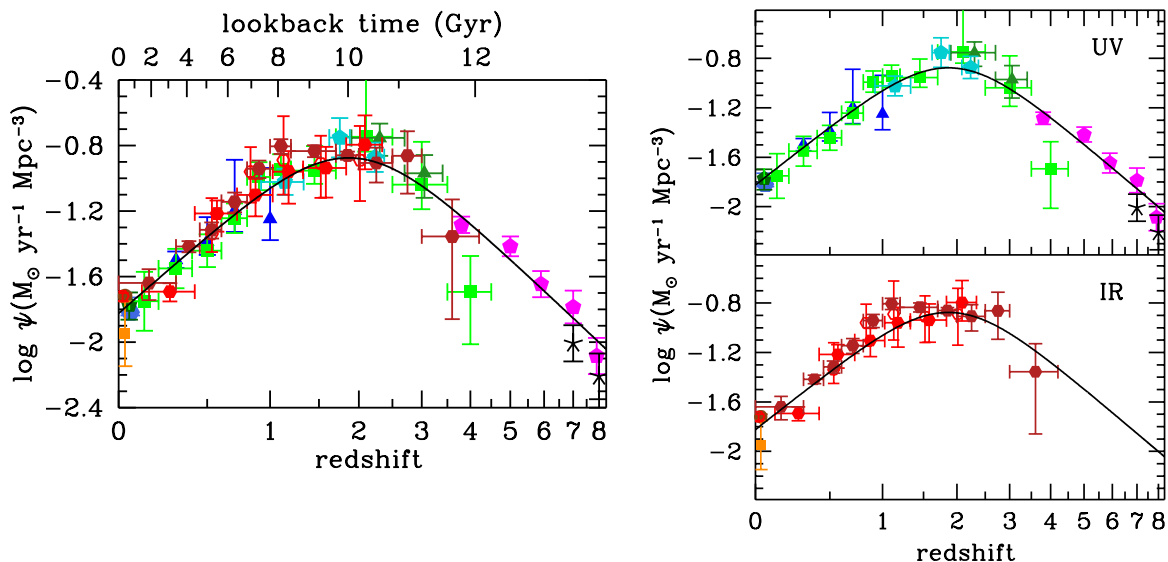


Figure 9: The history of cosmic star formation from far-ultraviolet (*top right panel*), infrared (*bottom right panel*), and FUV+IR (*left panel*) rest-frame measurements. The data points with symbols are given in Table 1. All UV luminosities have been converted to instantaneous star formation rate densities using the factor $\mathcal{K}_{\text{FUV}} = 1.15 \times 10^{-28}$ (see eq. 10), valid for a Salpeter IMF. Far-infrared luminosities (8–1000 μm) have been converted to instantaneous star formation rates using the factor $\mathcal{K}_{\text{IR}} = 4.5 \times 10^{-44}$ (see eq. 11), also valid for a Salpeter IMF. The best-fit star formation rate density in equation (15) is plotted in the three panels with the solid curve.

Figure 9 shows the history of cosmic star formation from UV and IR data following the above prescriptions, together with the best-fitting function

$$\psi(z) = 0.015 \frac{(1+z)^{2.7}}{1 + [(1+z)/2.9]^{5.6}} \text{ M}_{\odot} \text{ yr}^{-1} \text{ Mpc}^{-3}. \quad (15)$$

These state-of-the-art surveys provide a remarkably consistent picture of the cosmic star formation history: a rising phase, scaling as $\psi(z) \propto (1+z)^{-2.9}$ at $3 \lesssim z \lesssim 8$, slowing and peaking at some point probably between $z = 2$ and 1.5, when the universe was about 3.5 Gyr old, followed by a gradual decline to the present day, roughly as $\psi(z) \propto (1+z)^{2.7}$.

The co-moving SFRD at redshift 7 was about the same as that measured locally. The increase in $\psi(z)$ from $z \approx 8$ to 3 appears to have been steady, with no sharp drop at the highest redshifts, although there is now active debate in the literature about whether that trend continues or breaks at redshifts 9 and beyond (Coe et al. 2013; Ellis et al. 2013; Oesch et al. 2013). While we have adopted here a fitting function that is a double power-law in $(1+z)$, we note that the SFRD data at $z < 1$ can also be fit quite well by an exponential decline with cosmic time and an e-folding timescale of 3.9 Gyr. Compared to the recent empirical fit to the SFRD by Behroozi et al. (2013), the function in equation (15) reaches its peak at a slightly higher redshift, with a lower maximum value of ψ , and with slightly shallower rates of change at both lower and higher redshift, and produces 20% less stars by $z = 0$.

We also note that each published measurement has its own approach to computing uncertainties on the SFRD, taking different random and systematic factors into account, and we have made no attempt to rationalize these here. Moreover, the published studies integrate their measurements down to different luminosity limits. We have instead adopted a fixed threshold of $0.03 L^*$ for integrating the published luminosity functions, and given the covariance on the measurements and uncertainties of luminosity function parameters, there is no simple way for us to correct the published uncertainties to be appropriate for our adopted integration limit. Therefore, we have simply retained the fractional errors on the SFRD measurements published by each author without modification, in order to provide an indication of the relative inaccuracy derived by each study. These should not be taken too literally. This is particularly true when there is significant difference in the faint end slopes of luminosity functions reported in different studies, which can lead to large differences in the integrated luminosity density. Uncertainties in the faint end slope and the result extrapolations are not always taken fully into account in published error analyses, especially when luminosity functions are fit at high redshift by fixing the slope to some value measured only at lower redshift.

5.2 Core-Collapse Supernova Rate

Since core-collapse supernovae (i.e., Type II and Ibc supernovae, hereafter CC SNe) originate from massive, short-lived stars, the rates of these events should reflect ongoing star formation and offer an independent determination of the cosmic star formation and metal production rates at different cosmological epochs (e.g., Madau et al. 1998a; Dahlen et al. 2004). While poor statistics and dust obscuration are major limiting factors for using CC SNe as a tracer of the SFH of the universe, most derived rates are consistent with each other and increase with lookback time between $z = 0$ and $z \sim 1$ (see Fig. 10). The comoving volumetric SN rate is determined by multiplying equation (15) by the efficiency of forming CC SNe

$$R_{CC}(z) = \psi(z) \times \frac{\int_{m_{\min}}^{m_{\max}} \phi(m) dm}{\int_{m_l}^{m_u} m \phi(m) dm} \equiv \psi(z) \times k_{CC}, \quad (16)$$

where for our reference Salpeter IMF and canonical parameters for CC SNe, $m_{\min} = 8 M_{\odot}$ and $m_{\max} = 40 M_{\odot}$, the number of stars that explode as SNe per unit mass is $k_{CC} = 0.0068 M_{\odot}^{-1}$. The predicted cosmic SN rate is shown in Figure 10, and appears to be in good agreement with the data. Note that the IMF dependence in equation (16) is largely canceled out by the IMF dependence of the derived SFRD $\psi(z)$, as the stellar mass range probed by SFR indicators is comparable to the mass range of stars exploding as CC SNe. Recent

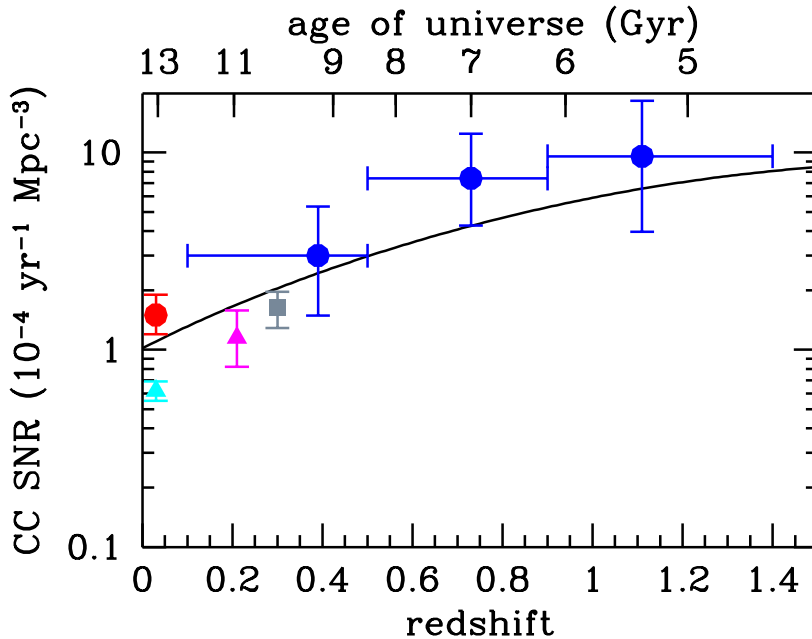


Figure 10: The cosmic core-collapse SN rate. The data points are taken from Li et al. (2011) (*cyan triangle*), Mattila et al. (2012) (*red dot*), Botticella et al. (2008) (*magenta triangle*), Bazin et al. (2009) (*gray square*), and Dahlen et al. (2012) (*blue dots*). The solid line shows the rates predicted from our fit to the cosmic star formation history. Note that the local rate within 10-15 Mpc of Mattila et al. (2012) may be boosted by the local overdensity in star formation.

comparisons between star formation and CC SN rates have suggested a discrepancy between the two, with the numbers of CC SNe detected being too low by about a factor of two (Horiuchi et al. 2011). Our revised cosmic star formation history does not appear to show such systematic discrepancy (see also Dahlen et al. 2012).

Observations show that at least some long-duration gamma-ray bursts (GRBs) happen simultaneously with CC SNe, but neither all SNe, nor even all SNe of Type Ibc produce GRBs (see Woosley & Bloom 2006 for a review). While the rate of GRBs of this class could in principle provide a complementary estimate of the SFRD (e.g., Porciani & Madau 2001), such rate is only a small fraction (<1% after correction for beaming) of the CC SN rate (Gal-Yam et al. 2006), suggesting that GRBs are an uncommon chapter in the evolution of massive stars, requiring special conditions that are difficult to model. Recent studies of the GRB-SFR connection have claimed that GRBs do not trace the SFR in an unbiased way, and are more frequent per unit stellar mass formed at early times (Kistler et al. 2009; Robertson & Ellis 2012; Trenti et al. 2012).

5.3 Stellar Mass Density

Figure 11 shows a compilation (see also Table 2) of recent (mostly post-2006) measurements of the SMD as a function of redshift (for a compilation of older data see Wilkins et al.

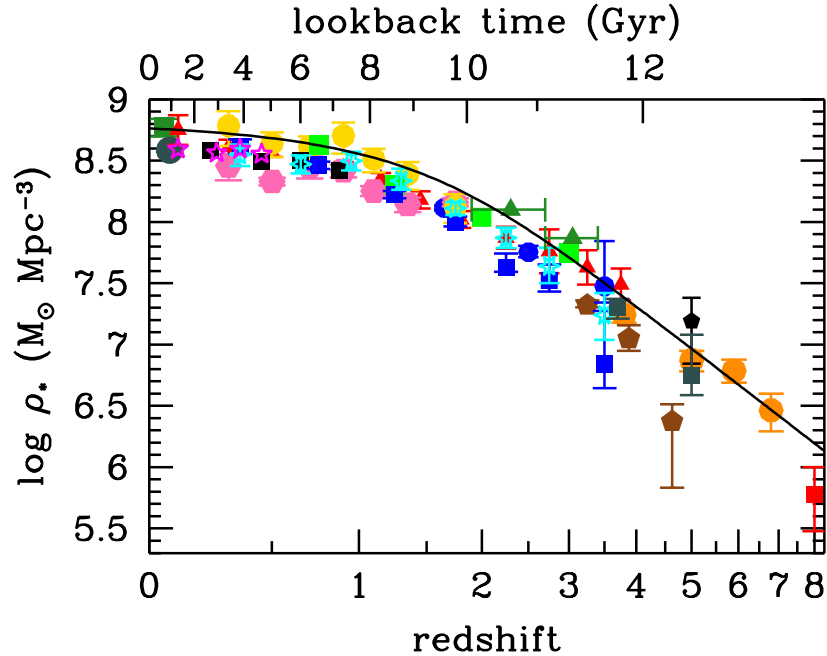


Figure 11: The evolution of the stellar mass density. The data points with symbols are given in Table 2. The solid line shows the prediction generated by integrating the instantaneous star formation rate density ψ (eqs. 2 and 15, with $R = 0.27$).

2008a). We show local SDSS-based SMDs from Gallazzi et al. (2008), Li & White (2009), and Moustakas et al. (2013). Moustakas et al. also measured stellar mass functions at $0.2 < z < 1$, but at $z > 0.5$ their mass completeness limit is larger than $10^{9.5} M_{\odot}$, so we have only used their points below that redshift. At higher redshifts (and, indeed, in Moustakas et al.), nearly all of the modern estimates incorporate *Spitzer* IRAC photometry; we include only one recent analysis (Bielby et al. 2012) which does not, but which otherwise uses excellent deep, wide-field near-IR data in four independent sightlines. Otherwise, we include measurements at $0.1 < z \lesssim 4$ from Arnouts et al. (2007), Pérez-González et al. (2008), Kajisawa et al. (2009), Marchesini et al. (2009), Pozzetti et al. (2010), Reddy & Steidel (2012), Ilbert et al. (2013), and Muzzin et al. (2013). We show measurements for the IRAC-selected sample of Caputi et al. (2011) at $3 \leq z \leq 5$, and for UV-selected LBG samples at $4 < z < 8$ by Yabe et al. (2009), González et al. (2011), Lee et al. (2012), and Labbé et al. (2013).

When needed, we have scaled from a Chabrier IMF to a Salpeter IMF by multiplying the stellar masses by a factor of 1.64 (Figure 4). At high redshift, authors often extrapolate their stellar mass functions beyond the observed range by fitting a Schechter function. Stellar mass completeness at any given redshift is rarely as well defined as luminosity completeness, given the broad range of M/L values that galaxies can exhibit. Unlike the luminosity functions used for the SFRD calculations, where we have tried to impose a consistent faint luminosity limit (relative to L^*) for integration, in most cases we have simply accepted

whatever low-mass limits or integral values that the various authors have reported. Many authors have found that the characteristic mass M^* appears to change rather little for $0 < z < 3$ (e.g., Fontana et al. 2006; Ilbert et al. 2013), and is roughly $10^{11} M_\odot$ (Salpeter). Therefore, a low-mass integration limit similar to that which we used for the luminosity functions ($L_{\min} = 0.03L^*$) would correspond to $M_{\min} \approx 10^{9.5} M_\odot$ in that redshift range. A common but by no means universal low mass integration limit used in the literature is $10^8 M_\odot$. Generally, stellar mass functions are found to have flatter low-mass slopes than are UV (and sometimes IR) luminosity functions, so the lower mass limit makes less difference to the SMDs than it does to the SFRDs.

The solid line in Figure 11 shows the global SMD obtained by integrating our best-fit instantaneous SFRD $\psi(z)$ (eqs. 2 and 15), with a return fraction $R = 0.27$. Our model predicts an SMD that is somewhat high (about 0.2 dex on average, or 60%) compared to many, but not all, of the data at $0 < z \lesssim 3$. At $0.2 < z < 2$ our model matches the SMD measurements for the *Spitzer* IRAC-selected sample of Arnouts et al. (2007), but several other modern measurements in this redshift range from COSMOS (Pozzetti et al. 2010; Ilbert et al. 2013; Muzzin et al. 2013) fall below our curve. Carried down to $z = 0$, our model is somewhat high compared to several local estimates of the SMD (e.g., Cole et al. 2001; Baldry et al. 2008; Li & White 2009), but not all (Gallazzi et al. 2008).

Several previous analyses (Hopkins & Beacom 2006, but see the erratum, Hopkins & Beacom 2008; Wilkins et al. 2008a) have found that the instantaneous SFH over-predicts the SMD by larger factors, up to 0.6 dex at redshift 3. We find little evidence for such significant discrepancies, although there does appear to be a net offset over a broad redshift range. While smaller, a $\sim 60\%$ effect should not be disregarded. One can imagine several possible causes for this discrepancy; we consider several of these here.

Star formation rates may be overestimated, particularly at high redshift during the peak era of galaxy growth. For UV-based measurements, a likely culprit would be the luminosity-weighted dust corrections, which could be too large, although it is often asserted instead that UV data are likely to *underestimate* SFRs in very dusty, luminous galaxies. Infrared-based SFRs may be overestimated, and indeed *were* overestimated for some high-redshift galaxies in earlier *Spitzer* studies, although this seems less likely now in the era of deep *Herschel* FIR measurements. It seems more plausible that the SFRs inferred for individual galaxies themselves may be correct on average, but that the luminosity function extrapolations could be too large – many authors either adopt fairly steep ($\alpha \geq -1.6$) faint-end slopes to both the UV and IR LFs for distant galaxies. For the UVLFs, the best modern data constrain these slopes quite well, but in the infrared current measurements are not deep enough to do so. However, while these extrapolations may be uncertain, the good agreement between the current best estimates of the UV- and IR-based SFRDs at $0 < z < 2.5$ (Fig. 9) does not clearly point to a problem in either one.

Instead, stellar masses or their integrated SMD may be systematically underestimated. This is not implausible, particularly for star-forming galaxies, where the problem of recent star formation “outshining” older high M/L stars is well known (see §5.1). By analyzing mock catalogs of galaxies drawn from simulations with realistic (and complex) star formation histories, Pforr et al. (2012) find that the simplifying assumptions that are typically made when modeling stellar masses for real surveys generally lead to systematically underestimated stellar masses at all redshifts. That said, other systematic effects systematics can work in the opposite direction and lead to mass overestimates, e.g., the effects of TP-AGB stars on the red and near-infrared light if these are not correctly modeled (Maraston 2005). A steeper low-mass slope to the galaxy SMF could also increase the total SMD. This has

been suggested even at $z = 0$, where mass functions have been measured with seemingly great precision and dynamic range (e.g., Baldry et al. 2008). At high redshift, most studies to date have found relatively flat low-mass SMF slopes, but galaxy samples may be incomplete (and photometric redshift estimates poor) for very faint, red, high- M/L galaxies if they exist in significant numbers. Some recent SMF determinations using very deep *HST* WFC3 observations have found steeper SMF slopes at $z > 1.5$ (e.g., Santini et al. 2012), and new measurements from extremely deep near-infrared surveys like CANDELS are eagerly anticipated. That said, it seems unlikely that the SMF slope at *low* redshift has been underestimated enough to account for a difference of 0.2 dex in the SMD.

Recent evidence has suggested that strong nebular line emission can significantly affect broad band photometry for galaxies at high redshift, particularly $z > 3.8$, where $H\alpha$ (and, at $z > 5.3$, [OIII]) enter the *Spitzer* IRAC bands (Shim et al. 2011). Following Stark et al. (2013), we have therefore divided the SMD of González et al. (2011) at $z \simeq 4, 5, 6$, and 7 in Figure 11 by the factor 1.1, 1.3, 1.6, and 2.4, respectively, to account for this effect. While there are still considerable uncertainties in these corrections, such downward revision to the inferred early SMD clearly improve consistency with expectations from the time integrated SFRD.

Alternatively, some authors have considered how changing the IMF might help reconcile $SMD(z)$ with the time-integrated $SFRD(z)$ (e.g., Wilkins et al. 2008b). Generally, a more top-heavy or bottom-light IMF will lead to larger luminosities per unit SFR, hence smaller SFR/L conversion factors K (§3.1). Mass-to-light ratios for older stellar populations will also tend to be smaller, however, but not necessarily by the same factor. Although we have used a Salpeter IMF for reference in this review, an IMF with a low-mass turnover (e.g., Chabrier or Kroupa) will yield a larger mass return fraction R and hence proportionately lower final stellar masses for a given integrated past star formation history, by a factor $(1 - R_1)/(1 - R_2) = 0.81$, where R_1 and $R_2 = 0.41$ and 0.27 for Chabrier and Salpeter IMFs, respectively (§2). The apparent offset between the SMD data and our integrated model $\psi(z)$ can therefore be reduced further, to only ~ 0.1 dex, without invoking a particularly unusual IMF. Given the remaining potential for systemic uncertainties in the measurements of SFRDs and SMDs, it seems premature to tinker further with the IMF, although if discrepancies remain after further improvements in the measurements and modeling then this topic may be worth revisiting.

5.4 Fossil Cosmology

In concordance with estimates from the cosmic star formation history, the measurements of the SMD discussed above imply that galaxies formed the bulk ($\gtrsim 75\%$) of their stellar mass at $z < 2$. Stars formed in galaxies before 11.5 Gyr are predicted to contribute only 8% of the total stellar mass today. An important consistency check for all these determinations could then come from studies of the past star formation history of the universe from its present contents. This “fossil cosmology” approach has benefited from large spectroscopic surveys in the local universe, such as the 2dFGRS (Colless et al. 2001) and the SDSS (York et al. 2000), which provide detailed spectral information for hundreds of thousands of galaxies. Using a sample of 1.7×10^5 galaxies drawn from the SDSS DR2, and comparing the spectrum of each galaxy to a library of Bruzual & Charlot (2003) templates (the comparison was based on five spectral absorption features, namely D4000, $H\beta$, and $H\delta_A + H\gamma_A$ as age-sensitive indices, and $[Mg_2Fe]$ and $[MgFe]'$ as metal-sensitive indices), Gallazzi et al. (2008) have constructed a distribution of stellar mass as a function of age (see also Panter et al. 2007

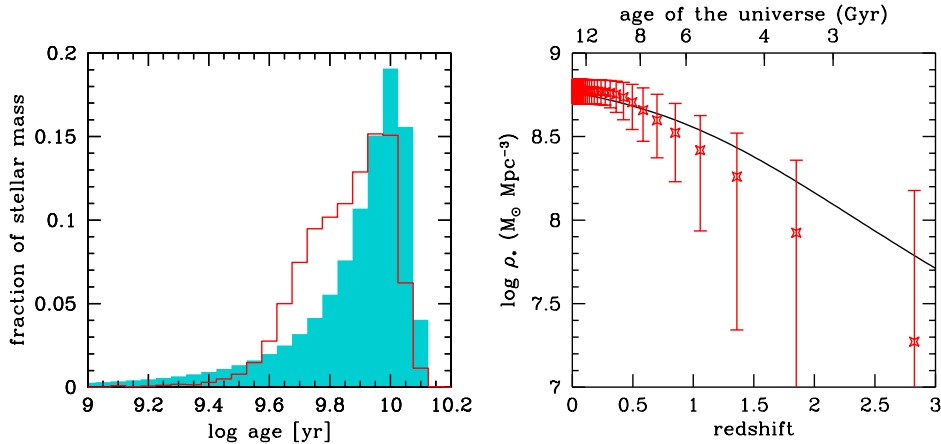


Figure 12: “Stellar archaeology” with the SDSS. *Left panel:* Normalized distribution of stellar mass in the local universe as a function of age. *Red histogram:* estimates from the SDSS (Gallazzi et al. 2008). The measured (mass-weighted) ages have been corrected by adding the lookback time corresponding to the redshift at which the galaxy is observed. *Turquoise shaded histogram:* distribution generated by integrating the instantaneous star formation rate density in eq. (2). *Right panel:* Evolution of the stellar mass density with redshift. The points, shown with systematic error bars, are derived from the analysis of SDSS data by Gallazzi et al. (2008), assuming a Salpeter IMF in the range $0.1 - 100 M_{\odot}$. The solid line shows the mass assembly history predicted by integrating our best-fit SFH.

for a similar analysis on the SDSS DR3 sample). In the left panel of Figure 12 we compare this distribution with the one predicted by our best-fit cosmic SFH. The latter implies a mass-weighted mean stellar age,

$$\langle t_{\text{age}} \rangle = t_0 - \int_0^{t_0} t\psi(t)dt \left[\int_0^{t_0} \psi(t)dt \right]^{-1}, \quad (17)$$

equal to $\langle t_{\text{age}} \rangle = 8.3$ Gyr. Both distributions have a peak at $8 - 10$ Gyr and decline rapidly at younger ages, with the peak age corresponding to the formation redshift, $z \sim 2$, where the cosmic star formation density reaches a maximum. The SDSS distribution, however, appears to be skewed towards younger ages. This is partly caused by a bias toward younger populations in the SDSS “archaeological” approach, where individual galaxies are only assigned an average (weighted by mass or light) age that is closer to the last significant episode of star formation. Such bias appears to be reflected in the right panel of Figure 12, where the mass assembly history predicted by our model SFH is compared with that inferred by translating the characteristic age of the stellar populations measured by Gallazzi et al. into a characteristic redshift of formation. The agreement is generally good, although the SDSS distribution would predict later star formation and more rapid SMD growth at $z < 2$, and correspondingly less stellar mass formed at $z > 2$. The present-day total SMD derived by Gallazzi et al. is $(6.0 \pm 1.0) \times 10^8 M_{\odot} \text{Mpc}^{-3}$ (scaled up from a Chabrier to a Salpeter IMF), in excellent agreement with $\rho_* = 5.8 \times 10^8 M_{\odot} \text{Mpc}^{-3}$, predicted by our model SFH. This stellar density corresponds to a stellar baryon fraction of only 9% (5% for a Chabrier IMF).

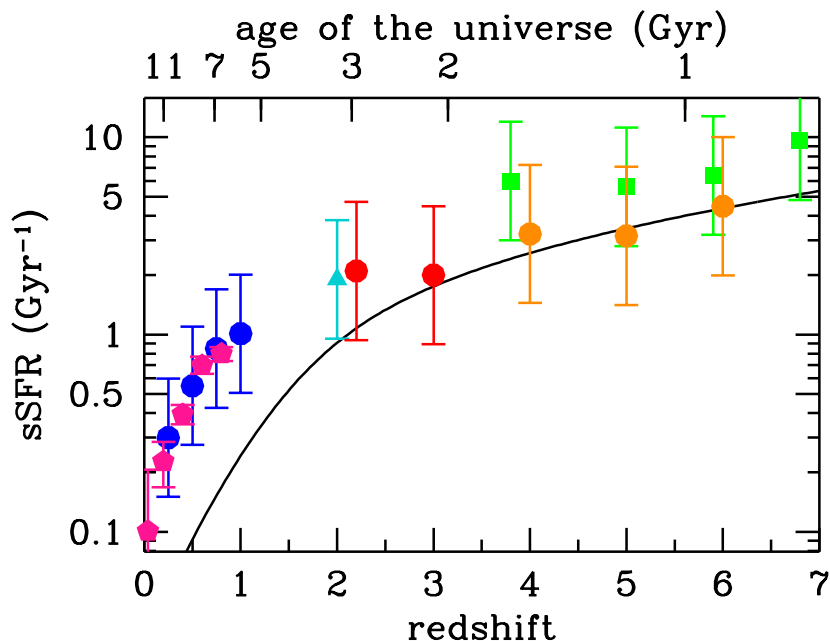


Figure 13: The mean specific star formation rate ($sSFR \equiv SFR/M_*$) for galaxies with estimated stellar masses in the range $10^{9.4} - 10^{10} M_\odot$. The values are taken from the literature: Damen et al. (2009) (*magenta pentagons*), Noeske et al. (2007) (*blue dots*), Daddi et al. (2007) (*cyan triangle*), Reddy et al. (2012) (*red dots*), Stark et al. (2013) (*green squares*), and González et al. (2012) (*orange dots*). The error bars correspond to systematic uncertainties. The González et al. (2012) and Stark et al. (2013) high-redshift points have been corrected upwards for the effect of optical emission lines on the derived stellar masses, using their “RSF with emission lines” model (González et al. 2012) and “fixed $H\alpha$ EW” model (Stark et al. 2013). The curve shows the predictions from our best-fit SFH.

5.5 The Global Specific Star Formation Rate

In recent years, there has been considerable interest in the “specific star formation rate” ($sSFR \equiv SFR/M_*$) of galaxies with different masses at different times in the history of the universe. The $sSFR$ describes the fractional growth rate of stellar mass in a galaxy, or equivalently, the ratio of current to past star formation. The inverse of the $sSFR$ is the characteristic stellar mass doubling time (Guzman et al. 1997). At $0 < z < 2$ and quite possibly at higher redshifts, most star-forming galaxies follow a reasonably tight relation between SFR and M_* , whose normalization (e.g., the mean $sSFR$ at some fiducial mass) decreases steadily with cosmic time (decreasing redshift) at least from $z = 2$ to the present (Brinchmann et al. 2004; Noeske et al. 2007; Elbaz et al. 2007; Daddi et al. 2007). A minority population of starburst galaxies exhibits elevated $sSFR$ s, while quiescent or passive galaxies lie below the $SFR-M_*$ correlation. For the “main sequence” of star forming galaxies, most studies find that the average $sSFR$ is a mildly declining function of stellar mass (e.g., Karim et al. 2011). This implies that more massive galaxies completed the bulk of their star formation earlier than that did lower-mass galaxies (Brinchmann & Ellis 2000; Juneau et al. 2005), a “downsizing” picture first introduced by Cowie et al. (1996). Dwarf galaxies continue to undergo major episodes of activity until the present day. The tightness of this $SFR-M_*$ correlation has important implications for how star formation is regulated within

galaxies, and perhaps for the cosmic star formation history itself. Starburst galaxies, whose SFRs are significantly elevated above the main sequence correlation, contribute only a small fraction of the global SFRD at $z \leq 2$ (Rodighiero et al. 2011; Sargent et al. 2012). Instead, the evolution of the cosmic star formation rate is primarily due to the steadily-evolving properties of main sequence disk galaxies.

Figure 13 compares the sSFR (in Gyr^{-1}) for star-forming galaxies with estimated stellar masses in the range $10^{9.4} - 10^{10} M_{\odot}$ from a recent compilation by González et al. (2012), with the predictions from our best-fit star formation history. At $z < 2$, the globally averaged sSFR ($\equiv \psi/\rho_*$) declines more steeply than does that for the star-forming population, as star formation is “quenched” for an increasingly large fraction of the galaxy population. These passive galaxies are represented in the global sSFR, but not in the sSFR of the star-forming “main sequence”. Previous derivations showed a nearly constant sSFR of $\sim 2 \text{Gyr}^{-1}$ for galaxies in the redshift range $2 < z < 7$, suggesting relatively inefficient early star formation and exponential growth in star formation rates and stellar masses with cosmic time. Recent estimates of reduced stellar masses, derived after correcting for nebular emission in broad band photometry, appear instead to require some evolution in the high- z sSFR (Stark et al. 2013; González et al. 2012). At these epochs, the global sSFR is found to decrease with increasing cosmic time t as $\text{sSFR} \sim 4/t \text{Gyr}^{-1}$, a consequence of the power-law scaling of our SFRD, $\psi(t) \propto t^{1.9}$.

5.6 Cosmic Metallicity

According to equation (4), the sum of the heavy elements stored in stars and in the gas phase at any given time, $Z\rho_g + \langle Z_* \rangle \rho_*$, is equal to the total mass of metals produced over cosmic history, $y\rho_*$. It is sometime useful to express this quantity relative to the baryon density,

$$Z_b(z) \equiv \frac{y\rho_*(z)}{\rho_b}, \quad (18)$$

where $\rho_b = 2.77 \times 10^{11} \Omega_b h^2 M_{\odot} \text{Mpc}^{-3}$. The evolution of the “mean metallicity of the universe”, Z_b , predicted by our model SFH is plotted in Figure 14. The global metallicity is $Z_b \simeq 0.09 (y/Z_{\odot})$ solar at the present epoch (note that this is the same value derived by Madau et al. 1998b). It drops to $Z_b \simeq 0.01 (y/Z_{\odot})$ solar at $z = 2.5$, i.e., the star formation activity we believe to have taken place between the Big Bang and $z = 2.5$ (2.5 Gyr later) was sufficient to enrich the universe as a whole to a metallicity of about 1 percent solar (for $y \simeq Z_{\odot}$). Note that the metal production term $y\rho_*$ (and therefore Z_b) depends only weakly on the IMF (at a fixed luminosity density): while Salpeter-based mass-to-light ratios are 1.64 times higher than those based on Chabrier, this is counterbalanced by Salpeter-based net metal yields that are about a factor of 2 lower than those based on Chabrier (see § 2).

The figure also shows the metallicity of a variety of astrophysical objects at different epochs. The mass-weighted average stellar metallicity in the local universe, $\langle Z_*(0) \rangle = (1.04 \pm 0.14) Z_{\odot}$ (Gallazzi et al. 2008), is plotted together with the metallicity of three different gaseous components of the distant universe: 1) galaxy clusters, the largest bound objects for which chemical enrichment can be thoroughly studied, and perhaps the best example in nature of a “closed box” (green triangles); 2) the damped $\text{Ly}\alpha$ absorption systems (DLAs) that originate in galaxies and dominate the neutral-gas content of the universe (red pentagons); and 3) the highly ionized circumgalactic and intergalactic gas that participates to the cycle of baryons in and out of galaxies in the early universe (orange dot, black pentagon, and magenta rectangle).

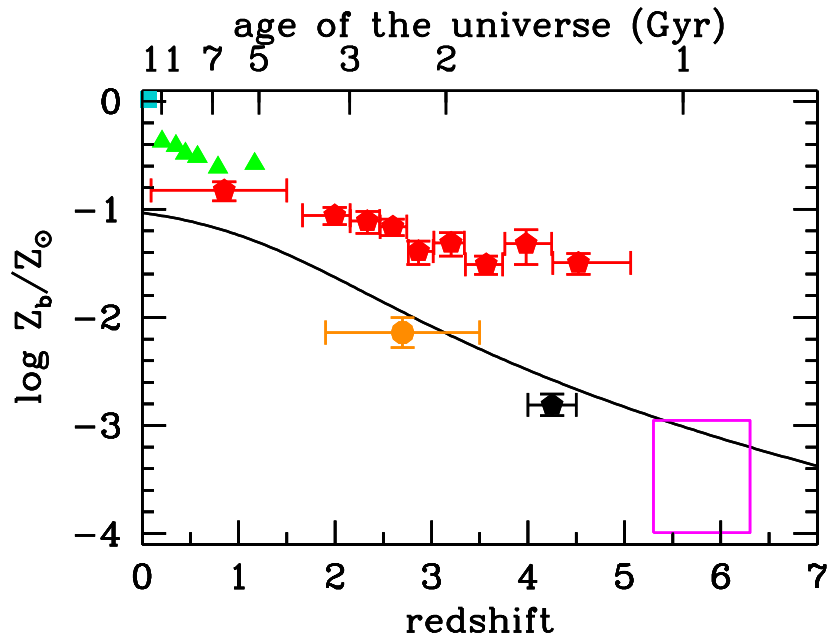


Figure 14: Mean metallicity of the universe (in solar units). *Solid curve*: mass of heavy elements ever produced per cosmic baryon from our model SFH, for an assumed IMF-averaged yield of $y = 0.02$. *Turquoise square*: mass-weighted stellar metallicity in the nearby universe from the SDSS (Gallazzi et al. 2008). *Green triangles*: mean iron abundances in the central regions of galaxy clusters (Balestra et al. 2007). *Red pentagons*: column density-weighted metallicities of the damped Ly α absorption systems (Rafelski et al. 2012). *Orange dot*: metallicity of the IGM as probed by O VI absorption in the Ly α forest (Aguirre et al. 2008). *Black pentagon*: metallicity of the IGM as probed by C IV absorption (Simcoe 2011). *Magenta rectangle*: metallicity of the IGM as probed by C IV and C II absorption (Ryan-Weber et al. 2009; Simcoe et al. 2011; Becker et al. 2011).

The iron mass in clusters is several times larger that could have been produced by CC SNe if stars formed with a standard IMF, a discrepancy that may point out to an IMF in clusters that is skewed toward high-mass stars (e.g., Portinari et al. 2004) and/or to an enhanced Fe production by Type Ia SNe (e.g., Maoz & Gal-Yam 2004). The DLAs are detected in absorption (i.e., have no luminosity bias) and their large optical depths at the Lyman limit eliminates the need for uncertain ionization corrections to deduce metal abundances. Their metallicity, determined with the highest confidence from elements like O, S, Si, Zn, and Fe, decreases with increasing redshift down to $\approx 1/600$ solar to $z \sim 5$ (e.g., Rafelski et al. 2012). The enrichment of the circumgalactic medium, as probed in absorption by C III, C IV, Si III, Si IV, O VI, and other transitions, provides us with a record of past star formation and of the impact of galactic winds on their surroundings. Figure 14 shows that the ionization-corrected metal abundances from O VI absorption at $z \sim 3$ (Aguirre et al. 2008) and C IV absorption at $z \sim 4$ (Simcoe 2011) track well the predicted mean metallicity of the universe, i.e. that these systems are an unbiased probe of the cosmic baryon cycle.

The universe at redshift 6 remains one of the most challenging observational frontiers, as the high opacity of the Ly α forest inhibits detailed studies of hydrogen absorption along

the line-of-sight to distant quasars. In this regime, the metal lines which fall longwards of the Ly α emission take on a special significance as the only tool at our disposal to recognize individual absorption systems, whether in galaxies or the IGM, and probe cosmic enrichment following the earliest episodes of star formation. Here, we have used recent surveys of high- and low-ionization intergalactic absorption to estimate the metallicity of the universe at these extreme redshifts. According to Simcoe et al. (2011) (see also Ryan-Weber et al. 2009), the comoving mass density of triply ionized carbon over the redshift range 5.3 – 6.4 is (expressed as a fraction of the critical density) $\Omega_{\text{CIV}} = (0.46 \pm 0.20) \times 10^{-8}$. Over a similar redshift range, C II absorption yields $\Omega_{\text{CII}} = 0.9 \times 10^{-8}$ (Becker et al. 2011). The total carbon metallicity by mass, Z_{C} , at $\langle z \rangle = 5.8$ implied by these measurements is then

$$Z_{\text{C}} = \frac{\Omega_{\text{CIV}} + \Omega_{\text{CII}}}{\Omega_b} \times \frac{C}{C_{\text{II}} + C_{\text{IV}}} \simeq 3 \times 10^{-7} \frac{C}{C_{\text{II}} + C_{\text{IV}}}, \quad (19)$$

where $(C_{\text{II}} + C_{\text{IV}})/C$ is the fraction of carbon that is either singly or triply ionized. In Figure 14 we have plot Z_{C} in units of the mass fraction of carbon in the Sun, $Z_{\text{C}\odot} = 0.003$ (Asplund et al. 2009). The lower bound to the rectangle centered at redshift 5.8 assumes no ionization correction, i.e., $(C_{\text{II}} + C_{\text{IV}})/C = 1$. To derive the upper bound, we have adopted the conservative limit $(C_{\text{II}} + C_{\text{IV}})/C \geq 0.1$; this is the minimum fractional abundance reached by C $\text{II} + \text{CIV}$ under the most favorable photoionization balance conditions at redshift 6.⁹ Clearly, if the ionization state of the early metal-bearing IGM is such that most of the C is either singly or triply ionized, then most of the heavy elements at these epochs appear to be “missing” compared to the expectations based on the integral of the cosmic SFH (Ryan-Weber et al. 2009; Pettini 2006). Conversely, if C II and C IV are only trace ion stages of carbon, then the majority of the heavy elements produced by stars 1 Gyr after the Big Bang ($z = 6$) may have been detected already.

A simple argument can also be made against the possibility that our best-fit SFH significantly overpredicts the cosmic metallicity at these early epoch. The massive stars that explode as Type II SNe and seed the IGM with metals are also the sources of nearly all of the Lyman-continuum (LyC) photons produced by a burst of star formation. It is then relatively straightforward to link a given IGM metallicity to the minimum number of LyC photons that must have been produced up until that time. The close correspondence between the sources of metals and photons makes the conversion from one to the other largely independent of the details of the stellar IMF (Madau & Shull 1996). Specifically, the energy emitted in hydrogen ionizing radiation per baryon, E_{ion} , is related to the average cosmic metallicity by

$$E_{\text{ion}} = \eta m_p c^2 Z_b, \quad (20)$$

where $m_p c^2 = 938$ MeV is the rest mass of the proton and η is the efficiency of conversion of the heavy element rest mass into LyC radiation. For stars with $Z_* = Z_{\odot}/50$ one derives $\eta = 0.014$ (Schaerer 2002; Venkatesan & Truran 2003). An average energy of 22 eV per LyC photon, together with our prediction of $Z_b = 7 \times 10^{-4} Z_{\odot}$ (assuming a solar yield) at redshift 6, imply that around 8 LyC photons per baryon were emitted by early galaxies prior to this epoch. This is a reasonable value since, while one needs at least one photon per baryon for reionization to occur, the effect of hydrogen recombinations in the IGM and within individual halos will likely boost the number of photons required. A global

⁹To obtain this estimate, we have computed photoionization models based on the CLOUDY code (Ferland et al. 1998) assuming the UV radiation background at $z = 6$ of Haardt & Madau (2012) and a range of gas overdensities $0 < \log \delta < 3$.

metallicity at $z = 6$ that was much lower than our predicted value would effectively create a deficit of UV radiation and leave the reionization of the IGM unexplained. In §5.8 below we will link the production of LyC photons to stellar mass, show that the efficiency of LyC production decreases with increasing Z_* , and discuss early star formation and the epoch of reionization in more details.

5.7 Black Hole Accretion History

Direct dynamical measurements show that most local massive galaxies host a quiescent massive black hole (MBH) in their nuclei. Their masses have been found to correlate tightly with the stellar velocity dispersion of the host stellar bulge, as manifested in the $M_{\text{BH}} - \sigma_*$ relation of spheroids (Ferrarese & Merritt 2000; Gebhardt et al. 2000). It is not yet understood whether such scaling relations were set in primordial structures and maintained throughout cosmic time with a small dispersion, or indeed which physical processes established such correlations in the first place. Nor it is understood whether the energy released during the luminous quasar phase has a global impact on the host, generating large-scale galactic outflows and quenching star formation (Di Matteo et al. 2005) or just modifies gas dynamics in the galactic nucleus (Debuhr et al. 2010).

Here, we consider a different perspective on the link between the assembly of the stellar component of galaxies and the growth of their central black holes. The cosmic mass accretion history of MBHs can be inferred using Soltan’s argument (Soltan 1982), which relates the quasar bolometric luminosity density to the rate at which mass accumulates into black holes,

$$\dot{\rho}_{\text{BH}}(z) = \frac{1 - \epsilon}{\epsilon c^2} \int L \phi(L, z) dL, \quad (21)$$

where ϵ is the efficiency of conversion of rest-mass energy into radiation. In practice, bolometric luminosities are typically derived from observations of the AGN emission at X-ray, optical or infrared wavelengths, scaled by a bolometric correction. Figure 15 compares several recent determinations of the MBH mass growth rate to the cosmic star formation rate density (eq. 15). The light green shaded region shows the accretion history derived from the hard X-ray LF (HXLF) of Aird et al. (2010), assuming a radiative efficiency $\epsilon = 0.1$ and a constant bolometric correction of 40 for the observed 2-10 KeV X-ray luminosities. This accretion rate peaks at lower redshift than does the SFRD, and declines more rapidly from $z \approx 1$ to 0. However, a number of authors have discussed the need for luminosity-dependent bolometric corrections, which in turn can affect the derived accretion history (e.g., Marconi et al. 2004; Hopkins et al. 2007; Shankar et al. 2009). Moreover, while the HXLF includes unobscured as well as moderately obscured sources that may not be identified as AGN at optical wavelengths, it can miss Compton thick AGN, which may be identified in other ways, particularly using infrared data. Delvecchio et al. (2014) have used deep *Herschel* and *Spitzer* survey data in GOODS-S and COSMOS to identify AGN by SED fitting. This is a potentially powerful method, but depends on reliable decomposition of the infrared emission from AGN and star formation.

Black hole mass growth rates derived from the bolometric AGN luminosity functions of Shankar et al. (2009) and Delvecchio et al. (2014) are also shown in Figure 15. These more closely track the cosmic star-formation history, peaking at $z \approx 2$, and suggest that star formation and black hole growth are closely linked at all redshifts, as found by previous authors (Boyle & Terlevich 1998; Silverman et al. 2008). However, the differences between accretion histories published in the recent literature would caution that it is premature to

consider this comparison to be definitive.

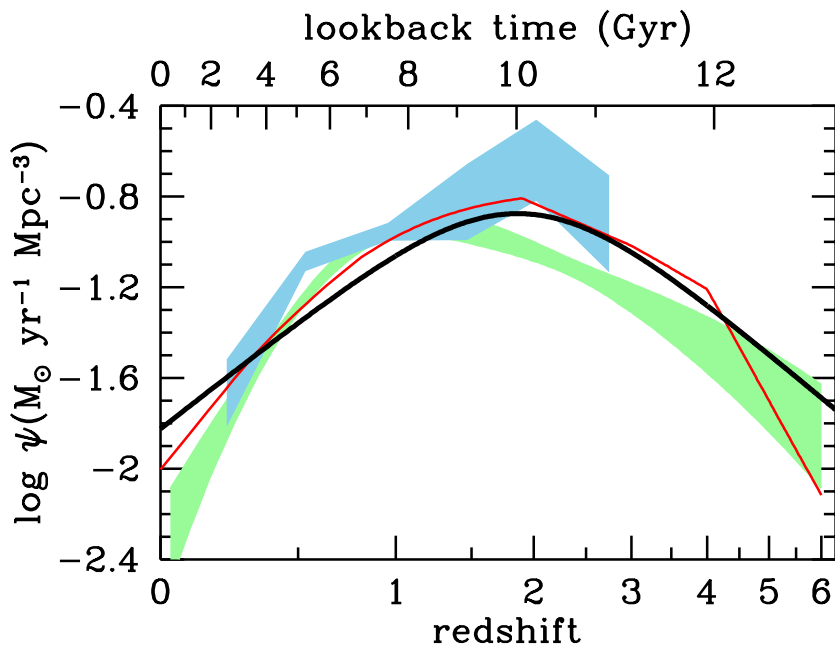


Figure 15: Comparison of the best-fit star formation history (*thick solid curve*) with the massive black hole accretion history from X-ray (Shankar et al. 2009, *red curve*; Aird et al. 2010, *light green shading*) and infrared (Delvecchio et al. 2014, *light blue shading*) data. The shading indicates the $\pm 1\sigma$ uncertainty range on the total bolometric luminosity density. The radiative efficiency has been set to the value $\epsilon = 0.1$. The comoving rates of black hole accretion have been scaled up by a factor of 3,300 to facilitate visual comparison to the star formation history.

5.8 First Light and Cosmic Reionization

Fundamental to our understanding of how the universe evolved to its present state is the epoch of “first light”, the first billion years after the Big Bang when the collapse of the earliest baryonic objects – the elementary building blocks for the more massive systems that formed later – determined the “initial conditions” of the cosmological structure formation process. The reionization in the all-pervading IGM – the transformation of neutral hydrogen into an ionized state – is a landmark event in the history of the early universe. Studies of Ly α absorption in the spectra of distant quasars show that the IGM is highly photoionized out to redshift $z \gtrsim 6$ (see Fan et al. 2006 for a review), while polarization data from the *Wilkinson Microwave Anisotropy Probe (WMAP)* constrain the redshift of any sudden reionization event to be significantly higher, $z = 10.5 \pm 1.2$ (Jarosik et al. 2011). It is generally thought that the IGM is kept ionized by the integrated UV emission from AGN and star-forming galaxies, but the relative contributions of these sources as a function of epoch are poorly known (e.g., Madau et al. 1999; Faucher-Giguère et al. 2008; Haardt & Madau 2012; Robertson et al. 2013).

Establishing whether massive stars in young star-forming galaxies were responsible for

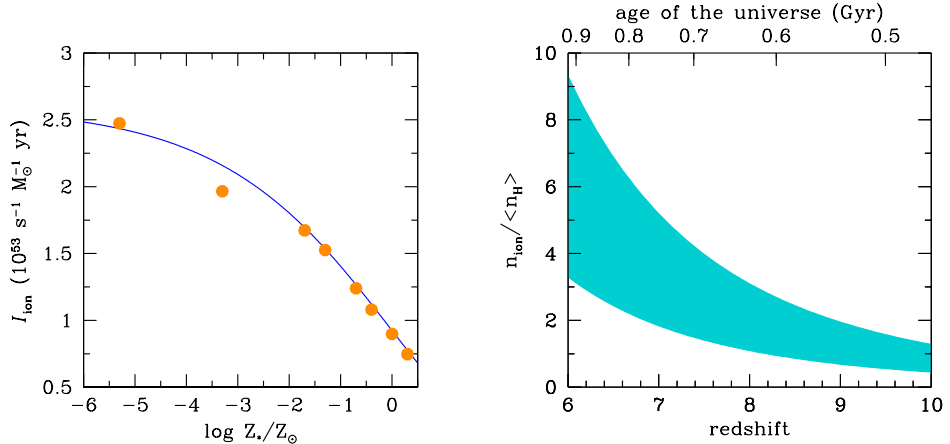


Figure 16: *Left panel:* Metallicity dependence of the ionizing photon yield, I_{ion} , for a stellar population with a Salpeter IMF and constant SFR. The points show the values given in Table 4 of Schaerer (2003), computed for a Salpeter IMF in the 1-100 M_{\odot} range, and divided by a mass conversion factor of 2.55 to rescale to a mass range 0.1-100 M_{\odot} . The solid curve shows the best-fitting function, $\log I_{\text{ion}} = [(0.00038Z_*^{0.227} + 0.01858)]^{-1} - \log(2.55)$. *Right panel:* Number of H-ionizing photons emitted per hydrogen atom since the Big Bang, $n_{\text{ion}}/\langle n_{\text{H}} \rangle$, according to our best-fit star formation history. The shaded area is delimited by stellar populations with metallicities $Z_* = Z_{\odot}$ (lower boundary) and $Z_* = 0$ (upper boundary).

cosmic reionization requires a determination of the early history of star formation, of the LyC flux emitted by a stellar population, and of the fraction of hydrogen-ionizing photons that are able to escape from the dense sites of star formation into the low-density IGM. We can again use stellar population synthesis to estimate the comoving volumetric rate at which photons above 1 Ryd are emitted from star-forming galaxies as

$$\dot{n}_{\text{ion}} = I_{\text{ion}} \times \psi(t), \quad (22)$$

where \dot{n}_{ion} is expressed in units of $\text{s}^{-1} \text{Mpc}^{-3}$ and ψ in units of $M_{\odot} \text{yr}^{-1} \text{Mpc}^{-3}$. The LyC photon yield I_{ion} is plotted in Figure 16 (left panel) for our reference Salpeter IMF and for a wide range of metallicities, spanning from extremely metal poor to metal-rich stars (Schaerer 2003). The yield increases with decreasing metallicity by more than a factor of three. Integrating equation (22) over time, and dividing by the mean comoving hydrogen density $\langle n_{\text{H}} \rangle = 1.9 \times 10^{-7} \text{cm}^{-3}$, we can write the total number of stellar LyC photons emitted per hydrogen atom since the Big Bang as

$$\mathcal{N}_{\text{ion}}(z) \equiv \frac{n_{\text{ion}}}{\langle n_{\text{H}} \rangle} = I_{\text{ion}} \times 7.8 \times 10^{-60} \times \rho_*(z), \quad (23)$$

where $\rho_*(z)$ is the cosmic stellar mass density.¹⁰ The right panel of Figure 16 depicts the quantity \mathcal{N}_{ion} at $z > 6$ according to our best-fit SFH, for the range of stellar metallicities

¹⁰Note that, while in the case of purely stellar radiation what matters for reionization is the total *number* of ionizing photons produced, in the case of energetic X-ray photons what counts is the total radiated *energy*. This is because, in a largely neutral medium, each photoionization produces a host of secondary collisional ionizations, with about one hydrogen secondary ionization for every 37 eV of energy in the primary photoelectron (Shull & van Steenberg 1985). As the medium becomes more ionized, however, an increasing fraction of this energy is deposited as heat.

$0 < Z_* < Z_\odot$. Cosmological reionization requires at least one LyC photon per hydrogen atom *escaping* into the intergalactic space, i.e., $\mathcal{N}_{\text{ion}}\langle f_{\text{esc}} \rangle > 1$, the exact number depending on the rate of radiative recombinations in a clumpy IGM. Here, the escape fraction $\langle f_{\text{esc}} \rangle$ is the angle-averaged, absorption cross section-weighted, and luminosity-weighted fraction of ionizing photons that leaks into the IGM from the dense star-forming regions within galaxies.

The figure shows the well-known result that, even if the emission of LyC photons at early cosmic times was dominated by extremely low-metallicity stars, escape fractions in excess of 20 per cent would be required in order to reionize the universe by redshift 6-7 (e.g., Bolton & Haehnelt 2007; Ouchi et al. 2009; Bunker et al. 2010; Haardt & Madau 2012; Finkelstein et al. 2012b). While the mechanisms regulating the escape fraction of ionizing radiation from galaxies and its dependence on cosmic time and luminosity are unknown, these leakage values are higher than typically inferred from observations of LBGs at $z \sim 3$ (e.g., Nestor et al. 2013; Vanzella et al. 2012, and references therein).

The “reionization budget” is made even tighter by two facts. First, the volume-averaged hydrogen recombination timescale in the IGM,

$$\langle t_{\text{rec}} \rangle = (\chi \langle n_{\text{H}} \rangle \alpha_B C_{\text{IGM}})^{-1} \simeq 3.2 \text{ Gyr} \left(\frac{1+z}{7} \right)^{-3} C_{\text{IGM}}^{-1}, \quad (24)$$

is about 60% of the expansion timescale $H^{-1} = H_0^{-1}[\Omega_M(1+z)^3 + \Omega_\Lambda]^{-1/2}$ at $z = 10$, i.e., close to two ionizing photon per baryon are actually needed to keep the IGM ionized. Here α_B is the recombination coefficient to the excited states of hydrogen, $\chi = 1.08$ accounts for the presence of photoelectrons from singly ionized helium, and C_{IGM} is the clumping factor of ionized hydrogen. The above estimate assumes a gas temperature of 2×10^4 K and a clumping factor for the intergalactic medium, $C_{\text{IGM}} = 1 + 43 z^{-1.71}$, that is equal to the clumpiness of gas below a threshold overdensity of 100 found at $z \geq 6$ in a suite of cosmological hydrodynamical simulations (Pawlik et al. 2009; see also Shull et al. 2012). Second, the rest-frame UV continuum properties of very high redshift galaxies appear to show little evidence for the “exotic” stellar populations (e.g., extremely sub-solar metallicities or top-heavy initial mass functions) that would significantly boost the LyC photon yield (e.g., Finkelstein et al. 2012a; Dunlop et al. 2013).

We conclude by noting that, while improved knowledge of the SFRD beyond redshift 9 may help in better characterizing this photon shortfall, the prospects of a direct observational determination of the escape fraction of ionizing photons leaking into the IGM at these early epochs look rather bleak, as the universe becomes opaque to LyC radiation above redshift 4.

6 CONCLUDING REMARKS

The cosmic history of star formation is one of the most fundamental observables in astrophysical cosmology. We have reviewed the range of complementary techniques and theoretical tools that are allowing astronomers to map the transformation of gas into stars, the production of heavy elements, and the reionization of the universe from the cosmic dark ages to the present epoch. Under the simple assumption of a universal IMF, there is reasonable agreement between the global SMD inferred at any particular time and the time integral of all the preceding instantaneous star formation activity, although modest offsets may still point toward systematic uncertainties. A consistent picture is emerging, whereby the SFRD peaked about 3.5 Gyr after the Big Bang, and dropped exponentially

at $z < 1$ with an e-folding timescale of 3.9 Gyr. The universe was a much more active place in the past, with stars being formed at a peak rate about 9 times higher than is seen today. About 25% of the present-day stellar mass density formed at $z > 2$, before the peak of the SFRD, and another 25% formed since $z = 0.7$, i.e., roughly over the last half of the universe’s age. From the peak of the SFRD at $z \approx 2$ to the present day, and perhaps earlier as well, most stars formed in galaxies that obey a relatively tight SFR– M_* correlation, and only a small fraction formed in starbursts with significantly elevated specific star formation rates. The smooth evolution of this dominant main sequence galaxy population suggests that the evolution of the cosmic star formation history is primarily determined by a balance between gas accretion and feedback processes, both closely related to galaxy mass, and that stochastic events such as merger-driven starbursts play a relatively minor role. The growth histories of the stellar component of galaxies and their central black holes are similar in shape, suggesting broad co-evolution of black holes and their host galaxies. The rise of the mean metallicity of the universe to 0.001 solar by redshift six, one Gyr after the Big Bang, appears to have been accompanied by the production of fewer than ten hydrogen Lyman-continuum photons per baryon, indicating a rather tight budget for cosmological reionization. The star formation rate density at $z \approx 7$ was about the same as that today, at $z \approx 0$, but only 1% of today’s stellar mass density was formed during the epoch of reionization.

As far as the observations and data are concerned, there is still room for improvement in both SFRD and SMD measurements at virtually every redshift, from the local universe to the epoch of reionization (§4.6). That said, it would be somewhat surprising if new *measurements* changed the picture dramatically at $z < 1$; it is more likely that stellar population modeling, e.g., for deriving stellar masses or star formation rates, could still change the details of the picture during the decline and fall of the cosmic star formation history. Indeed, at all redshifts, limitations of our methods for interpreting light as mass may play a significant, even dominant, role in the error budget for the analyses described in this review. The peak era of cosmic star formation has been extensively mapped, and yet even with the current data (Fig. 9) it is still hard to accurately pinpoint the redshift of maximum SFRD within a range $\Delta z = 1$. Our fitting function (eq. 15) places this peak at $z \approx 1.85$, which is plausible but still uncertain. Uncertainties in the faint end slope of the IR luminosity function, and in extinction corrections for the UV luminosity function, still dominate at this peak era of cosmic star formation. While the evidence seems to point clearly to a steady increase in the SFRD from $z = 8$ to $z \approx 2$, our direct knowledge of dust-obscured star formation at these redshifts is, for the most part, limited to the rarest and most ultraluminous galaxies, leaving considerable uncertainty about how much SFRD we may be missing in the UV census of that early phase of galaxy evolution. At $z > 4$, our galaxy surveys have been strongly biased toward UV-bright galaxies, and may underestimate both star formation rate and stellar mass densities. Even for UV-selected galaxies, the measurements at $z \geq 8$ are very new and likely uncertain, unsupported by spectroscopic confirmation to date. In addition to measuring redshifts, spectroscopy from the *JWST* will help clarify basic issues about nebular line emission and the degree to which it has affected the photometric analyses that have been carried out to date.

Painstaking though all this vast effort has been, it does miss a crucial point. It says little about the inner workings of galaxies, their “metabolism” and the basic process of ingestion (gas infall and cooling), digestion (star formation), and excretion (outflows), and ultimately about the mapping from dark matter halos to their baryonic components. Its roots are in optical/IR astronomy, statistics, stellar populations, and phenomenology, rather than in

the physics of the ISM, self-regulated accretion and star formation, stellar feedback, and SN-driven galactic winds. It provides a benchmark against which to compare semi-analytic modeling and hydrodynamical simulations of galaxy formation, but offers little guidance in identifying the smaller-scale basic mechanisms that determine the rate of conversion of gas into stars and lead to the grandiose events in the history of the universe described in this review.

While a variety of physical processes are thought to shape the observed distribution of galaxy properties, from those responsible for galaxy growth, such as star formation and galaxy merging, to those that regulate such growth, such as energetic feedback from SNe, AGN, and the UV radiation background, it is expected that many of these processes depend primarily on the mass of a galaxy’s dark matter halo. Relating the stellar masses and SFRs of galaxies to the masses and assembly histories of their parent halos is then a crucial piece of the galaxy formation and evolution puzzle. With the accumulation of data from large surveys and from cosmological numerical simulations, several statistical methods have been developed over the past decade to link galaxies properties to the underlying dark matter structures (e.g. Berlind & Weinberg 2002; Yang et al. 2003; Vale & Ostriker 2004). One of them, the “abundance matching” technique, assumes in its simplest form a unique and monotonic relation between galaxy light and halo mass, and has been shown to reproduce galaxy clustering as a function of luminosity over a wide range in redshift (e.g. Conroy et al. 2006; Guo et al. 2010; Moster et al. 2010). Modern versions of this approach (Moster et al. 2013; Behroozi et al. 2013) have shown that: 1) halos of mass $\sim 10^{12} M_{\odot}$ are the most efficient at forming stars at every epoch, with baryon conversion efficiencies of 20-40% that fall rapidly at both higher and lower masses; 2) in halos similar to that of the Milky Way, about half of the central stellar mass is assembled after redshift 0.7; and 3) in low-mass halos, the accretion of satellites contributes little to the assembly of their central galaxies, while in massive halos more than half of the central stellar mass is formed “ex-situ”. These studies represent promising advances, albeit with serious potential shortcomings (e.g. Guo & White 2013; Zentner et al. 2013). The assumption of a monotonic relation between stellar mass and the mass of the host halo is likely incorrect in detail, and it will only predict numerically converged properties on scales that are well resolved in the simulations. The matching procedure requires minimal assumptions and avoids an explicit treatment of the physics of galaxy formation. As such, of course, it provides relatively little new insight into this physics. In the version of this technique by Behroozi et al. (2013), for example, the cosmic star formation history is reproduced by construction.

As of this writing, a solid interpretation of the cosmic history of star formation from first principles is still missing (see Mac Low 2013 for a recent review). Generically, one expects that star formation may be limited at early times by the build-up of dark matter halos, and quenched at low redshift as densities decline from Hubble expansion to the point where gas cooling is inhibited. These two regimes could then lead to a peak in the SFH at intermediate redshifts (Hernquist & Springel 2003). A decade ago, hydrodynamical simulations predicted that the peak in star formation activity should occur at a much higher redshift, $z \gtrsim 5$, than is actually observed (Springel & Hernquist 2003; Nagamine et al. 2004). Theoretical modeling has been unable to correctly forecast the evolution of the SFRD because of the large range of galaxy masses that contribute significantly to cosmic star formation and the difficulty in following the feedback of energy into the interstellar and circumgalactic medium from stellar radiation, supernova explosions, and accreting massive black holes. Gas cooling in an expanding universe is an intrinsically unstable process because cooling acts to increase the density of the gas, which in turn increases the cooling rate. Systems collapsing at low

redshift have low mean densities and long cooling times, while systems collapsing at higher redshifts have higher mean densities and thus cool catastrophically. It is well known that, without feedback processes that transfer energy to the interstellar medium and reheat it, one is faced with the classical overcooling problem – the unphysical cooling of hot gas in the poorly resolved inner regions of galaxies – and with the consequent overproduction of stars at early times. And yet a completely satisfactory treatment of feedback in hydrodynamical simulations that capture large cosmological volumes remains elusive, as these mechanisms operate on scales too small to be resolved and must therefore be incorporated via ad-hoc recipes that are too simplistic to capture the complex subgrid physics involved (e.g., Schaye et al. 2009).

An in-depth knowledge of the mechanisms responsible for suppressing star formation in small halos (e.g., Governato et al. 2010; Krumholz & Dekel 2012; Kuhlen et al. 2012), more powerful supercomputers, better algorithms as well as more robust numerical implementations of stellar feedback (e.g., Agertz et al. 2013) all appear at this stage as crucial prerequisites for predicting more realistic star formation histories. Newer and deeper observations from the ground and space should improve our measurements of the galaxy population and its integrated properties, especially at and beyond the current redshift frontier where data is still sparse. It seems likely, however, that the most important contribution of new surveys and better modeling will be toward a detailed understanding of the physics of galaxy evolution, not simply its demographics.

7 DISCLOSURE STATEMENT

The authors are not aware of any affiliations, memberships, funding, or financial holdings that might be perceived as affecting the objectivity of this review.

8 ACKNOWLEDGMENTS

This review has benefited from many discussions with and the help of J. Aird, R. Chary, C. Conroy, D. Elbaz, H. Ferguson, A. Gallazzi, V. González, A. Klypin, K.-S. Lee, D. Maoz, P. Oesch, M. Pettini, J. Pforr, L. Pozzetti, J. Primack, J. X. Prochaska, M. Rafelski, A. Renzini, B. Robertson, and M. Schenker. Support for this work was provided by the NSF through grant OIA-1124453 and NASA through grant NNX12AF87G (P.M.), and by NOAO, which is operated by the Association of Universities for Research in Astronomy, under a cooperative agreement with the NSF (M.D.).

LITERATURE CITED

- Adelberger KL, Steidel CC, Shapley AE, et al. 2004. *Ap. J.* 607:226
 Agertz O, Kravtsov AV, Leitner, SN, Gnedin NY 2013. *Ap. J.* 770:25
 Aguirre A, Dow-Hygelund C, Schaye J, Theuns T 2008. *Ap. J.* 689:851
 Aird J, Nandra K, Laird ES, et al. 2010. *MNRAS* 401:2531
 Alavi A, Siana B, Richard J, et al. 2013. *Ap. J.* in press (arXiv:1305.2413)
 Appleton PN, Fadda DT, Marleau FR, et al. 2004. *Ap. J. Suppl.* 154:147
 Arnouts S, Schiminovich D, Ilbert O, et al. 2005. *Ap. J. Let.* 619:L43
 Arnouts S, Walcher CJ, Le Fevre O, et al. 2007. *Astron. Astrophys.* 476:137
 Ashby MLN, WillnerSP, Fazio GG, et al. 2013. *Ap. J.* 679:80
 Asplund M, Grevesse N, Sauval AJ, Scott P 2009. *Annu. Rev. Astron. Astrophys.* 47:481
 Atek H, Malkan M, McCarthy P 2010. *Ap. J.* 723:104

Aussel H, Cesarsky CJ, Elbaz D, Stark JL 1999. *Astron. Astrophys.* 342:313
 Babbedge TSR, Rowan-Robinson M, Vaccari M, et al. 2006. *MNRAS* 370:1159
 Baldry IK, Driver SP, Loveday J, et al. 2012. *MNRAS* 421:621
 Baldry IK, Glazebrook K 2003. *Ap. J.* 593:258
 Baldry IK, Glazebrook K, Driver SP 2008. *MNRAS* 388:945
 Balestra I, Tozzi P, Ettori S, et al. 2007. *Astron. Astrophys.* 462:429
 Barger A, Cowie LL, Richards EA 2000. *Astron. J.* 119:2092
 Barger A, Cowie LL, Sanders DB, et al. 1998. *Nature* 394:248
 Barger A, Cowie LL, Wold IGB 2012. *Ap. J.* 749:106
 Bastian N, Covey KR, Meyer MR 2010. *Annu. Rev. Astron. Astrophys.* 48:339
 Basu-Zych AR, Lehmer BD, Hornschemeier AE, et al. 2013. *Ap. J.* 762:45
 Bazin G, Palanque-Delabrouille N, Rich J, et al. 2009. *Astron. Astrophys.* 499:653
 Becker GD, Sargent WLW, Rauch M, Calverley AP 2011. *Ap. J.* 735:93
 Beckwith SVW, Stiavelli M, Koekemoer AM, et al. 2006. *Astron. J.* 132:1729
 Behroozi PS, Wechsler RH, Conroy C 2013. *Ap. J.* 770:57
 Bell EF, MacIntosh DH, Katz N, Weinberg MD 2003. *Ap. J. Suppl.* 149:289
 Berlind AA, Weinberg DH 2002. *Ap. J.* 575:587
 Berta S, Magnelli B, Nordon R, et al. 2011. *Astron. Astrophys.* 532:A49
 Béthermin M, Le Floc'h E, Olbert O, et al. 2012. *Astron. Astrophys.* 542:A57
 Bielby R, Hudelot P, McCracken HJ, et al. 2012. *Astron. Astrophys.* 545:23
 Blumenthal GR, Faber SM, Primack JR, Rees MJ 1984. *Nature* 311:517
 Bolton, JS, Haehnelt MG 2007. *MNRAS* 382:325
 Botticella MT, Riello M, Cappellaro E, et al. 2008. *Astron. Astrophys.* 479:49
 Bouwens RJ, Illingworth GD, Franx M, Ford H 2007. *Ap. J.* 670:928
 Bouwens RJ, Illingworth GD, Labbé I, et al. 2011a. *Nature* 469:504
 Bouwens RJ, Illingworth GD, Oesch PA, et al. 2011b. *Ap. J.* 737:90
 Bouwens RJ, Illingworth GD, Oesch PA, et al. 2012a. *Ap. J.* 754:83
 Bouwens RJ, Illingworth GD, Oesch PA, et al. 2012b. *Ap. J. Let.* 752:L5
 Bowler RAA, Dunlop JS, McLure RJ, et al. 2012. *MNRAS* 426:2772
 Boyle BJ, Terlevich RJ 1998. *MNRAS* 293:L49
 Brammer GB, van Dokkum PG, Franx M, et al. 2012. *Ap. J. Suppl.* 200:13
 Brammer GB, Whitaker KE, van Dokkum PG, et al. 2011. *Ap. J.* 739:24
 Brandt WN, Hasinger G. 2005. *Annu. Rev. Astron. Astrophys.* 43:827
 Brinchmann J, Charlot S, White SDM, et al. 2004. *MNRAS* 351:1151
 Brinchmann J, Ellis RS 2000. *Ap. J. Let.* 536:L77
 Bruzual G, Charlot S 2003. *MNRAS* 344:1000
 Bruzual G, Charlot S, González Lópezlira R, et al. 2013 in *The Intriguing Life of Massive Galaxies*,
 Proceedings of the International Astronomical Union, 295:435
 Buat V, Iglesias-Páramo J, Seibert M, et al. 2005. *Ap. J. Let.* 619:L51
 Buat V, Noll S, Burgarella D, et al. 2012. *Astron. Astrophys.* 545:A141
 Budavári T, Szalay AS, Charlot S, et al. 2005. *Ap. J. Let.* 619:L31
 Bunker AJ, Wilkins S, Ellis RS, et al. 2010. *MNRAS* 409:855
 Burgarella D, Buat V, Gruppioni C, et al. 2013. *Astron. Astrophys.* 554:A70
 Calzetti D 2001. *Pub. Astron. Soc. Pac.* 113:1449
 Calzetti D, Armus L, Bohlin RC, et al. 2000. *Ap. J.* 533:682
 Calzetti D, Kennicutt RC, Engelbracht CW, et al. 2007. *Ap. J.* 666:870
 Calzetti D, Kinney AL, Storchi-Bergmann T 1994. *Ap. J.* 429:582
 Caputi KI, Cirasuolo M, Dunlop JS, et al. 2011. *MNRAS* 413:162
 Caputi KI, Dunlop JS, McLure RJ, et al. 2012. *Ap. J.* 750:20
 Caputi KI, Lagache G, Yan L, et al. 2007. *Ap. J.* 660:97
 Carilli CL, Lee N, Capak P, et al. 2008. *Ap. J.* 689:883
 Castellano M, Fontana A, Boutsia K, et al. 2010a. *Astron. Astrophys.* 511:A20

Castellano M, Fontana A, Paris D, et al. 2010b. *Astron. Astrophys.* 524:A28
 Chabrier G 2003. *Pub. Astron. Soc. Pac.* 115:763
 Chapman SC, Blain AW, Smail I, Ivison RJ 2005. *Ap. J.* 622:772
 Charlot S, Fall SM 2000. *Ap. J.* 539:718
 Chary R-R, & Elbaz, D 2001. *Ap. J.* 556:562
 Chary R-R, Stern D, Eisenhardt P 2005. *Ap. J. Let.* 635:L5
 Chieffi A, Limongi M 2004. *Ap. J.* 608:405
 Coe D, Zitrin A, Carrasco M, et al. 2013. *Ap. J.* 762:32
 Cohen JG 2002. *Ap. J.* 567:672
 Cole S, Lacey CG, Baugh CM, Frenk CS 2000. *MNRAS* 319:168
 Cole S, Nordberg P, Baugh CM, et al. 2001. *MNRAS* 326:255
 Colless M, Dalton G, Maddox S, et al. 2001. *MNRAS* 328:1039
 Condon JJ 1992. *Annu. Rev. Astron. Astrophys.* 30:575
 Condon JJ, Cotton WD, Broderick JJ 2002. *Astron. J.* 124:675
 Connolly AJ, Szalay AS, Dickinson M, Subbarao MU, Brunner RJ 1997. *Ap. J. Let.* 486:L11
 Conroy C 2013. *Annu. Rev. Astron. Astrophys.* 51:393
 Conroy C, Gunn JE, White M 2009. *Ap. J.* 699:486
 Conroy C, van Dokkum PG 2012. *Ap. J.* 760:71
 Conroy C, Wechsler RH, Kravtsov AV 2006. *Ap. J.* 647:201
 Conselice CJ, Bluck AF, Buitrago F, et al. 2011. *MNRAS* 413:80
 Cowie LL, Songaila A, & Barger AJ 1999. *Astron. J.* 118:603
 Cowie LL, Songaila A, Hu EM, Cohen JG 1996. *Astron. J.* 112:839
 Cucciati O, Tresse L, Ilbert O, et al. 2012. *Astron. Astrophys.* 539:31
 Curtis-Lake E, McLure RJ, Dunlop JS, et al. 2013. *MNRAS* 429:302
 Daddi E, Cimatti A, Renzini A, et al. 2004. *Ap. J.* 617:746
 Daddi E, Dannerbauer H, Krips M, et al. 2009. *Ap. J. Let.* 695:L176
 Daddi E, Dickinson M, Chary R, et al. 2005. *Ap. J. Let.* 631:L13.
 Daddi E, Dickinson M, Morrison G, et al. 2007b. *Ap. J.* 670:156
 Dahlen T, Mobasher B, Dickinson M, et al. 2007. *Ap. J.* 654:172
 Dahlen T, Strolger L-G, Riess AG, et al. 2012. *Ap. J.* 757:70
 Dale DA, Bendo GJ, Engelbracht CW, et al. 2005. *Ap. J.* 633:857
 Dale DA, Helou G 2002. *Ap. J.* 576:159
 Damen M, Labbé I, Franx M, et al. 2009. *Ap. J.* 690:937
 Davis M, Efstathiou G, Frenk CS, White SDM 1985. *Ap. J.* 292:371
 Debuhr J, Quataert E, Ma C-P, Hopkins P 2010. *MNRAS* 406:L55
 Delvecchio I, Gruppioni C., Pozzi F, et al. 2014. *MNRAS* in press (arXiv:1401.4503)
 Dey A, Soifer BT, Desai V, et al. 2008. *Ap. J.* 677:943
 Dickinson M, Papovich C, Ferguson HC, Budavári T 2003. *Ap. J.* 587:25
 Dickinson M, Stern D, Giavalisco M, et al. 2004. *Ap. J. Let.* 600:L99
 Diemand J, Kuhlen M, Madau P, et al. 2008. *Nature* 454:735
 Di Matteo T, Springel V, Hernquist L 2005. *Nature* 433:604
 Doherty M, Bunker A, Sharp R, et al. 2006. *MNRAS* 370:331
 Driver SP, Popescu CC, Tuffs RJ, et al. 2008. *Ap. J. Let.* 678:L101
 Dubinski J, Carlberg RG 1991. *Ap. J.* 378:496
 Dunlop JS, Rogers AB, McLure RJ, et al. 2013. *MNRAS* 432:3520
 Dunne L, Eales S, Edmunds M, et al. 2000. *MNRAS* 315:115
 Dunne L, Ivison RJ, Maddox S, et al. 2009. *MNRAS* 394:3
 Dyle S, Dunne L, Eales S, et al. 2010. *Astron. Astrophys.* 518:L10
 Eales SA, Raymond G, Roseboom IG, et al. 2010. *Astron. Astrophys.* 518:L23
 Elbaz D, Daddi E, Le Borgne D, et al. 2007. *Astron. Astrophys.* 468:33
 Elbaz D, Dickinson M, Hwang HS, et al. 2011. *Astron. Astrophys.* 533:119
 Elbaz D, Hwang HS, Magnelli B, et al. 2010. *Astron. Astrophys.* 518:L29

Ellis RS, McLure RJ, Dunlop JS, et al. 2013. *Ap. J. Let.* 763:L7
 Engelbracht CW, Gordon KD, Rieke GH, et al. 2005. *Ap. J. Let.* 628:L29
 Engelbracht CW, Rieke GH, Gordon KD, et al. 2008. *Ap. J.* 678:804
 Eyles LP, Bunker AJ, Ellis RS, et al. 2007. *MNRAS* 374:910
 Faber SM, Willmer CNA, Wolf C, et al. 2007. *Ap. J.* 665:265
 Fan X, Carilli CL, Keating B 2006. *Annu. Rev. Astron. Astrophys.* 44:415
 Faucher-Giguère C-A, Prochaska JX, Lidz A, Hernquist L, Zaldarriaga M 2008. *Ap. J.* 681:831
 Ferland GJ, Korista KT, Verner DA, et al. 1998. *Pub. Astron. Soc. Pac.* 110:761
 Ferrarese L, Merritt D 2000. *Ap. J. Let.* 539:L9
 Finkelstein SL, Papovich C, Dickinson M, et al. 2013. *Nature* 502: 524
 Finkelstein SL, Papovich C, Ryan RE, et al. 2012a. *Ap. J.* 758:93
 Finkelstein SL, Papovich C, Salmon B, et al. 2012b. *Ap. J.* 756:164
 Flores H, Hammaer F, Thuan TX, et al. 1999. *Ap. J.* 517:148
 Fontana A, Donnarumma I, Vanzella E, et al. 2003. *Ap. J. Let.* 594:L9
 Fontana A, Salimbeni S, Grazian A, et al. 2006. *Astron. Astrophys.* 459:745
 Franceschini A, Andreani P, Danese L 1998. *MNRAS* 296:709
 Franx M, Labbé I, Rudnick G, et al. 2003. *Ap. J. Let.* 587:L79
 Fukugita M, Hogan CJ, Peebles PJE 1998. *Ap. J.* 503:518
 Gallazzi A, Brinchmann J, Charlot S, White SDM 2008, *MNRAS* 383:1439
 Galleo J, Zamorano J, Aragon-Salamanca A, Rego M 1995. *Ap. J. Let.* 455:L1
 Gal-Yam A, Ofek EO, Poznanski D, et al. 2006. *Ap. J.* 639:331
 Gavazzi G, Pierini D, Boselli A 1996. *Astron. Astrophys.* 312:397
 Gebhardt K, Bender R, Bower G, et al. 2000. *Ap. J. Let.* 539:L13
 Geha M, Brown TM, Tumlinson J, et al. 2013. *Ap. J.* 771:29
 Giavalisco M, Dickinson M, Ferguson HC, et al. 2004a. *Ap. J. Let.* 600:L103
 Giavalisco M, Ferguson HC, Koekemoer, et al. 2004b. *Ap. J. Let.* 600:L93
 Gispert R, Lagache G, Puget JL 2000. *Astron. Astrophys.* 360:1
 Glazebrook K, Blake C, Economou F, Lilly S, Colless M 1999. *MNRAS* 306:843
 Goldader JD, Meurer G, Heckman TM, et al. 2002. *Ap. J.* 568:651
 González V, Bouwens R, Illingworth G, et al. 2012. *Ap. J.* submitted (arXiv1208.4362)
 González V, Labbé I, Bouwens RJ, et al. 2011. *Ap. J. Let.* 735:L34
 Goto T, Arnouts S, Inami H, et al. 2011a. *MNRAS* 410:573
 Goto T, Arnouts S, Malkan M, et al. 2011b *MNRAS* 414:1903
 Governato F, Brook C, Mayer L, et al. 2010. *Nature* 463:203
 Grazian A, Cstellano M, Koekemoer AM, et al. 2011. *Astron. Astrophys.* 532:33
 Grogin NA, Kocevski DD, Faber SM, Ferguson HC, et al. 2011. *Ap. J. Suppl.* 197:35
 Gruppioni C, Pozzi F, Andreani P, et al. 2010. *Astron. Astrophys.* 518:L27
 Gruppioni C, Pozzi F, Rodighiero G, et al. 2013. *MNRAS* 432:23
 Guedes J, Callegari S, Madau P, Mayer L 2011. *Ap. J.* 742:76
 Gunawardhana MLP, Hopkins AM, Bland-Hawthorn J, et al. 2013. *MNRAS* 433:2764
 Guo Q, White S 2013. *MNRAS* 437:3228
 Guo Q, White S, Li C, Boylan-Kolchin M 2010. *MNRAS* 404:1111
 Guzman R, Galleo J, Koo DC, et al. 1997. *Ap. J.* 489:559
 Jarosik N, Bennett CL, Dunkley J, et al. 2011. *Ap. J. Suppl.* 192:14
 Haardt F, Madau P 2012. *Ap. J.* 746:125
 Haarsma DB, Partridge RB, Windhorst RA, Richards EA 2000. *Ap. J.* 544:641
 Hathi NP, Ryan RE, Cohen SH, et al. 2010. *Ap. J.* 720:1708
 Hayes M, Schaerer D, Östlin G 2010. *Astron. Astrophys.* 509:L5
 Hernquist L, Springel V 2003. *MNRAS* 341: 1253
 Hirschi R, Meynet G, Maeder A 2005. *Astron. Astrophys.* 433:1013
 Hogg DW, Cohen JG, Blandford R, Pahre MA 1998. *Ap. J.* 504:622
 Hopkins AM 2004. *Ap. J.* 615:209

Hopkins AM, Beacom JF 2006. *Ap. J.* 651:142
 Hopkins AM, Beacom JF 2008. *Ap. J.* 682:1486
 Hopkins AM, Connolly AJ, Szalay AS 2000. *Astron. J.* 120:2843
 Hopkins PF, Quataert E, Murray N 2012. *MNRAS* 421:3522
 Hopkins PF, Richards GT, Hernquist L 2007. *Ap. J.* 654:731
 Horiuchi S, Beacom JF, Kochanek CS, et al. 2011. *Ap. J.* 738:154
 Hu EM, Kim T-S, Cowie LL, Songaila A, Rauch M 1995. *Astron. J.* 110:1526
 Huang J-S, Zheng XZ, Rigopoulou D, et al. 2011. *Ap. J.* 742:L13
 Hughes DH, Serjeant S, Dunlop J, et al. 1998. *Nature* 394:241
 Huynh MT, Frayer DT, Mobasher M, et al. 2007. *Ap. J. Let.* 667:L9
 Ilbert O, McCracken HJ, Le Fèvre O, et al. 2013. *Astron. Astrophys.* 556:A55
 Ilbert O, Salvato M, Le Floc'h E, et al. 2010. *Ap. J.* 709:644
 Ivison RJ, Alexander DM, Biggs AD, et al. 2010. *MNRAS* 402:245
 Ivison RJ, Magnelli B, Ibar E, et al. 2010. *Astron. Astrophys.* 518:L31
 Iwata I, Ohta K, Tamura N 2007. *MNRAS* 376:1557
 Jarvis M 2012 in *Science from the Next Generation Imaging and Spectroscopic Surveys*, ESO Garching, 15-18 October, 2012
 Juneau S, Glazebrook K, Crampton D, et al. 2005. *Ap. J. Let.* 619:L135
 Kajisawa M, Ichikawa T, Tanaka I, et al. 2009. *Ap. J.* 702:1393
 Karim A, Schinnerer E, Martínez-Sansigre A, et al. 2011. *Ap. J.* 730:61
 Katz N, Weinberg DH, Hernquist L 1996. *Ap. J. Suppl.* 105:19
 Kauffmann G, Heckman TM, White SDM, et al. 2003. *MNRAS* 341:33
 Kauffmann G, White SDM, Guiderdoni B 1993. *MNRAS* 264:201
 Kennicutt RC 1998. *Annu. Rev. Astron. Astrophys.* 36:189
 Kennicutt RC, & Evans NJ 2012. *Annu. Rev. Astron. Astrophys.* 50:531
 Keres D, Katz N, Weinberg DH, Dave R 2005. *MNRAS* 363:2
 Kewley, L., & Kobulnicky, H. A. 2007, in *Island Universes: Structure and Evolution of Disk Galaxies*, ed. R. S. de Jong (Dordrecht: Springer), 435
 Kistler M, Yüksel H, Beacom JF, Hopkins AM, Wyithe JSB 2009. *Ap. J.* 705:104
 Klypin A, Trujillo-Gomez S, Primack J 2011. *Ap. J.* 740:102
 Koekemoer AM, Faber SM, Ferguson, HC 2011. *Ap. J. Suppl.* 197:36
 Kong X, Charlot S, Brinchmann J, Fall SM 2004. *MNRAS* 349:769
 Kroupa P 2001. *MNRAS* 322:231
 Krumholz MR, Dekel A 2012. *Ap. J.* 753:16
 Kuhlen M, Krumholz MR, Madau P, Smith B, Wise J. 2012, *Ap. J.* 749:36
 Labbé I, Oesch PA, Bouwens RJ, et al. 2013. *Ap. J. Let.* 777:L19
 Lagache G, Puget J-L, Dole H 2005. *Annu. Rev. Astron. Astrophys.* 43:727
 Laird ES, Nandra K, Adelberger KL, et al. 2005. *MNRAS* 359:47
 Laird ES, Nandra K, Hobbs A, et al. 2006. *MNRAS* 373:217
 Lanzetta KM, Wolfe AM, Turnshek DA 1995. *Ap. J.* 440:435
 Lapi A, González-Nuevo J, Fan L, et al. 2011. *Ap. J.* 742:24
 Lawrence A, Walker D, Rowan-Robinson M, Leech KJ, Penston MV 1986. *MNRAS* 219:687
 Lee K-S, Ferguson HC, Wiklind T, et al. 2012. *Ap. J.* 752:66
 Le Floc'h E, Papovich C, Dole H, et al. 2005. *Ap. J.* 632:169
 Lehmer BD, Brandt WN, Alexander DM, et al. 2005. *Astron. J.* 129:1
 Leitherer C, Schaerer D, Goldader JD, et al. 1999. *Ap. J. Suppl.* 123:3
 Li C, White, SDM 2009. *MNRAS* 398:2177
 Li W, Chornock R, Leaman J, et al. 2011. *MNRAS* 412:1473
 Lilly SJ, Le Fèvre O, Hammer F, Crampton D 1996. *Ap. J. Let.* 460:L1
 Lonsdale Persson CJ, & Helou G 1987. *Ap. J.* 314:513
 Lorenzoni S, Bunker AJ, Wilkins SM, et al. 2013. *MNRAS* 429:150
 Lutz D 2014. *Annu. Rev. Astron. Astrophys.* submitted.

Ly C, Lee JC, Dale DA, et al. 2011. *Ap. J.* 726:109
 Ly C, Malkan MA, Kashikawa N et al. 2007. *Ap. J.* 657:738
 Machalski J, Godlowski W 2000. *Astron. Astrophys.* 360:463
 Mac Low M-M 2013. *Science* 340:6140
 Madau P 1995. *Ap. J.* 441:18
 Madau P, Della Valle M, Panagia N 1998. *MNRAS* 297:L17
 Madau P, Ferguson HC, Dickinson ME, et al. 1996. *MNRAS* 283:1388
 Madau P, Haardt F, Rees MJ 1999. *Ap. J.* 514:648
 Madau P, Pozzetti L, Dickinson M 1998. *Ap. J.* 498:106
 Madau P, Shull JM 1996. *Ap. J.* 457:551
 Maeder A 1992. *Astron. Astrophys.* 264:105
 Magdis GE, Elbaz D, Daddi E, et al. 2010. *Ap. J.* 714:1740
 Magnelli B, Elbaz D, Chary RR, et al. 2009. *Astron. Astrophys.* 496:57
 Magnelli B, Elbaz D, Chary RR, et al. 2011. *Astron. Astrophys.* 528:A35
 Magnelli B, Popesso P, Berta S, et al. 2013. *Astron. Astrophys.* 553:A132
 Mancini C, Matute I, Cimatti A, et al. 2009. *Astron. Astrophys.* 500:705
 Mao MY, Huynh MT, Norris RP, et al. 2011. *Ap. J.* 731:79
 Maoz D, Gal-Yam A 2004. *MNRAS* 347:951
 Maraston C 2005. *MNRAS* 362:799
 Maraston C, Daddi E, Renzini A, et al. 2006. *Ap. J.* 652:85
 Maraston C, Pforr J, Renzini A, et al. 2010. *MNRAS* 407:830
 Marchesini D, van Dokkum PG, Forster Schreiber NM, et al. 2009. *Ap. J.* 701:1765
 Marchesini D, Whitaker KE, Brammer G, et al. 2010. *Ap. J.* 725:1277
 Marconi A, Risaliti G, Gilli R, et al. 2004. *MNRAS* 351:169
 Mattila S, Dahlen T, Efstathiou A, et al. 2012. *Ap. J.* 756:111
 Mauch T, Sadler EM 2007. *MNRAS* 375:931
 Mauduit J-C, Lacy M, Farrah D, et al. 2012. *Pub. Astron. Soc. Pac.* 124:714
 McLure RJ, Cirasuolo M, Dunlop JS, et al. 2009. *MNRAS* 395:2196
 McLure RJ, Dunlop JS, Bowler RAA, et al. 2013. *MNRAS* 432:2696
 Meurer GR, Heckman TM, Calzetti D 1999. *Ap. J.* 521:64
 Moore B, Ghigna S, Governato F, et al. 1999. *Ap. J. Let.* 524:L19
 Moster BP, Naab, T, White, SDM 2013. *MNRAS* 428:3121
 Moster BP, Somerville RS, Maulbetsch C, et al. 2010. *Ap. J.* 710:903
 Moustakas J, Coil A, Aird J, et al. 2013. *Ap. J.* 767:50
 Moustakas J, Kennicutt RC, Tremonti CA 2006. *Ap. J.* 642:775
 Murphy EJ, Condon JJ, Schinnerer E, et al. 2011. *Ap. J.* 737:67
 Muzzin A, Marchesini D, Stefanon M, et al. 2013. *Ap. J.* 777:18
 Nagamine K, Cen R, Hernquist L, Ostriker JP, Springel V 2004. *Ap. J.* 610:45
 Navarro JF, Steinmetz M 2000. *Ap. J.* 538:477
 Nestor DB, Shapley AE, Kornei KA, Steidel CC, Siana B 2013. *Ap. J.* 765:47
 Noeske KG, Faber SM, Weiner BJ, et al. 2007. *Ap. J. Let.* 660:L47
 Nonino M, Dickinson M, Rosati P, et al. 2009. *Ap. J. Suppl.* 183:244
 Nordon R, Lutz D, Shao L, et al. 2010. *Astron. Astrophys.* 518:L24
 Ocvirk P, Pichon C, Teyssier R 2008. *MNRAS* 390:1326
 Oesch PA, Bouwens RJ, Carollo CM, et al. 2010. *Ap. J. Let.* 725:L150
 Oesch PA, Bouwens RJ, Illingworth GD, et al. 2012. *Ap. J.* 759:135
 Oesch PA, Bouwens RJ, Illingworth GD, et al. 2013. *Ap. J.* 773:75
 Ouchi M, Mobasher B, Shimasaku K, et al. 2009. *Ap. J.* 706:1136
 Ouchi M, Shimasaku K, Okamura S, et al. 2004. *Ap. J.* 611:660
 Overzier RA, Heckman TM, Wang J, et al. 2011. *Ap. J. Let.* 726:L7
 Panter B, Jimenez R, Heavens AF, Charlot S 2007. *MNRAS* 378:1550
 Papovich C, Dickinson M, & Ferguson HC 2001. *Ap. J.* 559:620

Papovich C, Moustakas LA, Dickinson M, et al. 2006. *Ap. J.* 640:92

Papovich C, Rudnick G, Le Floch E, et al. 2007. *Ap. J.* 668:45

Pawlik AH, Schaye J, van Scherpenzeel E 2009. *MNRAS* 394:4

Patel H, Clements DL, Vaccari M, et al. 2013. *MNRAS* : 428:291

Peebles PJE 1982. *Ap. J. Let.* 263:L1

Pei YC, Fall SM 1995. *Ap. J.* 454:69

Pei YC, Fall SM, Hauser MG 1999. *Ap. J.* 522:604

Penner K, Dickinson M, Pope A, et al. 2012. *Ap. J.* 759:28

Pérez-González PG, Rieke GH, Egami E, et al. 2005. *Ap. J.* 630:82

Pérez-González PG, Rieke GH, Villar V, et al. 2008. *Ap. J.* 675:234

Persic M, Rephaeli Y, Braitto V, et al. 2004. *Astron. Astrophys.* 419:849

Persic M, Salucci P, 1992. *MNRAS* 258:14

Pettini M 2006. In *The Fabulous Destiny of Galaxies: Bridging Past and Present*, eds. V LeBrun, A Mazure, S Arnouts, D Burgarella, pp. 319-335. Paris: Frontiers Group

Pffor J, Maraston C, Tonini C 2012. *MNRAS* 422:3285

Pope A, Bussmann RS, Dey A, et al. 2008. *Ap. J.* 689:127

Porciani C, Madau P 2001. *Ap. J.* 548:522

Portinari L, Moretti A, Chiosi C, Sommer-Larsen J 2004. *Ap. J.* 604:579

Pozzetti L, Bolzonella M, Zucca E, et al. 2010. *Astron. Astrophys.* 523:A13

Rafelski M, Wolfe AM, Prochaska JX, Neeleman M, Mendez AJ 2012. *Ap. J.* 755:89

Raiter A, Fosbury RAE, Teimoorinia H 2010. *Astron. Astrophys.* 510:A109

Ranalli P, Comastri A, Setti G 2003. *Astron. Astrophys.* 399:39

Reddy NA, Erb DK, Pettini M, et al. 2010. *Ap. J.* 712:1070

Reddy NA, Pettini M, Steidel CC, et al. 2012. *Ap. J.* 754:25

Reddy NA, Steidel CC 2004. *Ap. J. Let.* 603:L13

Reddy NA, Steidel CC 2009. *Ap. J.* 692:778

Reddy NA, Steidel CC, Fadda D, et al. 2006. *Ap. J.* 744:792

Reddy NA, Steidel CC, Pettini M, et al. 2008. *Ap. J. Suppl.* 175:48

Retzlaff J, Rosati P, Dickinson M, et al. 2010. *Astron. Astrophys.* 511:A50

Riechers DA, Bradford CM, Clements DL, et al. 2013. *Nature* 496:329

Robertson BE, Ellis RS 2012. *Ap. J.* 744:95

Robertson BE, Furlanetto SR, Schneider E, et al. 2013. *Ap. J.* 768:71

Robotham ASG, Driver SP 2011. *MNRAS* 413:2570

Rodighiero G, Cimatti A, Gruppioni C, et al. 2010. *Astron. Astrophys.* 518:25

Rodighiero G, Daddi E, Baronchelli I, et al. 2011. *Ap. J. Let.* 739:L40

Rowan-Robinson M, Mann RG, Oliver SJ, et al. 1997. *MNRAS* 289:490

Rudnick, G, Rix, H-W, Franx M, et al. 2003, *Ap. J.* 599:847

Rujopakarn W, Eisenstein DJ, Rieke GH, et al. 2010. *Ap. J.* 718:1171

Rush B, Malkan MA, Spinoglio L 1993. *Ap. J. Suppl.* 89:1

Ryan-Weber EV, Pettini M, Madau P, Zych B 2009. *MNRAS* 395:1476

Sadler EM, Jackson CA, Cannon RD 2002. *MNRAS* 329:227

Salim S, Dickinson M, Rich RM, et al. 2009. *Ap. J.* 700:161

Salim S, Rich RM, Charlot S, et al. 2007. *Ap. J. Suppl.* 173:267

Salucci P, Persic M 1999. *MNRAS* 309:923

Salpeter EE 1955. *Ap. J.* 121:161

Sanders DB, Mazzarella JM, Kim DC, Surace JA, Soifer BT 2003. *Astron. J.* 126:1607

Santini, P, Fontana A, Grazian A, et al. 2012. *Astron. Astrophys.* 538:A33

Sargent MT, Béthermin M, Daddi E, Elbaz D 2012. *Ap. J. Let.* 747:L31

Sargent MT, Schinnerer E, Murphy E, et al. 2010a. *Ap. J. Suppl.* 186:341

Sargent MT, Schinnerer E, Murphy E, et al. 2010b. *Ap. J. Let.* 714:L190

Saunders W, Rowan-Robinson M, Lawrence A., et al. 1990. *MNRAS* 242:318

Sawicki M, Yee HKC 1998. *Astron. J.* 115: 1329

Schaerer D 2002. *Astron. Astrophys.* 382:28

Schaerer D 2003. *Astron. Astrophys.* 397:527

Schaller G, Schaerer D, Meynet G, Maeder A 1992. *Astron. Astrophys.* 96:269

Schaye J, Dalla Vecchia C, Booth CM, et al. 2009. *MNRAS*

Schenker MA, Robertson BE, Ellis RS, et al. 2013. *Ap. J.* , 768:196

Schiminovich D, Ilbert O, Arnouts S, et al. 2005. *Ap. J. Let.* 619:L47

Sedgwick C, Serjeant S, Pearson C, et al. 2011, *MNRAS* 416:1862

Serjeant S, Carramiñana A, González-Solares E, et al. 2004. *MNRAS* 355:813

Serjeant S, Gruppioni C, Oliver S 2002. *MNRAS* 330:621

Seymour N, Dwelly T, Moss D, et al. 2008. *MNRAS* 386:1695

Shankar F, Weinberg DH, Miralda-Escude J 2009. *Ap. J.* 690:20

Shapley A, Steidel CC, Adelberger KL 2001. *Ap. J.* 562:95

Shim H, Colbert J, Teplitz H, et al. 2009. *Ap. J.* 696:785

Shim H, Chary RR, Dickinson M, et al. 2011. *Ap. J.* 738:69

Shull JM, Harness A, Trenti M, Smith BD 2012. *Ap. J.* 747:100

Shull JM, van Steenberg ME 1985. *Ap. J.* 298:268

Shupe DL, Fang F, Hacking PB, Huchra JP 1998. *Ap. J.* 501:597

Silverman JD, Green PJ, Barkhouse WA, et al. 2008. *Ap. J.* 679:118

Simcoe RA 2011. *Ap. J.* 738:159

Simcoe RA, Cooksey KL, Matejek M, et al. 2011. *Ap. J.* 743:21

Smail I, Ivison RJ, Blain AW 1997. *Ap. J. Let.* 490:L5

Smith JDT, Draine BT, Dale DA, et al. 2007. *Ap. J.* 656:770

Smolčić V, Schinnerer E, Zamorani G, et al. 2009. *Ap. J.* 690:610

Sobral D, Best PN, Smail I, et al. 2011. *MNRAS* 411:675

Sodriski TJ, Odegard N, Arendt RG, et al. 1997. *Ap. J.* 480:173

Soifer BT, Sanders DB, Madore BF, et al. 1987. *Ap. J.* 320:238

Soltan A 1982. *MNRAS* 200:115

Somerville RS, Primack JR 1999. *MNRAS* 310:1087

Springel V, Hernquist L 2003. *MNRAS* 339:289

Springel V, Wang J, Vogelsberger M, et al. 2008. *MNRAS* 391:1685

Springel V, White SDM, Jenkins A, et al. 2005. *Nature* 435:629

Stadel J, Potter D, Moore B, et al. 2009. *MNRAS* 398:L21

Stanway ER, Bunker AJ, McMahon RG 2003. *MNRAS* 342:439

Stark DP, Bunker A, Ellis RS, et al. 2007. *Ap. J.* 659:84

Stark DP, Ellis RS, Bunker A, et al. 2009. *Ap. J.* 697:1493

Stark DP, Schenker MA, Ellis RS, et al. 2013. *Ap. J.* 763:129

Steidel CC, Adelberger KL, Giavalisco M, Dickinson M, Pettini M 1999. *Ap. J.* 519:1

Steidel CC, Adelberger KL, Shapley AE, Pettini M, Dickinson M 2003. *Ap. J.* 592:728

Steidel CC, Giavalisco, M, Pettini M, Dickinson M, Adelberger, KL 1996. *Ap. J. Let.* 462:L17

Steidel CC, Hamilton D 1993. *Astron. J.* 105:2017

Steidel CC, Shapley AE, Pettini M, et al. 2004. *Ap. J.* 604:534

Steidel CC, Pettini M, Hamilton D 1995. *Astron. J.* 110:2519

Sullivan M, Treyer MA, Ellis RS, et al. 2000. *MNRAS* 312:442

Takeuchi TT, Ishii TT, Dole H, et al. 2006. *Astron. Astrophys.* 448:525

Takeuchi TT, Yoshikawa K, Ishii TT 2003. *Ap. J. Let.* 587:L89

Thompson RI, Eisenstein D, Fan X, et al. 2006. *Ap. J.* 647:787

Tilvi V, Papovich C, Tran, KVH, et al. 2013. *Ap. J.* 768:56

Tinsley BM 1980. *Fundam. Cosmic Phys.* 5:287

Trenti M, Perna R, Levesque EM, Shull JM, Stocke JT 2012. *Ap. J. Let.* 749:L38

Tresse L, Ilbert O, Zucca E, et al. 2007. *Astron. Astrophys.* 472:403

Tresse L, Maddox SJ 1998. *Ap. J.* 495:691

Tresse L, Maddox SJ, Le Fevre O, Cuby J-G 2002. *MNRAS* 337:369

Treyer M, Ellis RS, Milliard B, Donas J, Bridges TJ 1998. *MNRAS* 300:303
Vaccari M, Marchetti L, Franceschini A, et al. 2010. *Astron. Astrophys.* 518:L20
Vale A, Ostriker JP 2004. *MNRAS* 353:189
Vanzella E, Guo Y, Giavalisco M, et al. 2012. *Ap. J.* 751:70
Venkatesan A, Truran JW 2003. *Ap. J. Let.* 594:L1
Verma A, Lehnert MD, Förster Schreiber NM, et al. 2007. *MNRAS* 377:1024
Wang W-H, Cowie LL, Barger AJ, et al. 2010. *Ap. J. Suppl.* 187:251
Wardlow JL, Smail I, Coppin KEK, et al. 2011. *MNRAS* 415:1479
Weidemann V 2000. *Astron. Astrophys.* 363:647
Westra E, Geller MJ, Kurtz MJ, Fabricant DG, Dell'Antonio I 2010. *Ap. J.* 708:534
White SDM, Frenk CS 1991. *Ap. J.* 379:52
White SDM, Rees MJ 1978. *MNRAS* 183:341
Wiklund T, Dickinson M, Ferguson HC, et al. 2008. *Ap. J.* 676:781
Wilkins SM, Hopkins AM, Trentham N, Tojeiro R 2008b. *MNRAS* 391:363
Wilkins SM, Trentham N, Hopkins AM 2008. *MNRAS* 385:687
Wilson G, Cowie LL, Barger AJ, Burke DJ 2002. *Astron. J.* 124:1258
Wolf C, Bell EF, McIntosh DH, et al. 2005. *Ap. J.* 630:771
Woosley SE, Bloom JS 2006. *Annu. Rev. Astron. Astrophys.* 44:507
Wyder TK, Treyer MA, Milliard B, et al. 2005. *Ap. J. Let.* 619:L15
Yabe K, Ohta K, Iwata I, et al. 2009. *Ap. J.* 693:507
Yan H, Dickinson M, Giavalisco M, et al. 2006. *Ap. J.* 651:24
Yan H, Finkelstein SL, Kuang K-H, et al. 2012. *Ap. J.* 761:177
Yan L, McCarthy PJ, Freudling W, et al. 1999. *Ap. J. Let.* 519:L47
Yang X, Mo HJ, van den Bosch FC 2003. *MNRAS* 339:1057
Yepes G, Kates R, Khokhlov A, Klypin A 1997. *MNRAS* 284:235
York DG, Adelman J, Anderson JE, et al. 2000. *Astron. J.* 120:1579
Yoshida M, Shimasaku K, Kashikawa N, et al. 2006. *Ap. J.* 653:988
Yun MS, Reddy NA, Condon JJ 2001. *Ap. J.* 554: 803
Zemp M, Gnedin OY, Gnedin NY, Kravtsov AV 2012. *Ap. J.* 748:54
Zentner AR, Hearin AP, van den Bosch FC 2013. *MNRAS* submitted (arXiv:1311.1818)
Zheng W, Postman M, Zitrin A, et al. 2012. *Nature* 489:406

Table 1: Determinations of the Cosmic Star Formation Rate Density from UV data (top group) and IR data (bottom group) used in this review.

	redshift range	A_{FUV}^a [mag]	$\log \psi^b$ [$M_{\odot} \text{ yr}^{-1} \text{ Mpc}^{-3}$]	symbols used in Fig. 9
Wyder et al. (2005)	0.01-0.1	1.80	$-1.82^{+0.09}_{-0.02}$	blue-gray hexagon
Schiminovich et al. (2005)	0.2-0.4	1.80	$-1.50^{+0.05}_{-0.05}$	blue triangles
	0.4-0.6	1.80	$-1.39^{+0.15}_{-0.08}$	
	0.6-0.8	1.80	$-1.20^{+0.31}_{-0.13}$	
	0.8-1.2	1.80	$-1.25^{+0.13}_{-0.13}$	
Robotham & Driver (2011)	0.05	1.57	$-1.77^{+0.08}_{-0.09}$	dark green pentagon
Cucciati et al. (2012)	0.05-0.2	1.11	$-1.75^{+0.18}_{-0.18}$	green squares
	0.2-0.4	1.35	$-1.55^{+0.12}_{-0.12}$	
	0.4-0.6	1.64	$-1.44^{+0.10}_{-0.10}$	
	0.6-0.8	1.92	$-1.24^{+0.10}_{-0.10}$	
	0.8-1.0	2.22	$-0.99^{+0.09}_{-0.08}$	
	1.0-1.2	2.21	$-0.94^{+0.09}_{-0.09}$	
	1.2-1.7	2.17	$-0.95^{+0.15}_{-0.08}$	
	1.7-2.5	1.94	$-0.75^{+0.49}_{-0.09}$	
	2.5-3.5	1.47	$-1.04^{+0.26}_{-0.15}$	
	3.5-4.5	0.97	$-1.69^{+0.22}_{-0.32}$	
Dahlen et al. (2007)	0.92-1.33	2.03	$-1.02^{+0.08}_{-0.08}$	turquoise pentagons
	1.62-1.88	2.03	$-0.75^{+0.12}_{-0.12}$	
	2.08-2.37	2.03	$-0.87^{+0.09}_{-0.09}$	
Reddy & Steidel (2009)	1.9-2.7	1.36	$-0.75^{+0.09}_{-0.11}$	dark green triangles
	2.7-3.4	1.07	$-0.97^{+0.11}_{-0.15}$	
Bouwens et al. (2012a),(2012b)	3.8	0.58	$-1.29^{+0.05}_{-0.05}$	magenta pentagons
	4.9	0.44	$-1.42^{+0.06}_{-0.06}$	
	5.9	0.20	$-1.65^{+0.08}_{-0.08}$	
	7.0	0.10	$-1.79^{+0.10}_{-0.10}$	
	7.9	0.0	$-2.09^{+0.11}_{-0.11}$	
Schenker et al. (2013)	7.0	0.10	$-2.00^{+0.10}_{-0.11}$	black crosses
	8.0	0.0	$-2.21^{+0.14}_{-0.14}$	
Sanders et al. (2003)	0.03	—	$-1.72^{+0.02}_{-0.03}$	brown circle
Takeuchi et al. (2003)	0.03	—	$-1.95^{+0.20}_{-0.20}$	dark orange square
Magnelli et al. (2011)	0.40-0.70	—	$-1.34^{+0.22}_{-0.11}$	red open hexagons
	0.70-1.00	—	$-0.96^{+0.15}_{-0.19}$	
	1.00-1.30	—	$-0.89^{+0.27}_{-0.21}$	
	1.30-1.80	—	$-0.91^{+0.17}_{-0.21}$	
	1.80-2.30	—	$-0.89^{+0.21}_{-0.25}$	
Magnelli et al. (2013)	0.40-0.70	—	$-1.22^{+0.08}_{-0.11}$	red filled hexagons
	0.70-1.00	—	$-1.10^{+0.10}_{-0.13}$	
	1.00-1.30	—	$-0.96^{+0.13}_{-0.20}$	
	1.30-1.80	—	$-0.94^{+0.13}_{-0.18}$	
	1.80-2.30	—	$-0.80^{+0.18}_{-0.15}$	
Gruppioni et al. (2013)	0.00-0.30	—	$-1.64^{+0.09}_{-0.11}$	dark red filled hexagons
	0.30-0.45	—	$-1.42^{+0.03}_{-0.04}$	
	0.45-0.60	—	$-1.32^{+0.05}_{-0.05}$	
	0.60-0.80	—	$-1.14^{+0.06}_{-0.06}$	
	0.80-1.00	—	$-0.94^{+0.05}_{-0.06}$	
	1.00-1.20	—	$-0.81^{+0.04}_{-0.05}$	
	1.20-1.70	—	$-0.84^{+0.04}_{-0.04}$	
	1.70-2.00	—	$-0.86^{+0.02}_{-0.03}$	
	2.00-2.50	—	$-0.91^{+0.09}_{-0.12}$	
	2.50-3.00	—	$-0.86^{+0.15}_{-0.23}$	
	3.00-4.20	—	$-1.36^{+0.23}_{-0.50}$	

^a In our notation, $A_{\text{FUV}} \equiv -2.5 \log_{10}(k_d)$.

^b All our star formation rate densities are based on the integration of the best-fit luminosity function parameters down to the same *relative* limiting luminosity, in units of the characteristic luminosity L^* , of $L_{\text{min}} = 0.03 L^*$. A Salpeter IMF has been assumed.

Table 2: Determinations of the Cosmic Stellar Mass Density used in this review.

	redshift range	$\log \rho_*^a$ [$M_\odot \text{ Mpc}^{-3}$]	symbols used in Fig. 11
Li & White (2009)	0.07	$8.59^{+0.01}_{-0.01}$	gray dot
Gallazzi et al. (2008)	0.005-0.22	$8.78^{+0.07}_{-0.08}$	dark green square
Moustakas et al. (2013)	0.0-0.2	$8.59^{+0.05}_{-0.05}$	magenta stars
	0.2-0.3	$8.56^{+0.09}_{-0.09}$	
	0.3-0.4	$8.59^{+0.06}_{-0.06}$	
	0.4-0.5	$8.55^{+0.08}_{-0.08}$	
Bielby et al. (2012) ^b	0.2-0.4	$8.46^{+0.09}_{-0.12}$	pink filled hexagons
	0.4-0.6	$8.33^{+0.03}_{-0.03}$	
	0.6-0.8	$8.45^{+0.08}_{-0.1}$	
	0.8-1.0	$8.42^{+0.05}_{-0.06}$	
	1.0-1.2	$8.25^{+0.04}_{-0.04}$	
	1.2-1.5	$8.14^{+0.06}_{-0.06}$	
	1.5-2.0	$8.16^{+0.32}_{-0.03}$	
Perez-González et al. (2008)	0.0-0.2	$8.75^{+0.12}_{-0.12}$	red triangles
	0.2-0.4	$8.61^{+0.06}_{-0.06}$	
	0.4-0.6	$8.57^{+0.04}_{-0.04}$	
	0.6-0.8	$8.52^{+0.05}_{-0.05}$	
	0.8-1.0	$8.44^{+0.05}_{-0.05}$	
	1.0-1.3	$8.35^{+0.05}_{-0.05}$	
	1.3-1.6	$8.18^{+0.07}_{-0.07}$	
	1.6-2.0	$8.02^{+0.07}_{-0.07}$	
	2.0-2.5	$7.87^{+0.09}_{-0.09}$	
	2.5-3.0	$7.76^{+0.18}_{-0.18}$	
	3.0-3.5	$7.63^{+0.14}_{-0.14}$	
	3.5-4.0	$7.49^{+0.13}_{-0.13}$	
Ilbert et al. (2013)	0.2-0.5	$8.55^{+0.08}_{-0.09}$	cyan stars
	0.5-0.8	$8.47^{+0.07}_{-0.08}$	
	0.8-1.1	$8.50^{+0.08}_{-0.08}$	
	1.1-1.5	$8.34^{+0.10}_{-0.07}$	
	1.5-2.0	$8.11^{+0.05}_{-0.06}$	
	2.0-2.5	$7.87^{+0.08}_{-0.08}$	
	2.5-3.0	$7.64^{+0.15}_{-0.14}$	
	3.0-4.0	$7.24^{+0.18}_{-0.20}$	
Muzzin et al. (2013)	0.2-0.5	$8.61^{+0.06}_{-0.06}$	blue squares
	0.5-1.0	$8.46^{+0.03}_{-0.03}$	
	1.0-1.5	$8.22^{+0.03}_{-0.03}$	
	1.5-2.0	$7.99^{+0.05}_{-0.03}$	
	2.0-2.5	$7.63^{+0.11}_{-0.04}$	
	2.5-3.0	$7.52^{+0.13}_{-0.09}$	
	3.0-4.0	$6.84^{+0.43}_{-0.20}$	
Arnouts et al. (2007)	0.3	$8.78^{+0.12}_{-0.16}$	yellow dots
	0.5	$8.64^{+0.09}_{-0.11}$	
	0.7	$8.62^{+0.08}_{-0.10}$	
	0.9	$8.70^{+0.11}_{-0.15}$	
	1.1	$8.51^{+0.08}_{-0.11}$	
	1.35	$8.39^{+0.10}_{-0.13}$	
	1.75	$8.13^{+0.10}_{-0.13}$	

Table 2: (cont.)

	redshift range	$\log \rho_*^a$ [$M_\odot \text{ Mpc}^{-3}$]	symbols used in Fig. 11
Pozzetti et al. (2010)	0.1-0.35	8.58	black squares
	0.35-0.55	8.49	
	0.55-0.75	8.50	
	0.75-1.00	8.42	
Kajisawa et al. (2009)	0.5-1.0	8.63	green squares
	1.0-1.5	8.30	
	1.5-2.5	8.04	
	2.5-3.5	7.74	
Marchesini et al. (2009)	1.3-2.0	$8.11^{+0.02}_{-0.02}$	blue dots
	2.0-3.0	$7.75^{+0.05}_{-0.04}$	
	3.0-4.0	$7.47^{+0.37}_{-0.13}$	
Reddy et al. (2012)	1.9-2.7	$8.10^{+0.03}_{-0.03}$	dark green triangles
	2.7-3.4	$7.87^{+0.03}_{-0.03}$	
Caputi et al. (2011)	3.0-3.5	$7.32^{+0.04}_{-0.02}$	brown pentagons
	3.5-4.25	$7.05^{+0.11}_{-0.10}$	
	4.25-5.0	$6.37^{+0.14}_{-0.54}$	
González et al. (2011) ^c	3.8	$7.24^{+0.06}_{-0.06}$	orange dots
	5.0	$6.87^{+0.08}_{-0.09}$	
	5.9	$6.79^{+0.09}_{-0.09}$	
	6.8	$6.46^{+0.14}_{-0.17}$	
Lee et al. (2012) ^c	3.7	$7.30^{+0.07}_{-0.09}$	gray squares
	5.0	$6.75^{+0.33}_{-0.16}$	
Yabe et al. (2009)	5.0	$7.19^{+0.19}_{-0.35}$	small black pentagon
Labbé et al. (2013)	8.0	$5.78^{+0.22}_{-0.30}$	red square

^a All the stellar mass densities have been derived assuming a Salpeter IMF.

^b Stellar mass densities were computed by averaging over the four fields studied by Bielby et al. (2012).

^c Following Stark et al. (2013), the mass densities of González et al. (2011) and Lee et al. (2012) at $z \simeq 4, 5, 6,$ and 7 have been reduced by the factor 1.1, 1.3, 1.6, and 2.4, respectively, to account for contamination by nebular emission lines.